

Third-order optical nonlinearities of glass-metal nanocomposites

Dissertation

zur Erlangung des akademischen Grades

doctor rerum naturalium

(Dr. rer. nat.)

vorgelegt der

Naturwissenschaftlichen Fakultät II

der Martin-Luther-Universität Halle-Wittenberg

von

Sabitha Mohan

geb. am 1. Mai 1980 in Mariathuruthu, Kottayam, India

Gutachter:

- 1.PD.Dr. Gerhard Seifert(Martin-Luther-Universität Halle Wittenberg)
- 2.PD.Dr. Frank Hubenthal(Universität Kassel)
- 3.Prof.Dr. Ralf Wehrsphon(Martin-Luther-Universität Halle Wittenberg)

verteidigt am 07.11.2011

Contents

1	Introduction	1
1.1	Road map through this thesis	2
2	Nonlinear optical properties of condensed matter	5
2.1	Introduction	5
2.2	Third order nonlinear optical process	6
2.2.1	Resonant nonlinear process	8
2.2.2	Non-resonant nonlinear process	9
2.3	Linear optical properties of nanocomposite materials	10
2.3.1	Effective medium theories	10
2.3.2	Optics of Metals	12
2.3.3	Particle plasmon oscillation	14
2.3.4	Plasmon resonances of non-spherical nanoparticles	18
2.4	Effective nonlinear susceptibility of the metallic nanoparticles in glass	21
2.4.1	Intraband contribution	22
2.4.2	Interband contribution	22
2.4.3	Hot electron contribution	23
2.5	Saturation of Surface Plasmon oscillation under ultra-short excitation	26
3	Experimental technique	29
3.1	Preparation and characterization of nanocomposite materials	29
3.1.1	Glasses containing spherical nanoparticles	29
3.1.2	Glasses containing ellipsoidal nanoparticles : Mechanically stretched nanoparticles	30
3.1.3	Glasses containing ellipsoidal nanoparticles: Laser irradiated samples	32
3.2	Laser systems	33
3.3	Measurement technique	36
3.3.1	Z-scan	36
3.3.2	I-scan	38
3.3.3	Z-scan analysis for thin samples	39
4	Nonlinear optical properties of mechanically stretched nano-particles	43
4.1	Introduction	43
4.2	Sample specification	44
4.3	Nonlinear optical measurements	45

4.3.1	Experimental results and Fitting procedure	46
4.3.2	Sign reversal in nonlinearity :Qualitative description	51
4.4	Local-field effect driven optical nonlinearity	55
4.5	Intensity dependent nonlinear optical properties	59
4.5.1	Photo-Physics of Sample LSPR_550	60
4.5.2	Photo-Physics of Sample LSPR_1200	62
4.6	Conclusions	64
5	Spectral dependence of the third-order optical nonlinearity	67
5.1	Introduction	67
5.2	Experimental Results	67
5.3	Modelling of Open aperture I-scan	69
5.4	Maxwell Garnett samples	72
5.5	Conclusion	76
6	Directional selective optical limiting in bi-layer glass-metal nanocomposites	77
6.1	Introduction	77
6.2	Theoretical modelling	78
6.2.1	Gaussian beam propagation through layered structures	80
6.2.2	Propagation through bi-layer structure (Lossless substrate)	85
6.2.3	From the limit of thin sample to thick sample approximation	86
6.2.4	Propagation through bi-layer structure (Lossy substrate)	87
6.3	Theoretical conclusions	88
6.4	Sample specification	88
6.5	Experimental results	89
6.6	Nonlinear transmission measurements performed on simple bi-layer structures	95
6.7	Conclusions and Outlook	96
7	Summary	99
A	Appendix 1: Mathematical calculations	103
A.1	Symmetrisation technique for the evaluation of nonlinear refraction	103
A.2	Appendix 2: Calculation of the shape factor L	104
A.3	Appendix 3: Maxwell-Garnett Calculations	104

List of Figures

2.1	Relaxation processes in closed two-level	8
2.2	The typical Maxwell garnett geometry used for the nanocomposite materials [64].	11
2.3	The real(a) and imaginary(b) parts of dielectric function of silver	13
2.4	The real(a) and imaginary(b) parts of dielectric function of gold	13
2.5	The interaction of light with clusters	15
2.6	Field lines of the Poynting vector	16
2.7	The real and imaginary parts of field enhancement factor f , the phase ϕ	17
2.8	Calculated Mie extinction spectra of spherical nanoparticles	18
2.9	Geometrical factors for a spheroids (left)	19
2.10	Effect of shape on the spectral position of dipolar absorption & polarized extinction spectra of prolate (a) and oblate (b)	20
2.11	Fermi smearing mechanism & Instantaneous electron distribution	25
2.12	The scheme of the relaxation processes in a metallic nanoparticle[45]	27
3.1	TEM picture of spherical silver nanoparticles	30
3.2	The polarized extinction & SEM micrograph of the sample.	31
3.3	TEM images of the deformed nanoparticles	32
3.4	The scheme of the main laser system (Spectra Physics) used in this work.	34
3.5	Two-dimensional spatial beam profile	35
3.6	SHG-FROG trace, showing ~ 108 fs	35
3.7	The schematic of Closed and Open aperture Z-scan setup	36
3.8	Geometrical optics analysis of Z-scan	37
3.9	Closed and Open aperture Z-scan signals	38
3.10	The schematic of Closed and Open aperture I-scan setup	39
4.1	The polarized linear extinction spectra of the samples	44
4.2	The Electric field vector and the direction of the dipolar polarizibilities	45
4.3	The experimental configuration used for the Z-scan measurement	46
4.4	The open and closed aperture Z-scan measurements performed on LSPR_550	47
4.5	Energy level scheme used for the analysis of the plasmon	48
4.6	Polarized Z-scan measurements (LSPR_550, 1030 nm)	49
4.7	Polarized Z-scan measurements (LSPR_550, 800 nm)	51
4.8	Polarized Z-scan measurements (LSPR_450, 1030 nm)	52
4.9	Polarized Z-scan measurements (LSPR_450,800 nm)	53
4.10	The spectral dependence of n_2 and β with respect to the detuning of the SPR	54
4.11	Z-scan measurements (LSPR_550, 1030 nm) and (LSPR_1200, 1030 nm)	55

LIST OF FIGURES

4.12	The values obtained for in saturation intensity I_s at different excitation intensities	56
4.13	The values obtained for in saturation intensity n_2 at different excitation intensities	56
4.14	The spectral dependence of n_2 and β in the configuration	59
4.15	Intensity dependent open aperture Z-scan measurements(LSPR_550 configuration)	60
4.16	The polarized linear extinction spectra of sample LSPR_1200 & 550 configuration	60
4.17	Fit values of two-photon absorption coefficient at different intensities (LSPR_550)	61
4.18	Open aperture Z-scan measurements performed on LSPR_1200 in the configuration	62
4.19	The variation of transmission change ΔT measured for LSPR_1200	63
5.1	The polarized extinction spectra of the nanocomposites measured	68
5.2	The Intensity scan data measured for different irradiated areas performed in the configuration	69
5.3	The figure represents the comparison between the experimental and theoretical fitting	70
5.4	The polarized extinction spectra of the area A1 & A4	71
5.5	The figure represents the comparison between the experimental and theoretical fitting for area A9 & A2	72
5.6	The comparison between the extinction spectra calculated using the Maxwell-Garnett theory	74
5.7	The variation of nonlinear absorption coefficient (β), filling factor (p)and linear absorption	74
6.1	The schematic of bi-layer sample structure used for the theoretical modelling . .	81
6.2	The beam radius calculated at the exit of substrate material and the sample layer	82
6.3	The intensity dependent focus length	82
6.4	Schematic of the beam-sample configuration used for the calculation of open aperture transmission curve	83
6.5	The simulated open aperture Z-scan curves	84
6.6	The simulated open aperture Z-scan curves calculated for lossless substrate . . .	86
6.7	Figure represents the comparison of anisotropic transmission between the lossless and lossy substrate material	88
6.8	The linear transmission spectra measured from pure glass, and glass containing silver nanoparticles	89
6.9	Geometry of bi-layer sample structure	90
6.10	The open aperture Z-scan curves measured from the heavy doped, $(\frac{Z_0}{L}) = 2.2$. .	91
6.11	The open aperture Z-scan curves measured from the light doped, $(\frac{Z_0}{L}) = 2.2$. .	91
6.12	The comparison of anisotropic transmission between the heavy and light doped sample	92
6.13	The open aperture Z-Scan curves measured from the heavy doped nanocomposite glass, $(\frac{Z_0}{L}) = 1.3$	93
6.14	he open aperture Z-scan curves measured from the TiO ₂ -SiO ₂	96
A.1	Fitted value of FWHM for each irradiated area of the sample.	106

List of Tables

2.1	Drude parameters used for the Ag and Au	14
4.1	Nonlinear coefficients of mechanically stretched samples	64
5.1	Nonlinear coefficients of laser irradiated samples	76

LIST OF TABLES

Chapter 1

Introduction

The 21st century is often designated as the *century of the photon*. This notion has been chosen in analogy to the past *electron* century, which saw a tremendous technological progress based on the fast and substantial improvements of electronic circuits and the concomitant exponential growth of applications in public and private life. It is a common sense nowadays that technologies relying on control and manipulation of light will take over a similar role in the current century. Laser based technologies has blossomed into a mature but still exciting and rapidly developing field of science. A large technological progress has happened in the field of optoelectronics. But the price paid for this advance is the lossage of 30% of their energy in converting electrons into photons and vice-versa. An alternative solution is the invention of optical counterpart of many electronic devices with photons essentially replacing electrons [10, 33].

At present, the attention is mainly focussed on the development of optical devices to switch and process light signals without converting them into electronic form. They are based on the development of materials possessing ultrafast optical nonlinearities with controllable properties i.e. changes of the refractive index caused by an intense optical beam or by an applied electric field [76]. The materials based on inorganic polymers, semi-conductors has received much attention in the past several years [11]. On the other hand the nanocomposite materials are proved to be one of the special candidates, in which materials having different linear and nonlinear properties are suitably mixed to produce a heterogeneous systems possessing suitable nonlinear properties. The large ultrafast optical nonlinearity of the metals can be utilized by mixing them with homogeneous dielectric matrix. The spectacular properties arising from the “surface plasmon resonance” can produce enhanced optical properties [60, 64]. In this context emphasis has been given to the anisotropic nonlinear optical

properties of nanocomposites.

The primary aim of the PhD dissertation is to investigate the nonlinear optical properties arising from the structural anisotropy of the nanoparticles. We have worked on nanocomposite materials having different kinds of structural anisotropy. The observed nonlinear properties arising in resonant and non-resonant light interaction regime is measured and analysed in context of surface plasmon resonance.

1.1 Road map through this thesis

This thesis is organized as follows. The chapter 2 briefly touches the third order nonlinear optical mechanisms observed in resonant and non-resonant light interaction regime. The linear optical properties of the nanoparticles are described on the basis of an effective medium theory (section 2.3). The source of optical nonlinearity of the nanocomposite systems are realised in section 2.4, which has been used as the bench mark for the analysis of the observed nonlinear measurements in the later chapters.

Chapter 3 gives a short description on the ultrashort laser systems used for the nonlinear characterisation. A brief discussion on the spatial and temporal characteristics of the laser beam is presented. The technical details of the femtosecond Z-scan method together with the Z-scan fitting procedure is included in the following sections.

Chapter 4 deals with the nonlinear measurements performed on samples containing mechanically stretched nanoparticles. The nonlinear optical properties arising in the resonant and non-resonant light interaction regime is investigated by making use of the shape anisotropy of the nanoparticles. The sign reversal observed in optical nonlinearity is analysed in the context of the surface plasmon resonance. The dispersive behavior of optical nonlinearity is calculated and described using the structural anisotropy of the nanoparticles. The photo-physical mechanisms observed in each sample is addressed and discussed in section 4.5.

Chapter 5 deals with the nonlinear studies performed on the Maxwell Garnett type of samples. The nonlinear measurements performed on the laser irradiated samples are found to replicate the physical properties of constituent elements of the composite materials.

In chapter 6 we have discussed the optical diode like behaviour observed in a bi-layer sample structure. Uni-directional behaviour in the nonlinear transmission is described as the consequence of pure nonlinear refractive effects from the substrate material. The observed anisotropic transmission can be utilised for the realisation of many potential passive photonic devices. Finally a summary of the thesis is given in chapter 7.

Chapter 2

Nonlinear optical properties of condensed matter

2.1 Introduction

The physics of interaction of light with matter has been well understood since the pioneering work of J.C. Maxwell. The interactions of electro-magnetic fields with matter are described through Maxwell's equations. In general the response of the medium to the driving electric field \vec{E} can be well explained through the material polarization \vec{P} (defined as dipole moment per unit volume) [31]. In conventional optics, i.e, under weak field excitation, the medium responds linearly to the interacting electro-magnetic field which can be expressed as

$$\vec{P}(\omega, t) = \varepsilon_0 \chi^{(1)}(\omega, t) \vec{E}(\omega, t) \quad (2.1)$$

The resulting linear optical process is familiar to us through our visual sense such as reflection, refraction, absorption and transmission. If the light waves are able to penetrate and pass through a medium, it would occur without any interaction between the waves [25, 31].

On the other hand the response of any physically oscillating system becomes non-linear if it is over driven. Under highly intense illumination, the optical properties of the medium become solely controlled by the strength of the electric field. The nonlinearity exhibited in the polarization of the medium is often expressed by a power series expansion of applied field as

$$\vec{P} = \varepsilon_0 \chi^{(1)} \vec{E} + \varepsilon_0 \chi^{(2)} \vec{E} : \vec{E} + \varepsilon_0 \chi^{(3)} \vec{E} : \vec{E} : \vec{E} + \dots \quad (2.2)$$

Here $\chi^{(1)}$ represents the linear susceptibility of the material. The terms $\chi^{(2)}$ and $\chi^{(3)}$ are known as the second- and third-order nonlinear susceptibilities, respectively. The Taylor series expansion in equation (2.2) is valid as long as the involved nonlinear processes are weak. In the expansion series, the even order terms are responsible for parametric processes such as sum and difference frequency generation and odd order terms result in self action effects. For materials featuring a center of inversion, the physical processes resulting from even order terms are forbidden and the lowest order nonlinear processes are arising from third order process such as optical Kerr effect, optical phase conjugation, optical bistability, degenerate four wave mixing and third harmonic generation [7, 8, 66].

The physical origin of optical nonlinearity in general can be derived either from electronic, vibrational or rotational degrees of freedom. The electronic nonlinearity originates from the distortion of the electronic cloud about the atomic nucleus and responds exceedingly fast with a response time of the order of a few femtoseconds [6, 27]. The contribution from the nuclear motion responds in a picosecond time scale. Under femtosecond laser pulse excitation the dominant contribution to the optical nonlinearity is of electronic nature. With increasing pulse duration, other contributions start dominating the nonlinear process. For instance a variation in nonlinear refractive index can be expected due to the strain induced in the medium by the electric field and also by the local heating of the medium through the single photon absorption process. The former one is named as electro-strictive and the latter one attributed to thermal nonlinearities. Under nanosecond laser pulse excitation the contribution from thermal nonlinearity will contribute to the overall nonlinear process [49]. In this regard our attention is mainly focused on the ultra-fast third order nonlinear processes. The process arising from other nonlinear optical effects will not be considered in the further sections.

2.2 Third order nonlinear optical process

In general the nonlinear process arising from $\chi^{(3)}$ effects constitute of optical Kerr effect, optical limiting, optical phase conjugation, two-photon absorption, Brillouin and Raman scattering etc.

For isotropic materials and under weak field excitation, the power series expansion can be approximated as

$$\vec{P} = \varepsilon_0 \chi^{(1)} \vec{E} + \varepsilon_0 \chi^{(3)} \vec{E} : \vec{E} : \vec{E} = \varepsilon_0 \left(\chi^{(1)} + \chi^{(3)} \vec{E} : \vec{E} \right) \vec{E} \quad (2.3)$$

where the interacting electric field takes the following form $\vec{E} = \vec{E} e^{-i\omega t} + \vec{E}^* e^{i\omega t}$,

Hence the above expression can be re-written as

$$\vec{P} = \varepsilon_0 \chi_{eff} \vec{E} \quad (2.4)$$

where the effective susceptibility of the material system is defined as

$$\chi_{eff} = \chi^{(1)} + \chi^{(3)} |E|^2$$

In general, the susceptibility of the material is related to its refractive index through $n_0 = (1 + \chi_1)^{1/2}$. Accordingly in the nonlinear optical regime we can write

$$\begin{aligned} n &= n_0 \left(1 + \frac{\chi^{(3)} |E|^2}{n_0^2} \right)^{1/2} \\ n &\approx n_0 \left(1 + \frac{\chi^{(3)} |E|^2}{2n_0^2} \right) = n_0 + \tilde{n}_2 I \end{aligned} \quad (2.5)$$

where $\tilde{n}_2 = \frac{\chi^{(3)}}{\varepsilon_0 c n_0^2}$ and $I = \frac{c \varepsilon_0 n_0}{2} |E|^2$. In general \tilde{n}_2 is a complex quantity whose real part n_2 is responsible for nonlinear refractive effects and imaginary part β results in nonlinear absorptive effects. In general one can relate the nonlinear refractive index to complex susceptibility as given below

$$n_2 = \frac{3 \text{Re} \chi^{(3)}}{4 \varepsilon_0 c n_0^2} \quad \text{and} \quad \beta = \frac{3 \omega \text{Im} \chi^{(3)}}{2 \varepsilon_0 c^2 n_0^2}.$$

From the above equations we can learn that the effective refractive index of the medium is a linear function of the intensity of the incident light. This effect is otherwise known as the optical Kerr effect [7, 8, 74]. Due to the intensity dependence, the refractive index of the material can be modified by highly intense laser pulses which results in phenomena such as self-focusing of a laser beam, self-phase modulation of laser pulse or optical bistability of the nonlinear medium. The imaginary part β contributes to nonlinear absorption processes such as two-photon absorption and reverse saturable absorption [66].

The validity of the power series expansion (equation 2.2) used for the representation of nonlinear optical response depends primarily on the spectral regime of excitation and the strength of the driving electric field. In general, depending on the spectral regime of excitation two physical situations can be realised: the resonant and non-resonant optical processes.

2.2.1 Resonant nonlinear process

If the frequency ω of the incoming electric field is either in resonance with electronic, vibrational or rotational transitions of the material medium, an enhancement in the optical process occurs. For instance in case of saturable absorption, the power series expansion represented by equation 2.2 may not converge. Under resonant excitation, the perturbation techniques might fail to provide an adequate description of the response of the system to an applied optical field. The non-perturbative treatment based on the two-level approximation provides a good tool to deal such physical situations.

For instance let us consider a physical situation as shown in 2.1, where the laser photon energy $\hbar\omega$ is in resonance with the single photon transition between the ground state (a) and upper level (b) $\hbar\omega = \hbar(\omega_b - \omega_{ga})$. A coherent superposition state exists between the electronic polarization of the atomic system and the applied electric field immediately during the excitation.

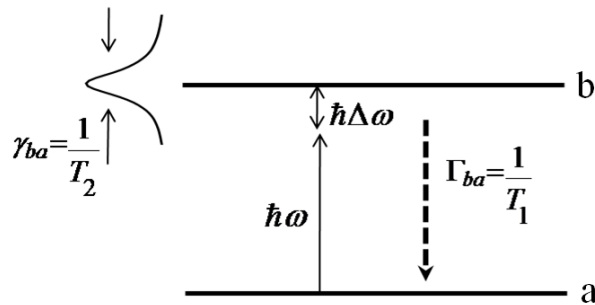


Figure 2.1: Relaxation processes of the closed two-level scheme. The upper level b decays to the lower level a at rate given by $\Gamma_{ba} = \frac{1}{T_1}$. We assume that the atomic dipole moment is dephased with characteristic time T_2 .

In real systems, such a coherent situation decays very fast due to scattering mechanisms. The rate at which the coherence is washed out determines the broadening of the absorption profile and hence the frequency response of the imaginary component of the linear susceptibility. The real part of the linear susceptibility gives rise to the dispersion of the refractive index. It is assumed that the rate at which photons are supplied to the system produces a negligible change of population in the upper and lower states. On the other hand in the nonlinear optical regime, when the incident irradiance is sufficiently high, the upper level can become appreciably occupied, reducing the availability of terminal states for optical transitions. The absorption thus decreases or bleaches. Associated with the change of absorption is

a change of the refractive index. Correspondingly the field corrected susceptibility is represented as

$$\overline{\chi(\omega; E)} = \frac{\chi^{(1)}(-\omega; \omega)}{1 + I_\omega / I_s(\Delta)} \quad (2.6)$$

where

$$\chi^{(1)}(-\omega; \omega) = \frac{-w_0 N e^2}{\varepsilon_0 \hbar (\Delta - i/T_2)} |r_{ab \cdot e}|^2$$

is the linear susceptibility of the two level medium where the real and imaginary parts describes the linear refraction and absorption, N represents the number density of polarizable units (equally the number of two-level atoms), $|r_{ab \cdot e}|$ the strength of the transition dipole moment for the atomic transition. The saturation intensity I_s is found to follow the dispersion relation of the following form $I_s(\Delta) = I_s^0 (1 + \Delta^2 T_2^2)$ where T_2 determines the dephasing time of the coherent electron oscillation [7, 8, 65].

2.2.2 Non-resonant nonlinear process

In non-resonant regime, if the strength of the applied electric field is less than the characteristic atomic field strength ($6 \times 10^9 \text{ Vcm}^{-1}$), then the perturbative treatment of optical nonlinearity (equation 2.2) is a good approximation. In the visible - near infrared spectral range, for excitation intensities less than 10^{14} Wcm^{-2} , the physical processes arising from $\chi^{(2)}$, $\chi^{(3)}$ and $\chi^{(5)}$ play a major role in the overall nonlinear mechanism.

In general the nonlinear process can be categorized into parametric and non-parametric processes. The parametric process can always be described by a real susceptibility; conversely, the nonparametric processes represent the complex susceptibilities. The sum and difference frequency generation, second and third harmonic generation fall in the category of parametric processes. On the other hand processes corresponding to the two and three photon absorption, stimulated Raman scattering comes in the class of non-parametric process.

As described in the previous paragraph, non-parametric effects such as two/three photon absorption, are processes in which the photons can bridge the energy gap of the material through the simultaneous absorption of photons. Thus the process is normally observed at the transparency regime of the sample. When two/three

photons are present together for a fleeting instant of time determined by the Uncertainty Principle, an optical transition can take place. Accordingly a transmission decrease can be observed at higher excitation intensities, resulting in an optical limiting mechanism. A part of the presented work deals with the 'optical diode' like behavior observed in an asymmetric bi-layer structure due to the direction selective optical limiting mechanism [65, 74, 75].

2.3 Linear optical properties of nanocomposite materials

The search for materials having large nonlinearities together with an ultrafast response time is highly demanding for the realization of many photonic applications. There are several approaches for the development of new materials for nonlinear optical applications. Among them, a well practiced technique is based on the materials architecture, in which constituent elements having different linear and nonlinear optical properties are combined to form composite systems. Such composites are a mixture of two or more materials which are homogeneous on a distance scale of the order of the optical wavelength. It is believed that an effective enhanced nonlinear optical response can appear in composite systems in which at least one component should possess an inherent nonlinear optical response. For instance the optical nonlinearity of any transparent dielectric material is improved by, mixing with highly nonlinear inclusions [9, 11, 64].

Materials in its nanosize dimension possess different physical properties who differ drastically from their parent bulk material. Among the different candidates in the family of nanometric nonlinear inclusions, the metal nanoparticles have gained special attention. Whenever the size of the metal is comparable to the mean free path of conduction electrons, the special optical features developing in metal nanoparticles in the visible and near infrared spectral range due to field enhancement lead to a large growth in optical nonlinearity. Correspondingly it has been proven that the $\chi^{(3)}$ of nanoparticles is six orders of magnitude larger than that of silicate glass [17, 60, 15].

2.3.1 Effective medium theories

Nanocomposite systems are formed by homogeneous mixing of constituent elements in a dielectric host matrix. Accordingly their optical properties are well described

2.3. LINEAR OPTICAL PROPERTIES OF NANOCOMPOSITE MATERIALS

through suitable effective medium theories. The choice of the effective medium theories are based on the size ($2R$), shape (L) and the volume filling factor ($p = V_{NP}/V_{sample}$) of the constituent elements where V_{NP} and V_{sample} denotes the volume of nanoparticle and the sample respectively. The two basic assumptions for the applicability of effective medium theories are, the size of the nano-constituent materials should be much less than the wavelength of the interacting electro-magnetic field ($2R \ll \lambda$), and hence the size dependent retardation effects can be excluded. The second criterion is that the volume filling factor of the constituent elements must be much less than its percolation threshold. The fundamental question is, how to define a proper dielectric function ϵ_{eff} which could explain the linear response of the composite medium to the incoming electro-magnetic field [64].

In general composite materials are formed by inter-mixing of two or more different constituents with the following size constraint. Each constituent is present in the whole in grains who are large enough so that their optical properties may be described by the bulk dielectric constant. At the same time the typical grain dimensions and spacing must be much smaller than an optical wavelength so that the composite may be described by effective optical parameters which are related to the constituent parameters [17, 58, 64, 70]; The schematic of such a kind of structure is shown in figure 2.2.

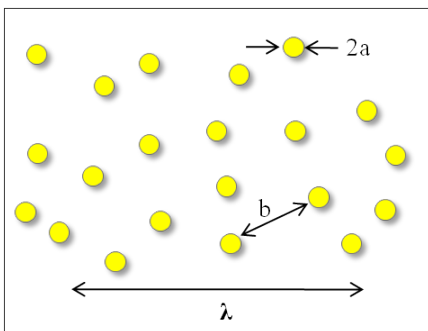


Figure 2.2: The typical Maxwell garnett geometry used for the nanocomposite materials [64].

The Maxwell Garnett theory, unlike other effective medium theories treats the two components in an asymmetric manner. The field acting on a grain due to all other grains, is assumed to be given by Lorentz local field. The expression for the effective dielectric constant ϵ_{eff} in which metal nanoparticles having the dielectric constant ϵ_m are embedded in a transparent dielectric host is given by a detailed derivation based on the approach of the Claussius-Mossotti relation

$$\frac{\varepsilon_{eff} - \varepsilon_d}{L_i \varepsilon_{eff} + (1 - L_i) \varepsilon_d} = p \frac{\varepsilon_m - \varepsilon_d}{L_i \varepsilon_m + (1 - L_i) \varepsilon_d} \quad (2.7)$$

Where p denotes the volume filling factor of constituent materials in the nanocomposite system and L_i defines the particle shape factor ($=\frac{1}{3}$ for spherical shape). It should be noted that the above equation has a pole at $(L_i \varepsilon_m + (1 - L_i) \varepsilon_d) = 0$ leading to a unique resonance in the visible spectral range; It has to be noted from the equation 2.7 that the Maxwell-Garnett theory can be extended to nanoparticles having different geometrical shape. Thus one could conclude that linear optical properties of composite systems can be tuned by suitably selecting the type of metal for the nanoparticle, the dielectric host matrix, controlling the size, shape and concentration of the constituent materials. In the coming section, the influence of each parameter on the effective dielectric constant of the nanocomposite system will be discussed [5, 12, 39, 41, 44, 42].

2.3.2 Optics of Metals

The optical properties of metals have been studied since the time of Drude. The Drude model assumes that, when the atoms of the metallic elements are brought together to form the metal, the valence electrons are detached and wander freely through the metal, while the metallic ions are intact and play the role of the immobile positive particles. Hence a charge neutrality is achieved at the equilibrium. But if the electrons are disturbed slightly from equilibrium, the nonuniform charge distribution will create an electric field. The electron gas having acquired momentum from the field, will overshoot the equilibrium configuration resulting in a collective oscillation of the electron gas known as plasma oscillation, its frequency is given by $\omega_p^2 = \frac{Ne^2}{\varepsilon_0 m_e}$, where N , e and m_e are the electronic number density, charge and mass respectively [1, 34, 41].

From Drude model the dielectric function of the free electron gas is represented as

$$\varepsilon(\omega) = 1 - \frac{\omega_p^2}{\omega^2 + i\Gamma\omega} \quad (2.8)$$

The phenomenological relaxation constant Γ is related to the electron mean free path l by $\Gamma = \frac{v_F}{l}$, where v_F the Fermi velocity.

2.3. LINEAR OPTICAL PROPERTIES OF NANOCOMPOSITE MATERIALS

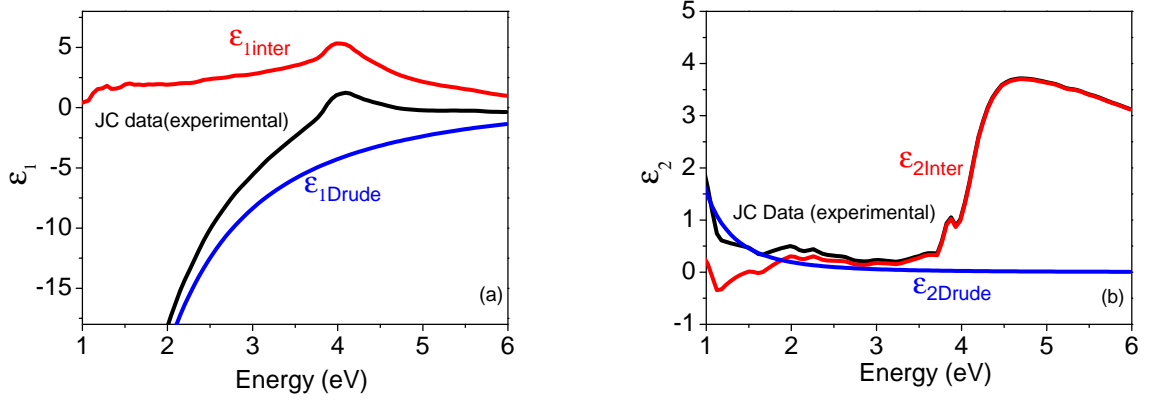


Figure 2.3: The real (a) and imaginary (b) parts of the dielectric function of silver. The experimental data is taken from the Johnson and Christy(JC). The experimental data is compared with the calculated one using the empirical formula based on Drude theory. The interband part is calculated by taking the difference between JC data and the Drude part

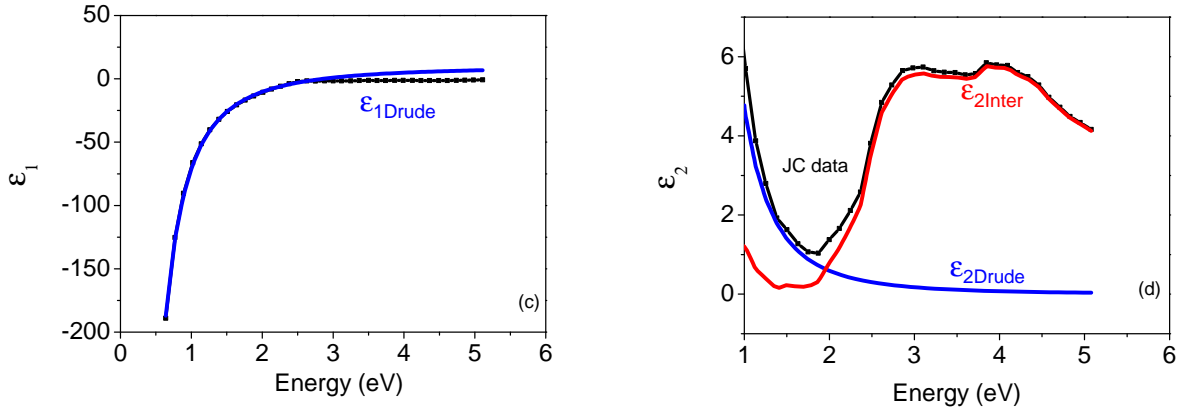


Figure 2.4: The real (a) and imaginary (b) parts of the dielectric function of gold. The experimental data is taken from the Johnson and Christy(JC). The experimental data is compared with the calculated one using the empirical formula based on Drude theory. The interband part is calculated by taking the difference between JC data and the Drude part

To a certain extent the Drude model is applicable to conduction electron metals such as alkali metals. But a substantial deviation is observed for the noble metals gold, silver and copper in the near ultra-violet, visible spectral range.

Silver looks white which is in accordance to the Drude model, but copper is reddish and gold is yellow; which indicates that they do not reflect well at visible spectral range even if the plasmon frequency is in the ultraviolet region. The filled d-bands close to the Fermi surface cause a highly polarized environment. The influence of the electrons (d- band electrons) which undergo interband transitions gives an additional

complex contribution $\varepsilon^{IB} = \varepsilon_1^{IB} + i\varepsilon_2^{IB}$ to the dielectric function of the metals. The complex contribution ε_2^{IB} , a direct measure of energy dissipation, contributes substantially at the interband transition threshold; whereas the real part ε_1^{IB} is important for smaller frequencies. At lower frequencies, the contribution due to interband transition is replaced by an averaged frequency independent value known as the polarization of the ion-core denoted by ε_∞ . Hence one can come up with the following empirical formula for the dielectric function

$$\varepsilon(\omega) = \varepsilon_\infty - \frac{\omega_p^2}{\omega^2 + i\Gamma\omega}. \quad (2.9)$$

Figure 2.3 and 2.4 represents the comparison between the dielectric constant of silver and gold measured by Johnson and Christy with the Drude formula corrected for the background dielectric constant ε_∞ . The table 2.1 lists the Drude-parameter values used for silver and gold. We could see that the threshold for interband transitions for silver is around 4 eV and that for gold is at 2 eV.

	$\hbar\omega_p$ (eV)	Γ (meV)	ε_∞
Ag	9.1	20	4.5
Au	9	60	9.9

Table 2.1: Drude parameters used for the Ag and Au. ε_∞ represents the frequency independent polarization contribution from ionic core.

It is quite reasonable to approximate that by reducing the dimension of bulk metallic systems there could be a modification in the collective behavior of electronic motion. i.e. for extremely small systems electrons could be able to sense the presence of the boundaries. In the forthcoming sections we will consider the optical properties of free electrons which are constrained to move in the reduced dimension.

2.3.3 Particle plasmon oscillation

Since ancient times, metal-nanocomposite glasses have gained much attention for coloring of church windows and ceramic pottery. Some historical examples are Roman church windows, the beautiful Lycurgus cup (Byzantine empire, 4th century AD). In 1908 Gaustav Mie developed a theory in an effort to understand the varied colors in absorption and scattering exhibited by small colloidal particles of gold suspended in water. The electrodynamic calculation based on Mie theory identified two

2.3. LINEAR OPTICAL PROPERTIES OF NANOCOMPOSITE MATERIALS

size regimes. The first, the *extrinsic size effects* which are concerned for nanoparticles of the size of the order of $2R > 30$ nm; in this size regime the electrodynamic theory could explain the nanoparticle's optical properties using bulk dielectric functions. The second one, the *intrinsic size effects* in which the electrodynamics tend to approximate to the electrostatic description with a size dependent dielectric function (figure. 2.5) [5, 41, 48].

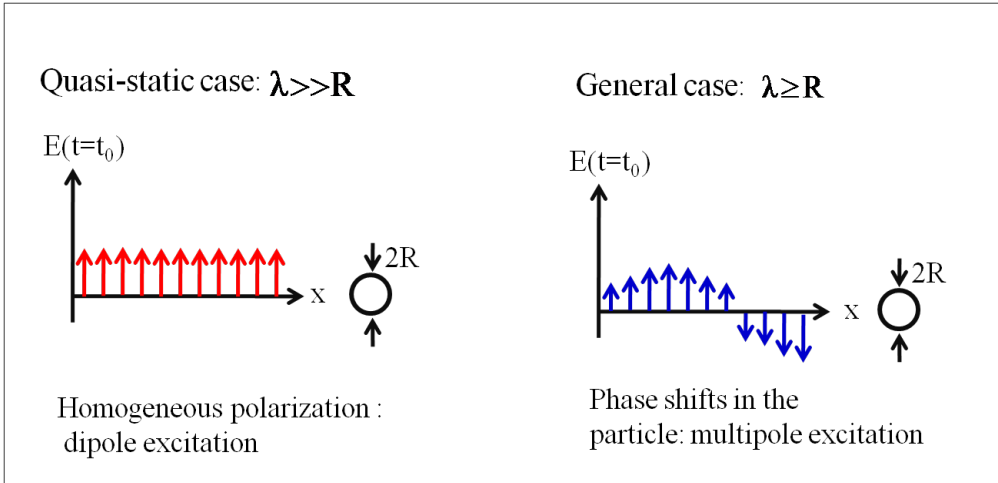


Figure 2.5: The interaction of light with clusters can be described in a simple way if $\lambda \gg 2R$, i.e. in the quasi static regime. For $\lambda \geq 2R$ retardation effects complicate the situation [41].

Whenever the size of the metal is squeezed to nano-dimension, the conduction electrons find themselves confined in a region much smaller than their characteristic distances. In the quasi-static regime i.e. under homogeneous excitation, the loosely bound conduction electrons experience a restoring force due to immobile positive ionic cores. The conduction electrons move in a *concert* like manner in response to the exciting electric field. Thus a time varying dipolar polarization is created at the surface, which oscillates at the frequency of the incoming light.

Using proper boundary conditions at the particle surface, one can calculate the polarizability α of the nanoparticle as well as the internal field E_{local} due an externally applied field, given by

$$\alpha = 4\pi\epsilon_0 R^3 \frac{\epsilon(\omega) - \epsilon_d}{\epsilon(\omega) + 2\epsilon_d} \quad (2.10)$$

$$E_{local} = \frac{3\epsilon_d}{\epsilon(\omega) + 2\epsilon_d} E_{ext} \quad (2.11)$$

here ϵ_d represents the dielectric function of host matrix.

We could infer from the above equations that at a particular frequency, the denominators of the above equation satisfy a singularity condition given by $[\varepsilon_1(\omega) + 2\varepsilon_d]^2 + [\varepsilon_2(\omega)]^2 = 0$, which refers to a resonance condition known as “Particle plasmon resonance”. Accordingly the resonant frequency ω_{spr} of the particle plasmon oscillation is given by $\omega_{spr} = \frac{\omega_p}{[1 + \varepsilon_1^b + 2\varepsilon_d]^{1/2}}$. Whenever the frequency of the incoming light coincides with the particle plasmon resonance, there is a huge flow of energy from the incoming field to the nanoparticle (figure 2.6(b)). But as the frequency moves away from the plasmon frequency the field is slightly perturbed at the vicinity of the particle surface (figure 2.6(a)) [4, 5, 41, 48].

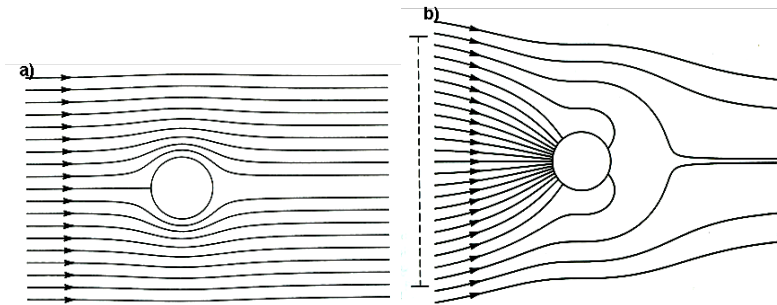


Figure 2.6: Field lines of the Poynting vector (quasi-static regime) around a small sphere illuminated by light of energy (a) away from plasmon resonance (b) at resonance [4].

As depicted in figure 2.6, the observed dielectric field enhancement at the surface plasmon frequency can be described in terms of local field factor f . In general the field factor for the dipolar excitation can be represented as

$$f = \frac{3\varepsilon_d(\varepsilon_1 + 2\varepsilon_d) - i(3\varepsilon_d\varepsilon_2)}{((\varepsilon_1(\omega) + 2\varepsilon_d)^2 + \varepsilon_2(\omega)^2)} \quad (2.12)$$

which is a complex quantity. To understand the physical significance of a complex natured field factor, one can define the local field factor f as the ratio between the two vector fields i.e. the ratio between the internal electric field and the applied field. For frequency $\omega \ll \omega_{spr}$ the dipolar field oscillates in phase with the external field where field factor is real and negligibly small in amplitude. But as the frequency of the incoming field is tuned towards the plasmon resonance an enhanced dipolar field is excited which oscillates $\frac{\pi}{2}$ out of phase with the incoming electric field; where the local field factor is imaginary which corresponds to a resonant absorption cross-section (figure 2.6(b)). As the frequency is tuned away from resonance $\omega > \omega_{spr}$ the phase factor will increase towards π .

2.3. LINEAR OPTICAL PROPERTIES OF NANOCOMPOSITE MATERIALS

In the far field, the particle plasmon resonance can be interpreted as dipolar absorption and the scattering phenomena. Light absorption and scattering of nanoparticles can be expressed through the frequency dependent cross-sections σ_{abs} and σ_{scat} :

$$\sigma_{abs}(\omega) = k \text{Im}(\alpha) = 4\pi k R^3 \text{Im} \left[\frac{\varepsilon(\omega) - \varepsilon_d}{\varepsilon(\omega) + 2\varepsilon_d} \right] \quad (2.13)$$

$$\sigma_{scat}(\omega) = \frac{k^4}{6\pi} |\alpha|^2 = \frac{8\pi}{3} k^4 R^6 \left| \frac{\varepsilon(\omega) - \varepsilon_d}{\varepsilon(\omega) + 2\varepsilon_d} \right|^2 \quad (2.14)$$

where $k = (2\pi/\lambda)$ represents the wavevector of the interacting plane wave.

In general the extinction cross-section of the nanoparticle is give by the sum of absorption and scattering cross-section as

$$\sigma_{ext}(\omega) = \sigma_{abs}(\omega) + \sigma_{scat}(\omega) \quad (2.15)$$

The dipolar extinction calculated for silver, gold and copper are shown in figure 2.7 (right). For silver nanoparticle the dipolar absorption band is peaked at 400 nm and for gold and copper nanoparticle the band is observed at 530 nm and 570 nm respectively. The broad absorption observed below 500 nm for gold and copper nanoparticle is associated with interband transitions. Compared to other noble nanoparticles, for silver the surface plasmon absorption band is located far away from interband transitions (310 nm) [5, 41].

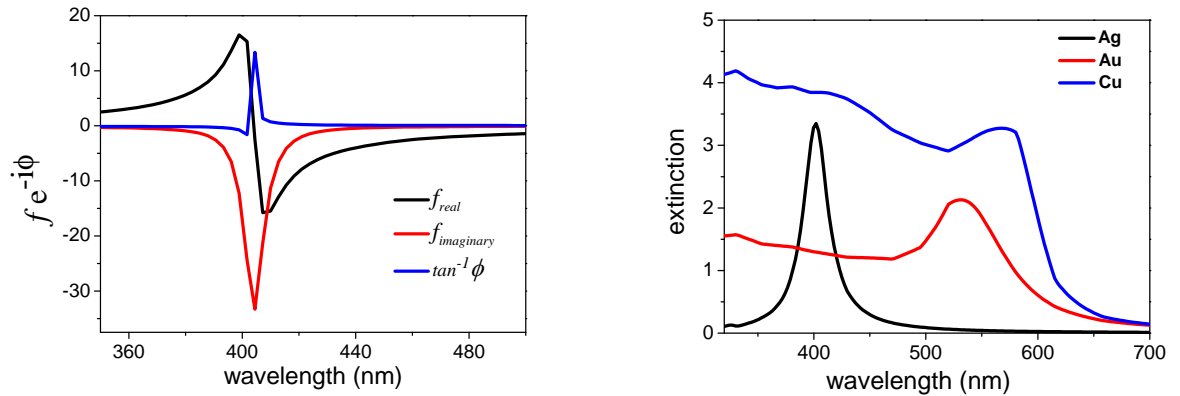


Figure 2.7: The real and imaginary parts of field enhancement factor f , together with the phase ϕ of local electric field (left), Dipolar-extinction spectra of glass containing spherical silver, gold and copper nanoparticles (right).

In general, any changes in the real ε_1 and imaginary parts ε_2 due to the variation

in the size and temperature strongly affects the position, width and height of the plasmon resonance to a considerable extent i.e.

(a) Changes in the peak positions $\Delta \lambda_{max}$ gives changes of ε_1 by

$$\Delta \varepsilon_1 = \left(\frac{d\varepsilon_1}{d\lambda} \right) \Delta \lambda_{max} \text{ at } \lambda = \lambda_{max}$$

(b) Changes of the peak height $\Delta \gamma_{max}$ gives changes of ε_2 by

$$\frac{\Delta \varepsilon_2}{\varepsilon_2} = - \frac{\Delta \gamma_{max}}{\gamma_{max}} \text{ at } \lambda = \lambda_{max}$$

(c) Changes of the band width $\Delta \Gamma$ gives changes of the refractive index by

$$\Delta n = A \Delta \Gamma \text{ at } \lambda = \lambda_{max}.$$

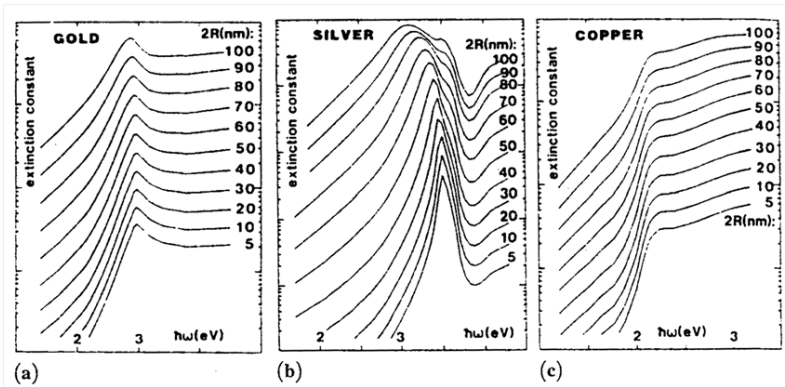


Figure 2.8: Calculated Mie extinction spectra of spherical nanoparticles of various metals. Parameter is the size $2R$. $\varepsilon_d=1$ [41].

For nanoparticles having size range of the order of 10 - 100 nm, the quasi-static approximation is not adequate to describe the optical properties of nanoparticles. One has to use the full electrodynamic calculations to describe the observed extinction spectra; in which the higher order multipoles cause a large retardation across the nanoparticle surface. For instance in figure 2.8(b) a secondary peak is observed due to the quadrupolar excitation in silver nanoparticles. With increasing size of the nanoparticle, the scattering (i.e, radiation damping) effects cause a huge red shift in the extinction cross-section [39, 41, 44].

2.3.4 Plasmon resonances of non-spherical nanoparticles

In the previous section we described the optical absorption and scattering of a spherical nanoparticle. A highly symmetrical spherical shape provides an isotropic

2.3. LINEAR OPTICAL PROPERTIES OF NANOCOMPOSITE MATERIALS

environment for free electron motion within the confined dimension; accordingly a dipolar absorption band is excited in the extinction spectra, which implies that any deviation in the geometrical structure can strongly affect the optical properties of the nanoparticles to a considerable extent. To learn about this aspect we have taken the particles having the simplest geometrical structure i.e. the “ellipsoidal geometry”. In general the geometrical surface of the ellipsoidal particles with semi axis $a \geq b \geq c$, is specified by $\frac{x^2}{a^2} + \frac{y^2}{b^2} + \frac{z^2}{c^2} = 1$. Using the electro-static approximation with proper boundary conditions, the polarizability of the ellipsoidal nanoparticle is given by

$$\alpha_j = v\varepsilon_0 \frac{\varepsilon(\omega) - \varepsilon_d}{\varepsilon_d + L_j(\varepsilon(\omega) - \varepsilon_d)} \quad (2.16)$$

where $v = \frac{4}{3}\pi abc$ is the volume, and L denotes the geometrical shape factor which describes the shape anisotropy of the nanoparticle. Hence for an ellipsoidal nanoparticle there are three independent components of polarizability α_j corresponding to each particle axis (hence three different L_j values). Special cases of ellipsoids are spheroids having two equal axial length along the semi-axis; therefore only one of the geometrical factors is independent. The geometry of the prolate(cigar-shaped) spheroid is defined as $b = c$ correspondingly $L_2 = L_3$, which are generated by rotating the ellipse along the major axis and for oblate (pancake-shaped) spheroids, it is $b = a$; $L_1 = L_2$ are generated by rotating an ellipse along its minor axis [5, 41].

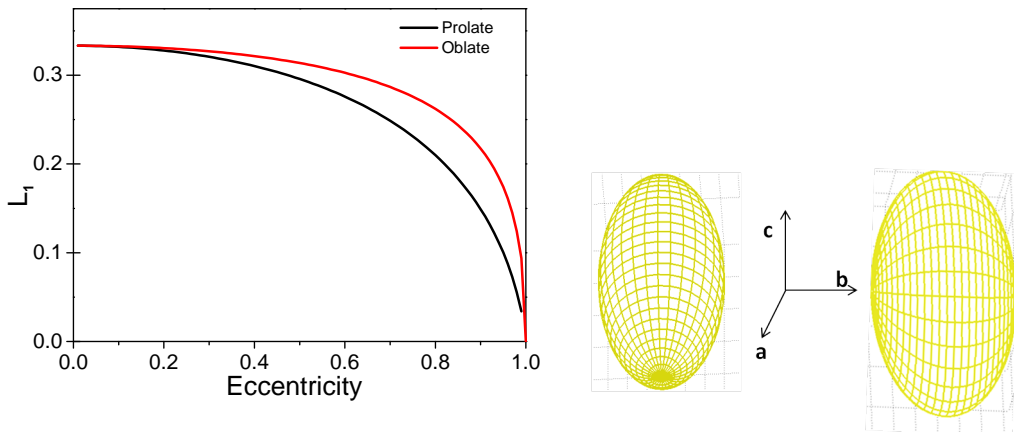


Figure 2.9: Geometrical factors for a spheroid (left) and corresponding geometrical structures of prolate & oblate spheroids(right).

The geometrical factor L , which is a measure of the geometrical sphericity of the

nanoparticle can be described in terms of the eccentricity e , i.e.

PROLATE ELLIPSOID ($b = c$)

$$L_1 = \frac{1 - e^2}{e^2} \left(-1 + \frac{1}{2e} \ln \frac{1 + e}{1 - e} \right); \text{ where } e = 1 - \frac{b^2}{a^2} \quad (2.17)$$

OBLATE SPHEROID ($a = b$)

$$L_1 = \frac{g(e)}{2e^2} \left[\frac{\pi}{2} - \tan^{-1} g(e) \right] - \frac{g^2(e)}{2}; \text{ where } g(e) = \left(\frac{1 - e^2}{e^2} \right)^{1/2} \& e^2 = 1 - \frac{c^2}{a^2} \quad (2.18)$$

Figure 2.9 shows the function variation of L_1 's with respect to the eccentricity of the nanoparticle. The oblate spheroid varies from a disc ($e = 1$) to a sphere ($e = 0$) and that of prolate spheroid ranges from needles to sphere [5].

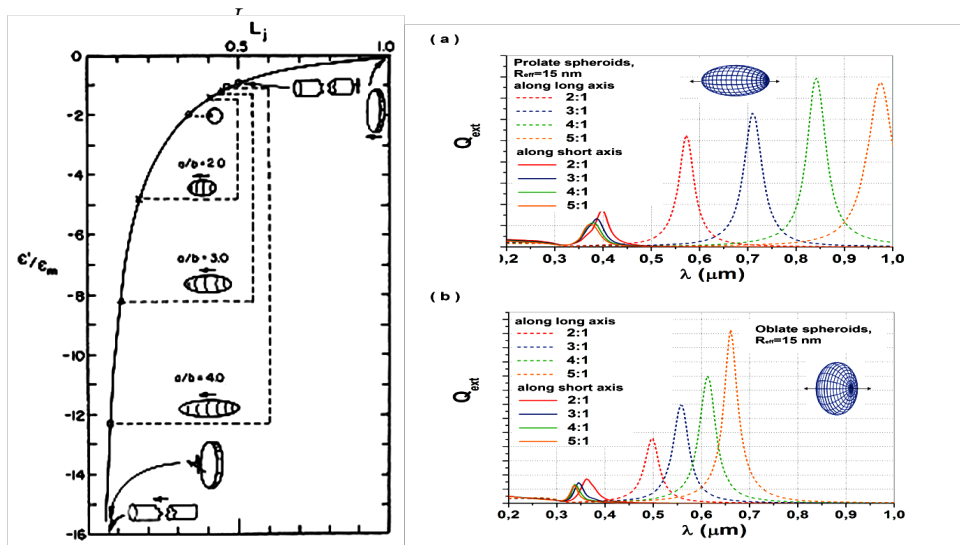


Figure 2.10: Effect of shape anisotropy on the spectral position of dipolar absorption. Arrows next to the various positions show the direction of the electric field (left) [5]. Extinction spectra calculated using the Mie theory for spheroids; polarized extinction spectra of prolate (a) and oblate (b) silver spheroids with different aspect ratios, which are embedded in glass. The volume of spheroids is equal to the volume of the nanosphere with radius of 15 nm. Dashed curves represent the polarization of the light is parallel to the long axis; solid line is that for light polarization parallel to the short axis. In insets, the shapes of spheroids are shown schematically (right).

Once we fix the type of metal and dielectric host matrix, the peak position of the dipolar absorption can be tuned to any desired spectral range by introducing the desired degree of geometrical anisotropy in the shape of the nanoparticle. As shown in figure 2.10 with developing the axial ratio of the semi axis, the peak position of the

absorption band is spanned from visible to infrared spectral region. Not only that, in contrast to spherical nanoparticles, its optical properties become highly sensitive to the polarization state of the incoming light.

For prolate spheroidal nanoparticles the absorption band splits into two, one corresponding to the long-axis of the ellipsoid known as longitudinal plasmon band which could be excited by choosing the light polarization parallel to the long axis of the particle. The second one known as transverse plasmon band corresponding to the short axis of the plasmon, which can be excited by choosing the light polarization perpendicular to it. The spectral gap between the band strongly depends upon the axial ratio of the nanoparticle (figure 2.10).

2.4 Effective nonlinear susceptibility of the metallic nanoparticles in glass

As we have seen from the previous section, the linear optical properties of the nanocomposite system are fully understandable through the knowledge of the composite dielectric function equally known as “effective dielectric function”. It is effective in the sense that its optical properties are extremely sensitive even to minor changes in the material parameters which constitute the composite system. We paraphrase the above statement in a functional form by $\varepsilon_{eff} = \varepsilon_{eff}(p, L, \varepsilon_m(\omega), \varepsilon_{glass}(\omega))$. Thus in the linear optical regime, drastic changes in the optical properties can be achieved either through a change in shape, size, concentration, the type of metal and the dielectric host matrix. A similar change can also be expected to occur in the nonlinear optical regime, this is exactly the point which we are interested in the present thesis work.

In the nonlinear optical regime, the photo induced changes in the dielectric function can act as a source [60, 20, 23, 58, 22] of nonlinear optical process. Under ultra-short laser pulse excitation, a transient change in the dielectric function of the nanocomposite system can occur through a change in the dielectric function of the constituent elements.

In general, such a physical situation can be represented using a power series expansion as given below

$$\varepsilon_{eff}(I) = \varepsilon_{eff} + \Delta \varepsilon_{eff} I + .. \quad (2.19)$$

Thus for a fixed volume fraction p and the shape L , the change can occur either due

to change in metal nanoparticle or glass dielectric function which can be represented as $\Delta \varepsilon_{eff} = \Delta (L, p, \varepsilon_m(\omega), \varepsilon_{glass}(\omega))$.

The first report on the optical nonlinearity of the nanoparticle was published in 1985 by Ricard et.al. Using the optical phase conjugation, under picosecond laser pulse excitation, their experiments could show a resonance enhancement of the order of 10^9 and 10^6 for gold and silver nanoparticles respectively. They categorize the resonant and non resonant interaction regime in context of local field factor $|f|$.

In an effort to understand the source of nanoparticle nonlinearity, they invoked three contributions to nano-particle nonlinearity: (i) a size dependent intraband contribution resulting from the confinement of conduction electrons; $\Delta \varepsilon(R)$ (ii) A size independent interband contribution arising from core-electron transition; $\Delta \varepsilon_{inter}$ (iii) The third one known as the hot electron contribution arising from the heating of conduction electrons due to laser pulse interaction, $\Delta \varepsilon_{hot}$.

$$\Delta \varepsilon'_{eff} = 3\pi Re\chi_m^{(3)} |E_{local}|^2 \quad (2.20)$$

$$\Delta \varepsilon''_{eff} = 3\pi Im\chi_m^{(3)} |E_{local}|^2 \quad (2.21)$$

Where the $\chi_m^{(3)}$ represents the intrinsic nonlinearity of the metallic particle which results from either of the three contributions

2.4.1 Intraband contribution

The intraband contribution is a size dependent contribution arising from the confinement of conduction electrons in the nano-dimension. Correspondingly the contribution is vanishingly small for nanoparticles having sizes of the order of 10 nm. This contribution is originally a dipolar one and expected to scale with the particle size as $\frac{1}{R^3}$ (provided R is sufficiently small). This contribution is calculated using a spherical box problem [21].

For our nonlinear studies, we have used nanoparticles having sizes of about 20 nm corresponding to a vanishing contribution from size dependent intraband transition.

2.4.2 Interband contribution

We have seen from section 2.3.2 that for noble metals, the interband contribution to the dielectric function is due to the transition of the inner core d-electrons to

conduction bands. The dielectric function calculated using the band structure model includes a strong resonance contribution which leads to a strong enhancement in the imaginary part of the dielectric function.

$$\chi^{IB} = \frac{8\hbar^3 \pi e^2}{m_{eff}^2} \sum \int \frac{2dk}{(2\pi)^3} |eP_{ij}(k)|^2 \times \left\{ \frac{1}{[E_j(k) - E_i(k)] [(E_j(k) - E_i(k))^2 - \hbar^2 \omega^2]} + i \frac{\pi}{2\hbar^3 \omega^2} \delta [E_j(k) - E_i(k) - \hbar\omega] \right\} \quad (2.22)$$

Where i and j refers to the various energy bands, $P_{ij}(k)$ is the matrix element of the momentum operator between the states corresponding to the quasi-momentum $\hbar k$, f_i and f_j are the occupation numbers and E_i and E_j are energies of the initial and final levels.

In the nonlinear optical regime, if the frequency of the interacting beam is in resonance with the certain interband transition, the main contribution to interband $\chi^{(3)}$ consists of a resonant contribution between the two corresponding levels. Accordingly the saturation of the two levels leads to a change in ε''_{inter} . The resulting $\chi^{(3)}$ is imaginary and its functional form is shown in equation

$$Im \left\{ \chi_{inter}^{(3)} \right\} = -\frac{4A T_1'}{3 T_2'} \frac{e^4}{m^4 \omega^4} \sum_{i,j} \int \frac{d^3 k}{4\pi^3} |P_{i,j}(k)|^4 \times f_i(k) (1 - f_f(k)) \frac{\pi T_2'^2}{2\hbar^2} \delta (E_j(k) - E_i(k) - \hbar\omega) \quad (2.23)$$

Unlike other noble metals in case of silver nanoparticles the spectral location of surface plasmon resonance (~ 2.9 eV for spherical nanoparticles) is far away from the interband transition energy (≥ 3.9 eV). Thus for the frequency range near to the surface plasmon resonance one can expect that nonlinear contribution arising from the imaginary part of $Im \left\{ \chi_{inter}^{(3)} \right\}$ are negligible. If at all the interband transition makes a contribution, it is the real part of $Re \left\{ \chi_{inter}^{(3)} \right\}$ which can be taken as a constant or “off-set” contribution to the total nonlinearity [20].

2.4.3 Hot electron contribution

The hot electron, a size independent contribution resulting from the heating of conduction electrons modifies the metallic dielectric function to a considerable extent. The corresponding nonlinear susceptibility can be expressed as

$$\chi_{he}^{(3)}(\omega) = \frac{2n_0(\omega)\varepsilon_0}{3I_0(\omega)} \Delta\varepsilon(\omega) \quad (2.24)$$

where $n_0(\omega)$ is the refractive index of metal, I_0 refers to the temporal maximum of the incident pulse intensity.

Whenever the energy of the laser pulse is absorbed by nanoparticles, their conduction electron distribution F is modified in the vicinity of the Fermi level, resulting in an increase in electron gas temperature. At equilibrium, $F = F_0$ is the Fermi-Dirac distribution at room temperature T_0 . Due to optical excitation, energy is instantaneously absorbed through intraband contributions, modifying the F near Fermi level. The system is out of equilibrium and it is impossible to ascribe a temperature to the electron gas. Internal energy redistribution takes place through electron-electron scattering and leads to a building up of Fermi Dirac distribution after a few hundreds of femtosecond at temperature $T_e > T_0$. At the same time the electron gas exchanges energy with the metal lattice through electron-phonon coupling until both are in quasi-equilibrium state. This step takes place on a time scale of few picoseconds.

On the time scale of the order of pump pulse duration, a large change in the electron temperature occurs without any change in lattice temperature. If the energy of the pump photon is shorter than the interband transition threshold, the energy transfer to the electron gas occurs through free carrier absorption, without perturbing the d-band electrons. A broad non-Fermi Dirac distribution with energy up to the pump photon energy above the Fermi level is created. The electron distribution change for instantaneous excitation and small perturbation is given by

$$\Delta\rho_{NT} = \Delta\rho_{NT}^0 \{f_0(E - E_p)[1 - f_0(E)] - f_0(E)[1 - f_0(E + E_p)]\} \quad (2.25)$$

where E is the electron energy, f_0 is the Fermi distribution at the initial sample temperature T_0 and E_p is the pump photon energy. The amplitude of the population change $\Delta\rho_{NT}^0$ depends upon the intensity of the pump. After the excitation, the energy is distributed among the electrons through electron-electron interactions, eventually leading to a hot electron distribution with temperature $T_e > T_0$. The figure 2.11 shows the instantaneous nonthermal population change $\Delta\rho_{NT}$ and corresponding thermalized (or Fermi) population change $\Delta\rho_{TH}$. The relative amplitude is calculated based on an assumption that all the energy stored in the initial non

thermal distribution is redistributed among the thermalized electrons without any loss to the lattice. [14, 20, 23, 44, 52, 62, 61, 19].

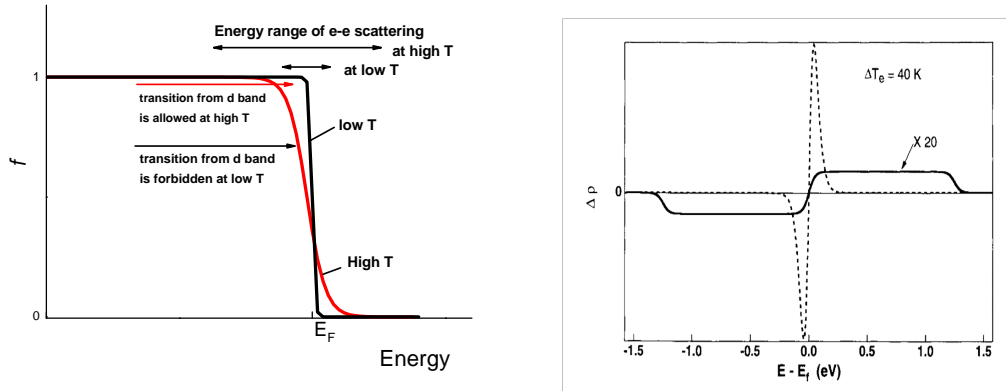


Figure 2.11: Fermi smearing mechanism. The solid line represents the Fermi Dirac distribution at low (black color) and high (red) temperature (left). Instantaneous electron distribution change $\Delta\rho_{NT}$ (solid line) created by free-carrier absorption of an infrared pump pulse and corresponding thermalized electron distribution $\Delta\rho_{T_h}$ (dashed line). $\Delta T_e = 40K$ represents the electron temperature rise (right) [73].

From the work of Hamanaka, Bigot [3, 23] it has been shown that a transient heating of the silver nanoparticle system results in a broadening and spectral shift of the plasmon resonance. We recall from the section 2.3.3 that any change in peak shift and broadening due to heating of conduction electrons results in a corresponding change in dielectric function. The observed spectral red shift and the broadening results in a change in both the real and imaginary parts of metallic dielectric function. The broadening arises from the damping of the plasmon resonance due to the collisional mechanism of the conduction electrons. The change in real part of the interband dielectric function leads to the nonlinear refraction.

As described in the above sections, the intrinsic nonlinearity of metallic systems shows a spectral dispersion near interband and intraband transition thresholds. In case of nanocomposite systems, if the pump photon energy lies far away from the absorption thresholds (interband and intraband), a positive nonlinearity originating from the hot electron contribution is observed. By tuning the pump photon energy near to the surface plasmon resonance, the sign and amplitude of the nonlinearity gets modified due to the complex natured local electric effects.

Using the Maxwell Garnett theory, the effective nonlinear susceptibility is represented as,

$$\chi_{eff}^{(3)} = p |f|^2 f^2 \chi_m^{(3)} \quad (2.26)$$

The above equation implies that effective nonlinearity is amplified to a considerable extent with the increase of local electric field. The latter parameter can be suitably controlled by tuning the material parameters of the composite systems. In this context, for our studies, we have suitably controlled the size, shape and concentration of the nanoparticles and analyzed carefully the effects of these constituent parameters on the nonlinearity of the nanocomposite system at different excitation regimes (both resonant and non-resonant) [52, 58, 60].

2.5 Saturation of Surface Plasmon oscillation under ultra-short excitation

The hot electron contribution described in the previous section can result in saturation of plasmon absorption. It has been established through pump-probe experiments that a coherent superposition of the electronic polarization of the nanoparticle and an electromagnetic field of the pump pulse is created immediately during the femtosecond excitation. Such a coherent situation can in principle decay due to radiative and non-radiative relaxation processes. The speed of the dephasing is characterized by the time constant T_2 (~ 10 fs), which is related to the time constant for inelastic decay of the population, T_1 , via $\frac{2}{T_2} = \frac{1}{T_1} + \frac{1}{T^*}$, where T^* describes the possible elastic phase loss processes of the plasmon. The physical scenario is depicted in figure 2.12. In case of resonant interaction of ultra-short laser pulses with the surface plasmon resonance (*SPR*) of nano-particles, ultrafast non-radiative relaxation processes on the femtosecond time scale cause heating of the conduction band electrons resulting in a damping of the plasmon oscillation. In the differential transmission measurements, the damping of the plasmon results in a transmission increase at the plasmon resonance. The bleaching of the plasmon resonance can be described in the frame of two level as explained in the section (2.2.1); i.e. when the broadening of the absorption is homogeneous, the absorption coefficient is related to the incident intensity through $\alpha(I) = \frac{\alpha_0}{1+I_\omega/I_s(\Delta)}$ where α_0 represents the unsaturated absorption coefficient and I_s the saturation intensity [20, 23, 26, 63, 54, 19].

2.5. SATURATION OF SURFACE PLASMON OSCILLATION UNDER ULTRA-SHORT EXCITATION

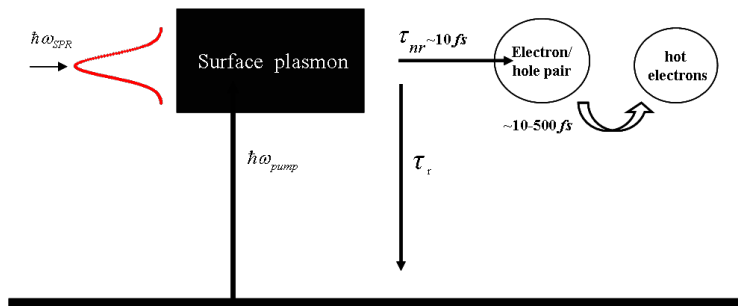


Figure 2.12: The scheme of the relaxation processes in a metallic nanoparticle[45]

By probing the wavelength dependence of the saturation intensity, one can know more about the strength of the nonlinear interaction processes. This issue has been addressed in detail in chapter 4.

Chapter 3

Experimental technique

The present chapter introduces the details of the samples, laser systems and the experimental setup employed for the nonlinear studies. The nanocomposite samples been used for the nonlinear studies were provided by CODIXX AG Germany. Commercially available laser systems from “Spectra Physics” and “Light Conversion” have been used for the nonlinear measurements. The details of the Femtosecond Z-scan technique and their applicability to the simultaneous measurement of nonlinear absorption and nonlinear refraction is given. A dual beam transmission spectrometer Shimadzu UV-3100 operating in spectral range of 200-1500 nm was used to measure the transmission spectra of the samples.

3.1 Preparation and characterization of nanocomposite materials

3.1.1 Glasses containing spherical nanoparticles

The glasses containing spherical nanoparticles are prepared by Ag^+ - Na^+ ion exchange technique followed by a subsequent reduction in hydrogen atmosphere. For the ion exchange process the glass substrate is placed in a mixed melt of AgNO_3 and KNO_3 at 400°C [59]. The thickness of the glass substrate, time of the ion exchange process and weight concentration of AgNO_3 in the melt determine the concentration and distribution of Ag^+ ions in the glass. Thermal annealing of the ion exchanged glass in H_2 reduction atmosphere, typically at $400\text{-}450^\circ\text{C}$, results in the formation of spherical silver nanoparticles. As could be expected, size and distribution of silver nanoparticles in the depth of the glass sample depend strongly on temperature and time of Na-Ag ion exchange as well as on the annealing time [2]. In our case, the spherical silver nanoparticles of 30-40 nm mean diameter [Figure 3.1(a)] are dis-

tributed in a thin surface layer of approximately $6 \mu\text{m}$ thickness (total thickness of glass plate 1 mm).

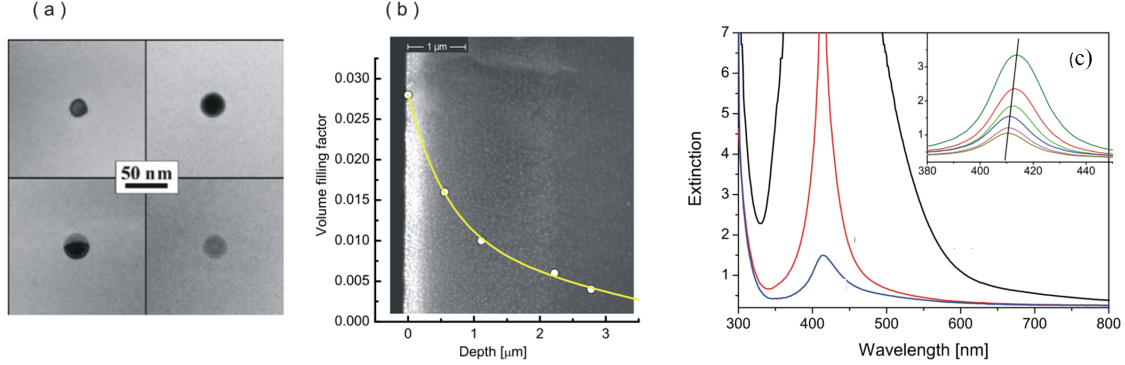


Figure 3.1: (a) TEM picture of typical spherical silver nanoparticles in nanocomposite glass. (b) SEM picture of the cross section of glass sample containing spherical silver nanoparticles (Ag particles are reproduced as white spots). The gradient of the volume filling factor of Ag nanoparticles is shown in superimposition (The x-axis was adjusted to the length scale of the picture) (c) Extinction spectra of samples with spherical silver nanoparticles after different time of etching in 12% HF acid. Images are taken from ref.[72].

Figure 3.1(b) shows the scanning electron microscopic (SEM) picture of the cross section of the sample, where silver particles are reproduced as white spots. To obtain an information about the distribution of silver nanoparticles in the depth of the glass, surface layers of various thicknesses from the sample were removed by etching in 12% HF acid for different retention times. Figure 3.1(c) represents the linear extinction spectra recorded from the respective etched area of the samples. After this procedure SEM images were recorded for all etched surfaces. The area fraction of silver derived from the SEM pictures was then converted to a volume fill factor assuming a typical electron penetration depth of 500 nm. The result is given as superimposed curve in figure. 3.1(b), showing the highest silver content of $f = 0.028$ directly below the glass surface. Within a few micrometers the fill factor decreases strongly with increasing distance from the surface [71].

3.1.2 Glasses containing ellipsoidal nanoparticles : Mechanically stretched nanoparticles

The glasses containing ellipsoidal nanoparticles are prepared by mechanical stretching method. Mechanical stretching of glass containing spherical silver nanoparticles was performed by applying a constant stress of $50\text{-}150 \text{ Nmm}^{-2}$ in a furnace at around 600°C . Applying a tensile deformation together with the heat treatment results in

3.1. PREPARATION AND CHARACTERIZATION OF NANOCOMPOSITE MATERIALS

ellipsoidal nanoparticles with a uniform orientation of the symmetry axis along the direction of deformation. One consequence of the used sample preparation technique is an overall reduction in the thickness of the sample; i.e. the thickness of both the glass and the particle layer have reduced to $200\ \mu\text{m}$ and $1\ \mu\text{m}$ respectively. As we described in chapter 2, the anisotropy in the shape of the nanoparticle is strongly sensitive to the polarization state of the interacting electro-magnetic radiation. To polarize the light in spectrometer and thereby measure the polarized transmission spectra, Glan prisms placed in the spectrometer were employed. In the polarized transmission spectra (figure 3.2(a)), the optical absorption of the spherical particles splits into two bands according to the long and short axis of the spheroid-shaped particles. The spectral position of the absorption bands are tuned by varying the initial size of the spherical particles and the degree of glass deformation determines the aspect ratio of the prolate particles [28].

Figure 3.2(b) represents a scanning electron microscopic (SEM) image of highly stretched nanoparticles. In the figure, the stretched direction of the sample is shown by the red arrow. A large size and shape distribution of nanoparticles with an average axial ratio (ratio between the semi-axis) of the order of 1:6 could be seen from the SEM image. The volume filling factor of the composite glass is calculated to be of the order of 2%.

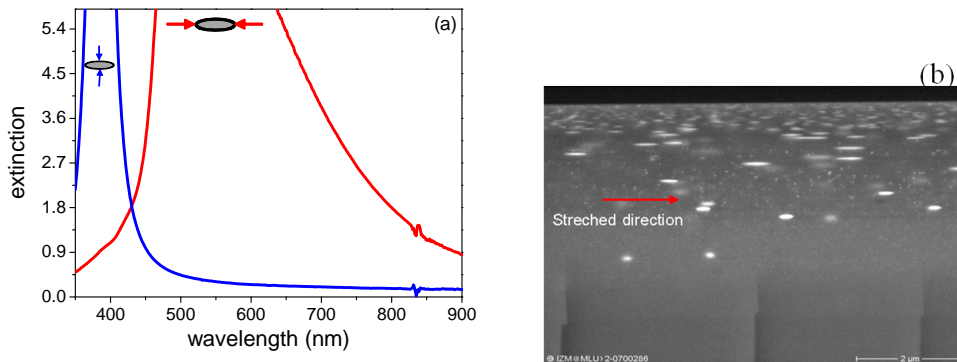


Figure 3.2: (a) The polarized extinction spectra of the sample. (b) The SEM image of highly stretched sample is shown in figure, the direction of the red arrow denotes the stretched direction of the sample.

3.1.3 Glasses containing ellipsoidal nanoparticles: Laser irradiated samples

In the previous section we have described that a shape deformation of nanoparticles from spherical to ellipsoidal can be achieved using the mechanical stretching method. It has been discovered that a permanent shape deformation of initially spherical metal nanoparticles embedded in soda-line glass to ellipsoidal (non-spherical) is realizable by irradiating the composite glass with intense femtosecond laser pulses near surface plasmon resonance. By choosing linearly polarized laser pulses, a dichroic behavior can be induced in the optical properties of the nanocomposite glass [37, 36].

The glass having low filling factor ($\sim 10^{-3}$) for the spherical silver nanoparticles (prepared via ion exchange technique and followed by annealing as described in section: 3.1.1) was used for the laser irradiation technique. Nanoparticles having average sizes of 30 nm diameter are distributed in a thin layer (thickness $\sim 1-2 \mu\text{m}$) within a thick glass substrate (thickness of glass 1 mm). The linear absorption spectra of the glass containing low dilution of spherical silver nanoparticles is shown in figure. 3.3(c: solid black line).

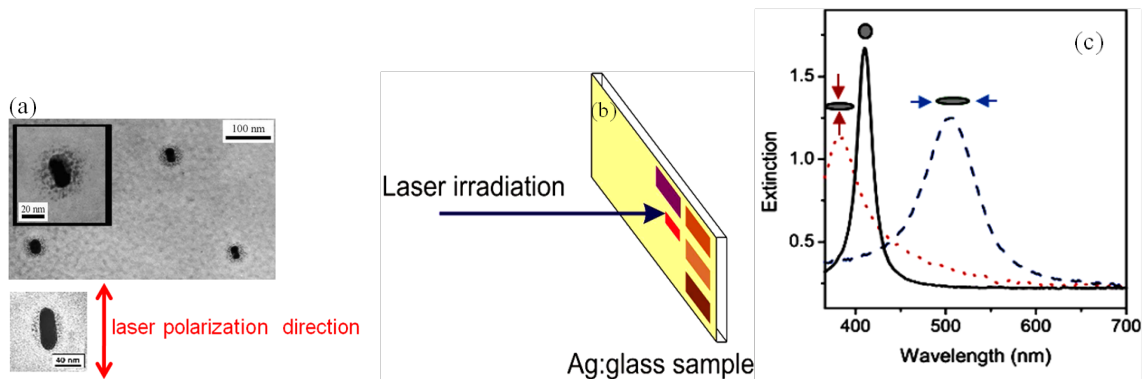


Figure 3.3: (a) TEM images of the deformed nanoparticles. The originally spherical shaped nanoparticles are modified into prolate spheroid with long axis parallel to the laser polarization direction .

Different colors of the irradiated areas can be produced by varying the irradiation parameters (b).The figure(c) shows the extinction spectra of the sample. The black solid line corresponds to the spherical nanoparticles, the blue (dashed line) and red (dotted line) line corresponds to polarized extinction spectra of the prolate spheroid with long axis parallel and perpendicular to the laser polarization direction. Images are taken from [35, 50].

The experimental configuration used for the laser irradiation technique is shown in figure 3.3(b). The laser irradiation technique changes the original color of the glass (the pale yellow) into darker colors. The different colors of the irradiated ar-

areas strongly depend upon the irradiation parameters such as the laser wavelength, the pulse intensity and the total number of pulses applied per area. The optical dichroism induced in the irradiated areas is a macroscopic consequence of the nanoparticle shape modifications. The transmission electron microscopic (TEM) image of the sample shown in figure 3.3(a) depicts that irradiating the nanocomposite glass with linearly polarized laser pulses can transform the initially spherical silver nanoparticles into elongated shapes (i.e. prolate spheroids) with their symmetry axes uniformly oriented along the laser polarization direction. Due to the shape modification, the original surface plasmon resonance is split up into two spectrally separated bands [50].

The physical background of the band splitting is associated with the electron oscillations parallel (longitudinal plasmon) and perpendicular (transverse plasmon) to the symmetry axis of the modified nanoparticle (figure 3.3(a)). The spectral gap between the nanoparticle is strongly dependent on the aspect ratio (particle axial ratio) of the nanoparticle. By varying the irradiation parameters, the aspect ratio of the nanoparticles can be adjusted to tailor the desired optical properties.

In the following sections, we will briefly introduce the laser systems and the laser pulse characteristics used for the nonlinear measurements.

3.2 Laser systems

For nonlinear measurements we have used different laser systems offering separate pump wavelengths having ultra short pulse duration. A commercially available Ti:sapphire laser with regenerative amplifier capable of delivering ultra short laser pulses is used. Ti:sapphire laser system mainly consists a mode-locked femtosecond oscillator “Tsunami” and a regenerative amplifier “Spitfire” (both are from “Spectra Physics”). The oscillator uses a Ti:sapphire laser rod as gain medium for femtosecond laser pulse generation. The pump laser is a cw diode pumped with $Nd:YVO_4$ laser with intercavity doubling at 532 nm. Pulses as short as 80 fs and energy up to few nJ, repetition rate 82 MHz, wavelength tunability from 740-820 nm is achieved. Pulses are spatially and temporally Gaussian.

In order to increase the pulse energy from oscillator up to ~ 50 mJ a regenerative amplifier is used. The working principle of the amplifier is based on the chirped pulse amplification, which is a method of generating very short pulses at high powers. The regenerative amplifier consists of three parts: the stretcher, the amplifier and

compressor. At first, the seed pulses from the oscillator are stretched in time to avoid catastrophic damages with very high peak powers during the amplification process. A single stretched pulse is allowed from the stretcher part to the amplifier cavity with the help of electro-optic modulator (Pockels cell). This pulse makes tens of passes through a Ti:sapphire rod, which is pumped by the Q-switched laser. Extracting much of the energy from the rod, a second Pockels cell sends pulses out of the cavity. The stretched and amplified pulse is then temporally recompressed back to its original duration of 100 fs with a grating compressor unit. At the end, the strong output pulses of the amplifier are almost transform-limited in time with a high beam quality.

Another femtosecond laser system named “PHAROS” is also used. This laser system works on the principle of chirped pulse amplification concept using laser diode-pumped Yb:KGW as active medium. The system comprises of Yb:KGW based master oscillator, regenerative amplifier and stretcher-compressor placed in a single enclosure. The output of the laser system operates at 1030 nm, 300 fs pulse duration with variable repetition rate tunable between 1 kHz to 350 kHz. Using a commercially available harmonic generator, 515 nm wavelength has been derived from the fundamental wavelength (1030 nm).

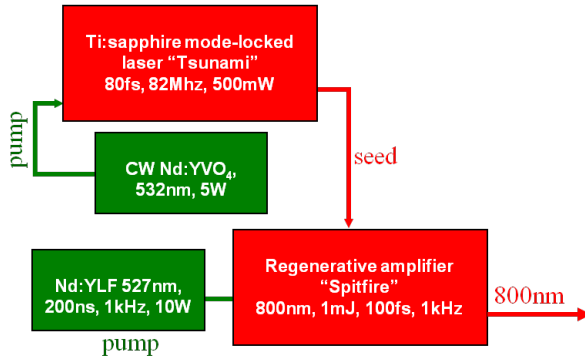


Figure 3.4: The scheme of the main laser system (Spectra Physics) used in this work.

Figure 3.5 shows the two-dimensional spatial profile of the laser beam (output from Spitfire-800 nm pump wavelength). The beam is focused by a 250 mm lens, and the image is recorded by a CCD camera at various positions along the beam propagation direction. The intensity distribution is best-fitted with the Gaussian function. It is clearly seen that the spatial beam profile matches a Gaussian profile with the fundamental TEM_{00} mode. The diameter $2W_0$ (beam width) of the Gaussian shape is defined at the position where the beam irradiance (intensity) has fallen to $1/e^2$

(13.5%) of its peak value and Z_0 the Rayleigh length of the focussed laser beam which signifies the distance from the focus at which the peak irradiance of the beam drops to half its value at the focus. Having the fundamental mode of the beam before focusing is very important in this sense, because at each focusing depth, the beam will retain its Gaussian character.

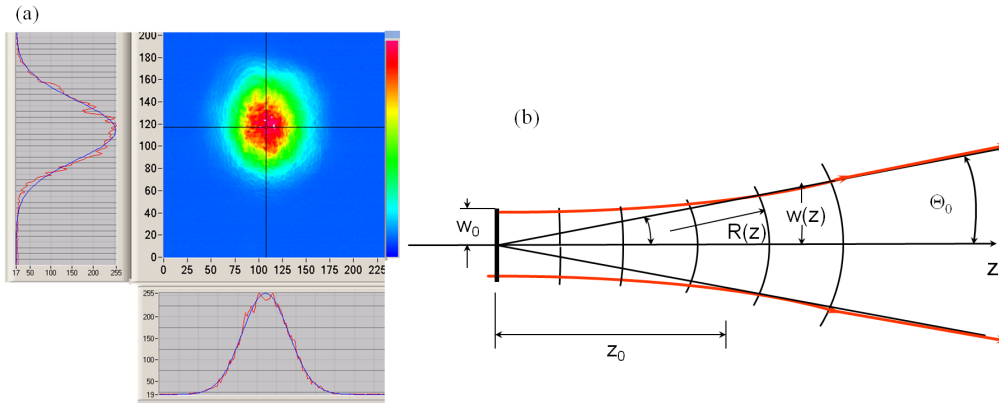


Figure 3.5: (a).Two-dimensional spatial beam profile of fundamental beam showing the TEM_{00} Gaussian mode. (b) The free space propagation of the Gaussian beam with a beam waist (spot size) of w_0 . The growth in w_0 (i.e. divergence) with the propagation distance is observed.

To examine the temporal characteristic of the pulses, a second harmonic generation frequency resolved optical gating was used. As an example, figure. 3.6 shows the SHG-FROG traces measured from Spitfire.

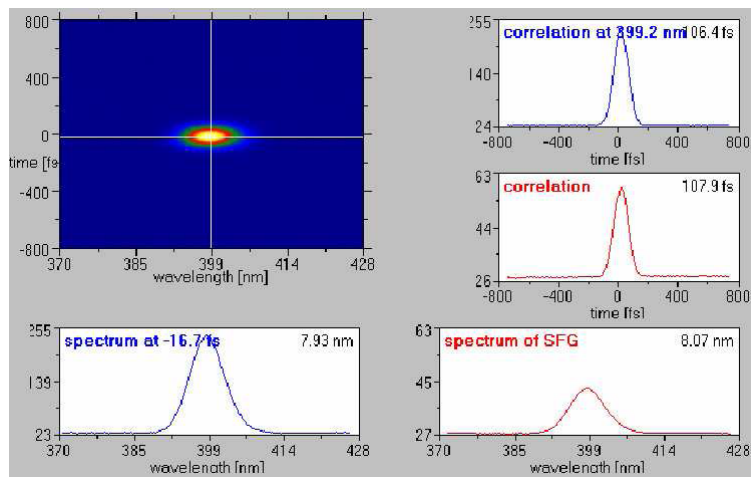


Figure 3.6: SHG-FROG trace, showing ~ 108 fs of pulse width together with the spectral information.

3.3 Measurement technique

3.3.1 Z-scan

Many techniques have been proposed for the measurements of nonlinear optical properties in the last few decades. For instance interferometric technique, degenerate four wave mixing, optical Kerr gate and beam distortion methods. The first three methods are potentially sensitive techniques, but all require relatively complex experimental apparatus. Beam distortion measurements, on the other hand, are relatively insensitive and require detailed wave propagation analysis.

Out of all these techniques the Z-scan gained rapid acceptance in the nonlinear optics community as a standard technique for separately determining the nonlinear changes in index and changes in absorption. This acceptance is primarily due to the simplicity of the technique as well the simplicity in the interpretation. The Z-scan is a single beam method, uses the principle of spatial beam distortion to measure both the sign and magnitude of refractive nonlinearities of optical materials, developed by Sheik-Bahae et al. in 1990. As shown in figure 3.7, the experiment uses the Gaussian beam from a laser in tight focus geometry to measure the transmittance of a nonlinear medium through a finite aperture in the far field, as a function of the sample distance Z from the focal plane; such a scheme is referred as “closed aperture” Z-scan (represented by the arm c in the figure 3.7). In addition to this, the sample transmittance without an aperture is also measured to extract the complementary information about the absorptive nonlinearities of the system which is called an “open aperture” Z-scan (represented by the arm b in the figure 3.7).

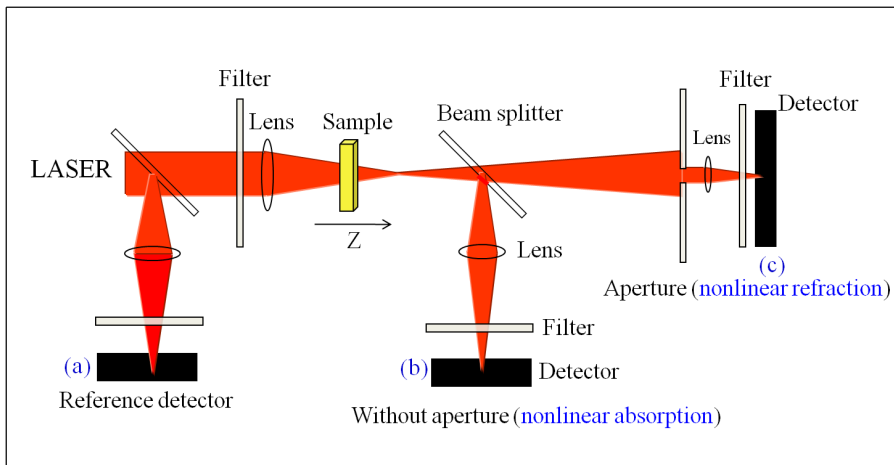


Figure 3.7: The schematic of Closed and Open aperture Z-scan setup

The principle of the Z-scan technique is to move the sample along the beam propagation direction of the focussed laser beam and measure the laser energy transmittance as a function of the sample position. For each position around the focus, the induced Kerr lens inside the sample has different focal lengths. As the sample is moved closer to the focus, the irradiance increases, leading to self-lensing in the sample. As illustrated in figure 3.8, the positive self-lensing in the sample placed before the focus moves the focal position closer to the sample resulting in a greater far field divergence and a reduced aperture transmittance. On the other hand, if the sample is placed after focus, the same positive lensing reduces the far field divergence allowing a larger aperture transmittance. Correspondingly a prefocal transmittance minimum (valley) followed by a postfocal transmittance maximum (peak) is the Z-scan signature of positive refractive nonlinearity (Figure 3.9(a) : blue solid line).

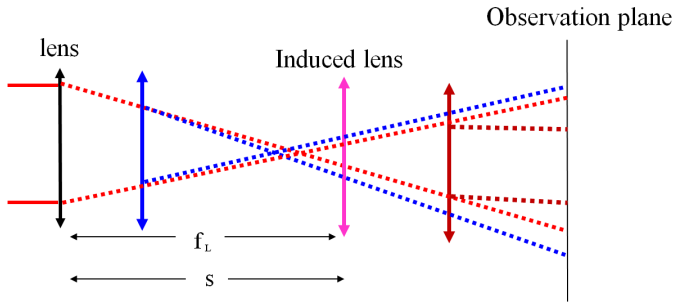


Figure 3.8: Geometrical optics analysis of Z-scan measurement for nonlinear refractive index.

In figure 3.7, a reference arm has been employed to account for the laser beam fluctuations between the experimental runs. The samples are scanned through the focal region of the sample by using a stepper motor driven translation stage. The energy of the laser pulse reaching the sample is appropriately controlled using the neutral density filters. The output transmittance from the sample is divided using a beam splitter and is directed towards two separate optical arms for the closed and open aperture scan measurements. The optical arm-c has been used for the closed aperture scan measurements in which a detector is placed in front of the aperture. On the other hand the nonlinear absorption measurements are performed using an open aperture (without aperture) scan as represented by the arm-b.

The opposite occurs for a self-defocusing nonlinearity, ($n_2 < 0$) (figure 3.9(a) : red solid line). On the other hand, a Z-scan with fully open aperture is insensitive to nonlinear refraction. Such Z-scan traces are expected to be symmetric with respect to focus ($Z=0$) where they have a minimum transmittance (multi-photon absorption)

and maximum transmittance (saturable absorption) (figure 3.9(b)).

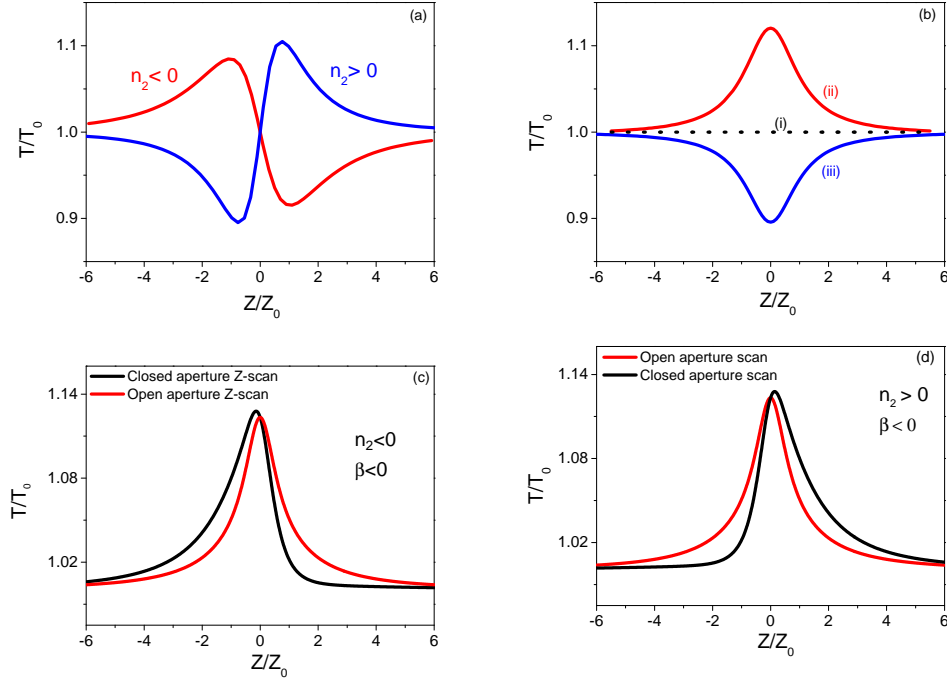


Figure 3.9: (a) Illustration of normalized Z-scan transmittance curve. The closed aperture Z-scan signal for pure nonlinear refraction ($n_2 > 0$ (blue solid line)) and negative nonlinear refraction $n_2 < 0$ (red solid line). (b) Open aperture Z-scan curve for (i) linear absorption (ii) saturable absorption $\beta < 0$ (iii) reverse saturable absorption $\beta > 0$. (c) Closed and open aperture curves (black and red solid line respectively) for $n_2 < 0$, $\beta < 0$ (d) $n_2 > 0$, $\beta < 0$.

3.3.2 I-scan

I-scan, an alternative technique for the measurement of optical nonlinearities in which neither the sample nor the detector is moved. This technique can be used for measuring the nonlinear properties of samples that are wedged, having surface irregularities. In I-scan technique, the sample is placed in the collimated focal region of a laser beam. By changing the amplifier current of the laser system, we have varied the input power in continuous steps. The incident and transmitted power through the sample is measured using powermeter. By measuring the beam radius at the local position of the sample, we calculated output intensity for each incident input power. For the I-scan measurement we used the Z-scan setup with sample rigidly placed within the Rayleigh range of the focussed Gaussian beam as shown in figure

3.10, where optical arm (a) represents the open aperture I-scan and arm (b) is that for closed aperture I-scan measurement.

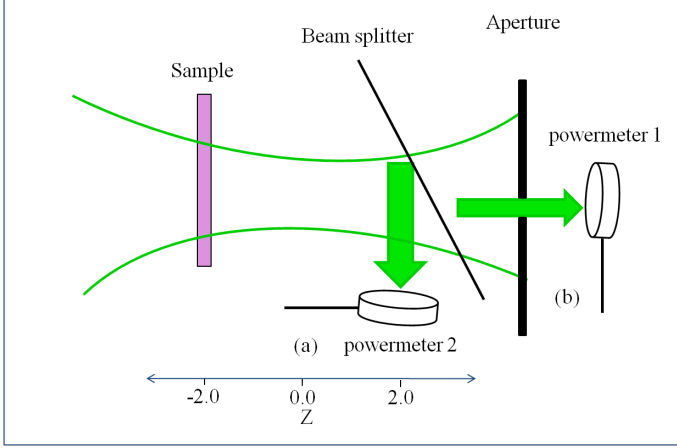


Figure 3.10: The schematic of Closed and Open aperture I-scan setup

3.3.3 Z-scan analysis for thin samples

For material possessing lowest order nonlinearity, i.e. materials having cubic non-linear refraction, where the index of refraction takes a functional form as given in equation 3.1

$$n(I) = n_0 + \frac{n_2}{2} |E|^2 \quad (3.1)$$

Here n_0 is the refractive index under low intensity illumination, E is the peak electric field and I denotes the irradiance of the laser beam within the sample. Assuming a TEM_{00} Gaussian beam of beam waist w_0 travelling in $+Z$ direction, we can represent E as

$$E(z, r, t) = E_0(t) \frac{w_0}{w(Z)} \exp\left(-\frac{r^2}{w^2(Z)} - \frac{ikr^2}{2R(Z)}\right) e^{-i\phi(Z,t)} \quad (3.2)$$

where $w^2(Z) = w_0^2(1 + Z^2/z_0^2)$ the beam radius, $R(Z) = Z(1 + Z^2/z_0^2)$ the radius of curvature of the wavefront at Z , $Z_0 = (\pi w_0^2/\lambda)$ the Rayleigh length of the beam, $k = \frac{2\pi}{\lambda}$ the wave vector and λ is the wavelength. $E_0(t)$ denotes the electric field at the focus which includes the temporal envelope of the laser pulse. The term $e^{-i\phi(Z,t)}$ contains all the phase variations that do not depend on the spatial transverse coordinate.

If the sample thickness is shorter than the diffraction length of the beam $L < Z_0$, the changes in the beam diameter within the sample due to either diffraction or nonlinear refraction can be neglected. Correspondingly the self-refraction effects from thin sample is referred to as “external self action” [38]. For nonlinear refraction this implies $L \ll \left(\frac{Z_0}{\Delta\phi_0}\right)$. Using the slowly varying envelope approximation, the amplitude and the phase of the electric field as a function of z' are governed by a pair of simple differential equations,

$$\frac{d\Delta\phi}{dz'} = \Delta n(I) k \quad (3.3)$$

$$\frac{dI}{dz'} = -\alpha(I) I \quad (3.4)$$

Here z' is the propagation depth within the sample and $\alpha(I)$ in general includes linear and nonlinear absorption parts and can be expressed as,

$$\alpha(I) = \alpha_0 + \Delta\alpha(I),$$

where α_0 is the linear absorption coefficient and $\Delta\alpha(I)$ is the nonlinear absorption of the material system, using the lowest order approximation $\Delta\alpha$ can represent as

$$\Delta\alpha(I) = \beta I$$

where nonlinear absorption coefficient β can take either of the signs, i.e. $\beta > 0$ represents the optical limiting mechanism on the other hand $\beta < 0$ leads to a saturable absorption mechanism.

Solving equations 3.3 and 3.4 simultaneously gives the phase shift at the exit surface of the sample which follows the radial variation of the incident irradiance

$$\Delta\phi(Z, r, t) = \Delta\phi_0(Z, t) \exp\left(-\frac{2r^2}{w^2(Z)}\right) \quad (3.5)$$

with

$$\Delta\phi_0(Z, t) = \frac{\Delta\Phi_0(t)}{1 + Z^2/Z_0^2} \quad (3.6)$$

$\Delta\Phi_0(t)$ is the on-axis phase shift at the focus, is defined as

$$\Delta\Phi_0(t) = k\Delta n_0(t) L_{eff} \quad (3.7)$$

where $L_{eff} = (1 - e^{-\alpha L})/\alpha$, with L the sample length and α the linear absorption coefficient.

The complex electric field of Gaussian beam at the exit of a nonlinear sample is given by

$$E_e(r, Z, t) = E(Z, r, t) \exp\left(\frac{-\alpha L}{2}\right) \exp(-i\Delta\phi(Z, r, t)). \quad (3.8)$$

The ‘‘Gaussian decomposition’’ method used by Weaire could give an analytic solution to certain approximations and provides a more clear physical interpretation [77]. By decomposing the complex electric field at the exit plane of the sample into summation of Gaussian beams through a Taylor series expansion of the nonlinear phase factor $e^{i\Delta\phi(r, Z, t)}$

$$e^{i\Delta\phi(r, Z, t)} = \sum_{m=0}^{\infty} \frac{[i\Delta\phi(r, Z, t)]^m}{m!}, \quad (3.9)$$

Now each Gaussian beam will simply propagated into the aperture plane where they will be re-summed to reconstruct the beam.

In general the normalized aperture transmittance is represented as

$$T_{NL}(z) = \frac{\int_{-\infty}^{\infty} dt \int_0^a |E_a(r, Z', \Delta\phi_0(t))|^2 r dr}{\int_{-\infty}^{\infty} dt \int |E_a(r, Z', \Delta\phi_0(t) = 0)|^2 r dr}. \quad (3.10)$$

Here E_a represents the electric field patteredn at the aperture.

For very small aperture, pure refractive nonlinearity and small nonlinear phase shift $\Delta\Phi_0$ only few terms in the summation are needed to make a good approximation, one can write out the result analytically. Following the simplifications, the normalized transmittance can be expressed as

$$T_{NL}(Z) \simeq 1 - \frac{4(Z/Z_0) \langle \Phi_0(t) \rangle}{(1 + (Z/Z_0)^2)(9 + (Z/Z_0)^2)}. \quad (3.11)$$

Chapter 4

Nonlinear optical properties of mechanically stretched nano-particles

4.1 Introduction

The surface plasmon assisted linear optical properties of metals in their nano dimension show drastic effects as compared to its bulk parent form. Dielectric field enhancement near surface plasmon resonance strongly boosts its optical properties. The strength of the field enhancement can be tuned by suitably engineering the nanocomposite materials. For instance introducing shape anisotropies in the geometrical structure of the nanoparticles makes the optical properties sensitive to the polarization state of the incoming electro-magnetic field. One can control the optical properties of the nanocomposite systems in a wide range by tuning the shape and size of the nanoparticle constituents. Hence to learn about the local field driven optical nonlinearity, we used glass containing ellipsoidal nanoparticles, in which the symmetry axis of the nanoparticles are found to be oriented along a common direction. By probing the samples of this kind we could understand the nonlinear optical properties in the resonant and non-resonant regime separately.

For studying the optical properties of the samples of this special kind, we recall the fundamental principle of interaction of light with matter which is given by

$$\langle n | V | m \rangle = -\overline{\mu(\vec{r})} \cdot \vec{E}(\vec{r}, t) \quad (4.1)$$

where equation 4.1 represents the matrix element associated with the eigen states $|n\rangle$ and $|m\rangle$ of the two level system which are coupled through the interaction potential $V(\vec{r}, t)$ and $\overline{\mu(\vec{r})}$ comprise the transition dipole moment of atomic (ma-

terial) system. We can infer from the above equation that only the portion of the electric field which is parallel to the transition dipole moment will interact with the system. By making use of this idea, we have properly chosen the orientation of the polarization state of the interacting laser pulse with respect to the symmetry axis of the nanoparticle.

4.2 Sample specification

The glasses containing ellipsoidal nanoparticles prepared by mechanical stretching method are used for the nonlinear measurements. The very speciality of the mechanical stretching method is the introduction of both microscopic and macroscopic geometrical anisotropy in the nanocomposite structure. The microscopic anisotropy is due to the particle shape deformation from spherical to the ellipsoidal one; and the preferential uniform orientation of the long axis of the ellipsoids results in a macroscopic anisotropy. The nonlinearity arising from the geometrical anisotropy of the nanoparticles is studied by choosing the suitable polarization state of the interacting laser beam.

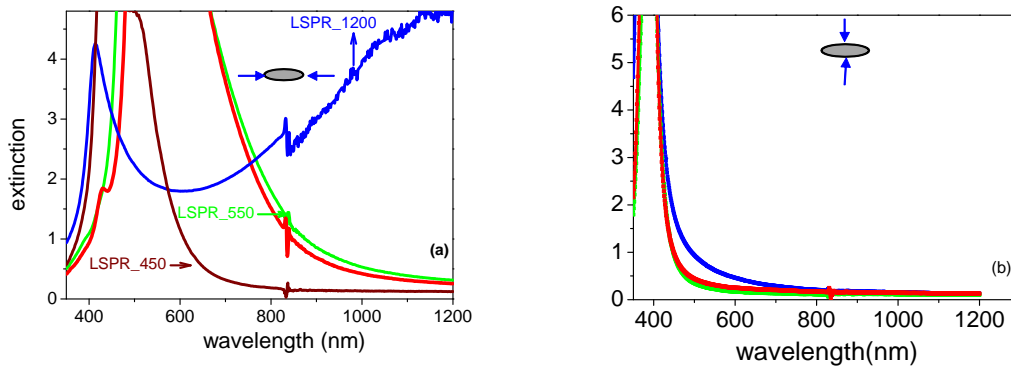


Figure 4.1: The polarized linear extinction spectra of the samples. (a) The extinction spectra of the samples with light polarized parallel to the long axis of the ellipsoid (b) the spectra with light polarized perpendicular to the long axis of the nanoparticle.

For nonlinear measurements, we have used four sets of samples with varying aspect ratio for the prolate ellipsoidal nanoparticles. The polarized linear extinction spectra of all the samples are shown in figure 4.1(a) and (b). The samples are named according to the peak positions of longitudinal surface plasmon band (LSPR). We could see from figure 4.1(a) that, for the sample named LSPR_1200 the longitudinal dipolar plasmon band (LSPR) is peaked at 1200 nm with an additional quadrupolar

absorption band at 420 nm. For other two samples (which are named as LSPR_550 and LSPR_450 respectively) the LSPR bands are peaked at 550 nm and 450 nm respectively. We have selected two sets of samples having same degree of structural anisotropy (LSPR_550, in figure 4.1(a) : green and red solid line) to check the consistency of nonlinear studies. The large broadening observed in the plasmon absorption band is attributed due to the broad size distribution of nanoparticles. In the perpendicular polarization the transverse surface plasmon bands (TSPR) of all the four samples are peaked around 390 nm (figure 4.1(b)).

4.3 Nonlinear optical measurements

The experimental configuration used for the nonlinear measurement can be suitably modified in accordance with the symmetry of the of nanocomposite system. In case of the prolate ellipsoidal nanoparticles, the shape anisotropy assigns different polarizability along the short and long axis of ellipsoid (reference: chapter 3). To study the properties arising from the different plasmon bands we changed the orientation of the long axis of the ellipsoid with respect to laser polarization direction.

As depicted in the figure 4.2, a propagating electric-field \vec{E} which is polarized along \vec{z} direction makes an angle θ with the long axis of the ellipsoid (equally with the stretched direction of the sample). For nonlinear measurements, the laser polarization is kept along z -axis and the angular orientation of the long axis of the ellipsoid is changed with respect to the laser polarization direction (figure 4.2 and 4.3). At $\theta = 0^\circ$ the stretched direction of the sample is found to be parallel to the laser polarization direction, we call it to be the parallel configuration (\parallel) and a perpendicular configuration (\perp) is realized at $\theta = 90^\circ$.

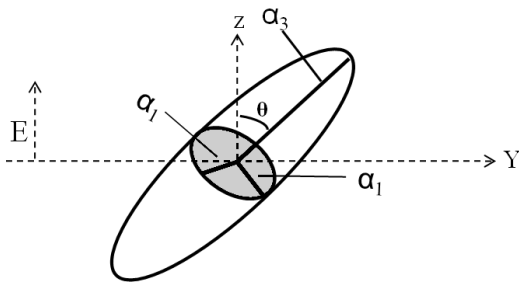


Figure 4.2: The Electric field vector and the direction of the dipolar polarizabilities of a single nanoparticle in the sample during optical absorption measurement.

Femtosecond Z-scan technique is employed for the nonlinear measurements. The details of the experimental setup is described in chapter 3. The excitation wavelengths were chosen to be 1030 and 800 nm with pulse durations of 300 fs and 100 fs, respectively. Both the laser systems were operated at 1 kHz repetition rate in order to avoid the accumulated heating effects in the focal volume. The Rayleigh range of the laser beams are measured to be 2 mm or 3 mm respectively for 800 nm and 1030 nm pump wavelength which is one order of magnitude greater than the thickness of the sample. Hence a thin sample approximation is valid irrespective of the excitation parameters. The spatial intensity profile of the laser beams are measured using CCD camera which confirms it to be nearly spatially circular Gaussian. The pulse energy of the laser beam is controlled by neutral density filters. Prior to collecting the data, the system is calibrated to ensure the linearity between all three detectors over the entire range of available energy.

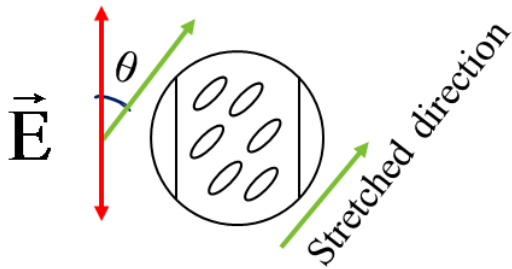


Figure 4.3: The experimental configuration used for the Z-scan measurement. The green line indicates the preferential orientation of the long axis of the nanoparticles and red line represents the laser polarization direction.

4.3.1 Experimental results and Fitting procedure

The figure 4.4 shows an open and closed aperture Z-scan measurement performed on LSPR_550 at 1030 nm excitation. In the \parallel configuration, the open aperture Z-scan (figure 4.4(a)) curve shows an increase in transmission peaked at the focal point of the lens, with an offset value for the linear transmission. Similar kind of feature is observed at closed aperture scan (figure 4.4(b)) for intensity $I_0 \leq 10 \text{ GWcm}^{-2}$. In the closed aperture scan an asymmetric feature starts to dominate at higher excitation intensity ($I_0 \geq 10 \text{ GWcm}^{-2}$) (figure 4.4(b) : green circles) which indicates the presence of nonlinear refractive effects. As already discussed

in chapter 3 (section 3.3), the closed aperture Z-scan curve is sensitive to both nonlinear refraction as well as nonlinear absorptive process. To separate out the contribution due to the nonlinear absorption we have employed a symmetrization technique [1, 2, 3] the details of which are available in the appendix-A.1. We observed a saturable absorption together with a negative nonlinear refraction at the open and closed aperture scan in the \parallel configuration (figure 4.6(a) and (b), black open circles). The nonlinear contribution measured from the glass substrate is found to be negligibly small and has thus not been taken into account in the \parallel configuration.

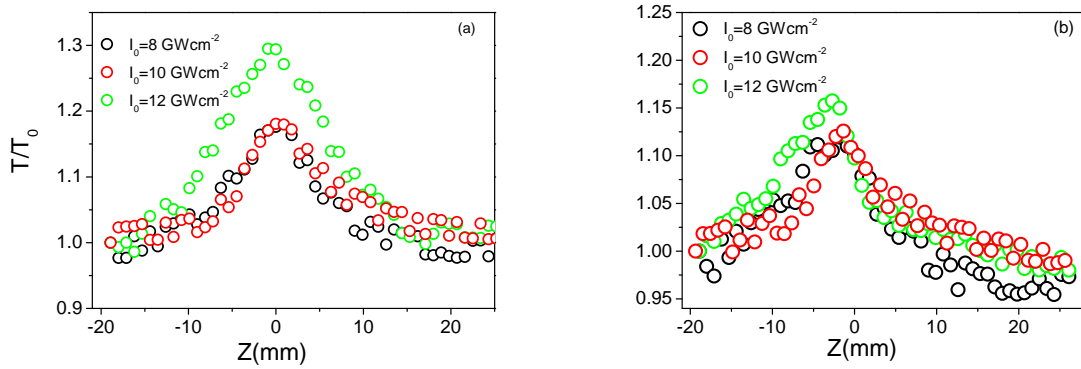


Figure 4.4: Figure (a) & (b) shows the open and closed aperture Z-scan measurements performed on LSPR_550 under 1030 nm excitation at the \parallel configuration.

Figure 4.5 shows the energy level scheme used for analyzing the Z-scan experimental results. The broad dipolar absorption bands of LSPR_1200 and LSPR_550 are represented in the figure by the blue and red solid curve. The red and black upward arrows indicate the spectral location of 800 and 1030 nm photon with respect to the plasmon band absorption. The spectral gap between the LSPR and TSPR band and pump excitation wavelengths are defined by $\hbar \Delta = \hbar (\omega_{spr} - \omega_{pump})$. From the above depiction it is clearly visible that in the \parallel configuration, the laser pulse interacts with LSPR band through single photon absorption process and correspondingly the nonlinear interaction falls in the near resonant regime. Also we can keep in mind that the strength of the nonlinear interaction is strongly dependent on the spectral gap, pulse energy and the pulse duration of interacting laser pulse.

In order to understand the origin of optical nonlinearity, a model based on the resonant interaction of electro-magnetic field with LSPR band is implemented in the \parallel configuration. When the energy of incoming photon corresponds to the single photon absorption cross-section; the system can be approximately described as two-level

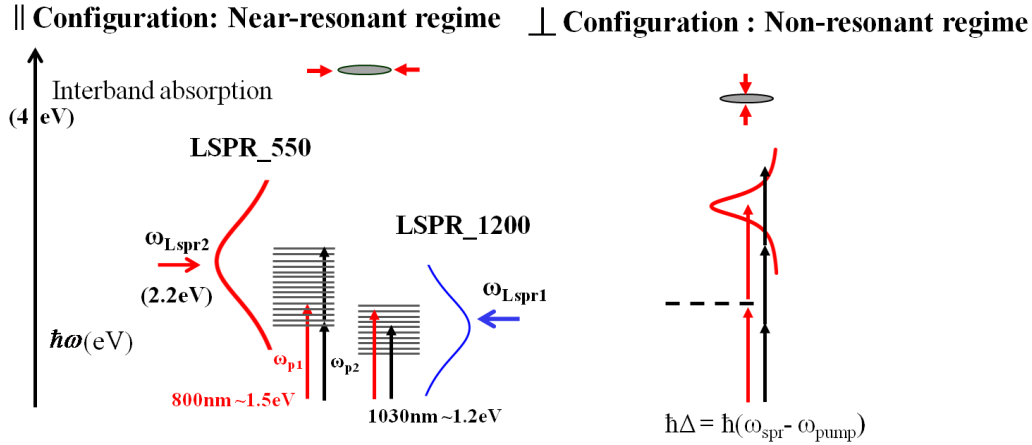


Figure 4.5: Energy level scheme used for the analysis of the plasmon in the near resonant regime. The broad Plasmon resonance decays into an electron or lattice heat bath. The board band (red continuous line) represents the SPR bands of LSPR_550 in the || and \perp configuration. The blue band represents that for sample LSPR_1200 in || configuration. The red and black arrow symbolizes the spectral position of 800 and 1030 nm pump wavelength with respect to plasmon band.

model; in which the ground state plasmon represents the lower state and the excited broad plasmon represents the upper state. To quantify the basic mechanisms responsible for nonlinear absorption we have defined an effective nonlinear absorption coefficient $\alpha(I)$

$$\alpha(I) = \left[\frac{\alpha_0(\Delta)}{(1 + (I/I_s(\Delta)))} \right] \quad (4.2)$$

where $\alpha_0(\Delta)$ is the unsaturated linear absorption coefficient, $I_s(\Delta)$ is the saturation intensity at pump excitation wavelength. For calculating the output intensity for a given input, we numerically evaluated the output intensity from the sample for each input by solving the propagation equation.

$$\frac{dI}{dz'} = -\alpha(I) I \quad (4.3)$$

A fourth order Runge-Kutta method is employed for solving the above differential equation [78]. For the numerical calculation, we treated the total sample thickness ($1 \mu m$) is composed of very many thin slices of thickness $\Delta z'$ and carefully analyzed how the laser pulse advance into given slice first, and then into the inner slices. The normalized transmittance is then calculated by dividing the output intensity with input intensity and then normalizing it with linear transmittance. By performing this numerical calculation for various Z-positions, we could calculate the transmittance

of the sample as a function of Z . Using the least square fit method, the saturation intensity I_s is estimated from the open aperture scan (figure. 4.6(a)) which is found to be 25 GWcm^{-2} where sample linear absorption coefficient is $0.59 \mu\text{m}^{-1}$. In figure 4.6(a), the open circles shows the experimental data points and solid line represents the corresponding theoretical fit.

The closed aperture data obtained through the symmetrization technique includes the contribution due to pure nonlinear refractive effects. Using a thin sample approximation, the experimental closed aperture transmission curve (figure. 4.6(b)) is fitted well with the n_2 process

$$T(z, \Delta \Phi_0^{(3)}) = 1 + \frac{4 \Delta \Phi_0^2 / z_0}{\left[(z/z_0)^2 + 9 \right] \left[(z/z_0)^2 + 1 \right]} \quad (4.4)$$

where the nonlinear phase shift given by $\Delta \Phi_0 = \left(\frac{2\pi}{\lambda} \right) n_2 I_0 L_{eff}$. The fitted value of n_2 is $-15 \times 10^{-17} \text{ m}^2/\text{W}$. The possible errors in the value of nonlinear coefficients can occur either due to the fluctuations in spatial beam profile and pulse duration between different experimental runs, uncertainty in the knowledge of laser pulse energy, beam waist size, spatial and temporal shapes. The measurements are repeated on different sample areas and the fitted values of nonlinear parameters are found to be consistent within 10% error value.

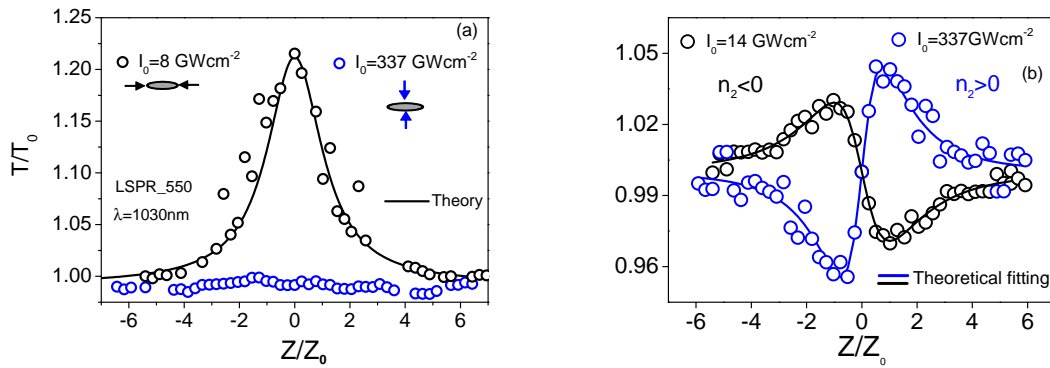


Figure 4.6: Figure a & b represents the open aperture and closed aperture Z -scan curves measured in the \parallel and \perp configuration (sample LSPR_550, 1030 nm excitation). Open points represent the experiment data points and continuous line correspond to the theoretical fit

In the \perp configuration, the short axis plasmon (transverse plasmon) alone will contribute to the nonlinear optical process. The transverse plasmon, which is peaked at 390 nm (3.1 eV) may interact with laser photons (1.2 eV) through multi photon absorption process; which concludes that while shifting from \parallel to the \perp configuration,

the nonlinear optical interaction process switches from near-resonant to the non-resonant interaction regime. The excitation intensity used in the \perp configuration is 40 times larger than the value used in the \parallel configuration. The respective Z-scan experimental results are shown in figure 4.6.(a) and (b) (blue open circles). While switching from \parallel to \perp configuration, we could observe a sign reversal in nonlinear refraction, i.e. in the \perp configuration, a positive nonlinear refraction is observed at the closed aperture scan along with a negligible absorption at the open aperture scan.

In the \perp configuration, to discriminate the contribution due to the glass nonlinearity, we compared the nonlinear transmission measured from the pure glass substrate with that of sample transmission. From polarized linear absorption spectra (figure 4.1(b)), we could see that, the 1030 nm excitation wavelength is not in resonance with two or three photon absorption process, which explains the observed negligible absorption at the open aperture scan. In comparison, we found that the transmission change ΔT ($T_{peak} - T_{valley}$) measured from the glass substrate is not negligible as compared to the transmission change measured from the sample and hence at this excitation wavelength the contribution from glass nonlinearity also plays a pre-dominant role.

In order to study the nonlinear contribution from TSPR band, we used $\lambda_2 = 800$ nm pump wavelength with a pulse duration of 100 fs. In non-resonant regime we could see from figure 4.5 that the excitation wavelength is two photon absorption resonant with TSPR band; the effective nonlinear absorption of the sample is defined to be $\alpha(I) = \alpha_0 + \beta_{\perp}I$ where β_{\perp} represents the two-photon absorption coefficient in the \perp configuration. Exciting the sample at higher intensities shows a transmission decrease at the focus in the open aperture scan due to the two photon absorption along with a positive nonlinear refraction at the closed aperture scan. Switching from \parallel to \perp configuration thus shows a sign reversal in nonlinearity for both nonlinear absorption and refractive process and the corresponding Z-scan measurements are shown in figure 4.7. In the \parallel configuration the fitted values of nonlinear coefficients n_2 and I_s are found to be $-15 \times 10^{-17} \text{m}^2/\text{W}$, 15.5 GWcm^{-2} , for \perp configuration the fitted values of $n_{2\perp}$ and β_{\perp} are given by $1 \times 10^{-17} \text{ m}^2/\text{W}$ and $1 \times 10^{-11} \text{ m}/\text{W}$ respectively. In the \parallel configuration a strong negative nonlinear refraction along with a saturable absorption is observed. Hence we could conclude from the above observation that switching the sign of nonlinearity is closely connected with the geometrical shape anisotropy of the nanoparticle system.

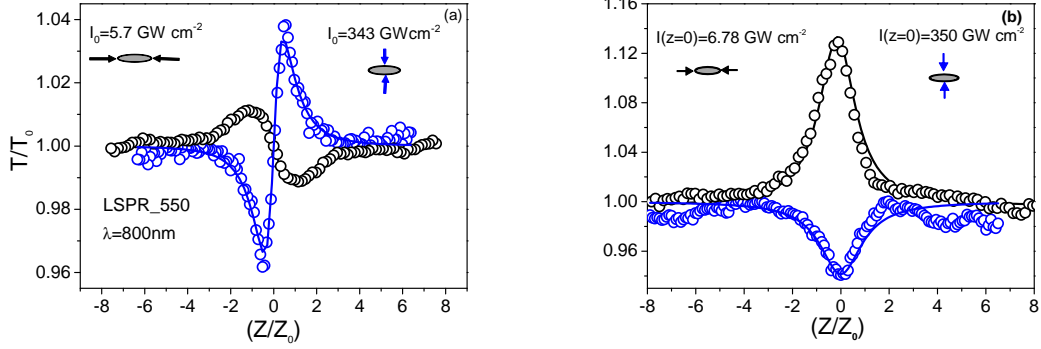


Figure 4.7: Figure a & b shows the closed aperture and open aperture Z-scan curves measured in the \parallel and \perp configuration for LSPR_550 under 800 nm excitation. Open points represent the experimental data points and continuous lines correspond to the theoretical fit.

4.3.2 Sign reversal in nonlinearity: (Qualitative description) Hot electron contribution

In this section we will discuss the physical origin of the sign reversal in the nonlinearity while switching from the \parallel to the \perp configuration. From equation. 4.2, the incoherent nonlinear absorption under zeroth order approximation ($I < I_s$) [47], can be represented as

$$\alpha(I) = \alpha_0 - \left(\frac{\alpha_0}{I_s}\right)I + \beta_{\perp}I = \alpha_0 - \beta_{\parallel}I + \beta_{\perp}I \quad (4.5)$$

in which the saturation intensity follows a spectral dependence of the following form

$$I_s = I_s^0 \left(1 + \Delta^2 T_2^2\right) \quad (4.6)$$

where β_{\parallel} and β_{\perp} represents the resonant and non-resonant nonlinear absorption coefficients and T_2 determines the dephasing time of the coherent electron oscillation.

In the \parallel configuration, a bleaching of the surface plasmon band is observed immediately after the excitation. Due to the shape anisotropy, as we switch over from \parallel to the \perp configuration, the spectral gap changes from a minimum to a maximum value i.e. by changing the angular orientation θ , the pump wavelength moves away from the resonance leading to an increase in the value of the saturation intensity I_s .

For instance under 1030 nm excitation, while switching between two interaction regimes, the spectral gap changes from 1.05 eV to 2 eV and the corresponding value

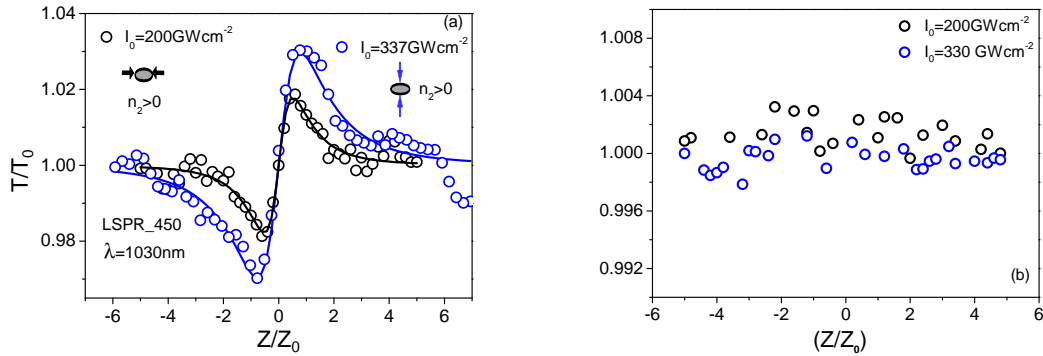


Figure 4.8: Figure a & b shows the closed aperture and open aperture Z-scan curves measured for sample LSPR_450 under 1030 nm excitation in the \parallel and \perp configuration. Open points represent the experimental data points and the continuous lines represent the theoretical fit the experimental data points.

of saturation intensity in the \parallel configuration is found to be 25 GWcm^{-2} ; while by rotating through 90° results in an excitation of the sample in its transparency regime which intuitively imposes an infinitely large value for the saturation intensity. A similar argument is found to be valid for 800 nm pump wavelength, where switching the light interaction regime changes the spectral gap from 0.7 eV to 1.63 eV. The fitted nonlinear parameters in the parallel configuration are $n_{2\parallel} = -15 \times 10^{-17} \text{ m}^2/\text{W}$ and $\beta_{\parallel} = -10.68 \times 10^{-9} \text{ m}/\text{W}$. The parameters obtained in the perpendicular configuration are $n_{2\perp} = 1 \times 10^{-17} \text{ m}^2/\text{W}$ and the value of the two photon absorption coefficient is calculated to be $\beta_{\perp} = 2.2 \times 10^{-11} \text{ m}/\text{W}$. The macroscopic anisotropy factor for the nonlinear absorption for 800 nm excitation is given by $|\frac{\beta_{\parallel}}{\beta_{\perp}}| = 200$ and the corresponding ratio of intensities used to excite the LSPR to TSPR band is 1:38 [43].

For a fixed excitation wavelength the value of spectral gap Δ between the pump wavelength and plasmon band (equally the type of nonlinear interaction) is decided by the shape anisotropy factor of the nanoparticle and represented by $\Delta = \Delta(\lambda_{fixed}, L_i)$. To understand this point, we have performed nonlinear measurements on LSPR_450 (Figure 4.8(a) and (b)). For 1030 nm excitation, the experimental results show a positive nonlinear refraction irrespective of the interaction regime along with a zero nonlinear absorption. While switching from \parallel to the \perp configuration, the value of the spectral gap Δ changes from 1.5 eV to 1.9 eV. In the \parallel configuration, the 1030 nm excitation is completely out of surface plasmon resonance (figure 4.1), the laser pulse interacts with nanoparticle system through infrared absorption of free

electrons which leads to a change in dielectric function $\Delta \varepsilon_1$ due to the heating of conduction electrons (Drude contribution) resulting in a positive optical nonlinearity due to hot electron contribution. From the linear absorption spectra, we could see that for sample LSPR_450 the spectral distance between the LSPR and TSPR band is 0.4 eV, corresponding to a nanoparticle aspect ratio (ratio of semi major axis to semi minor axis) of the order of 1 : 1.4. Such a small aspect ratio assumes a less degree of shape anisotropy in the nanocomposite structure and thus it is slightly sensitive to the linearly polarized infrared laser pulse.

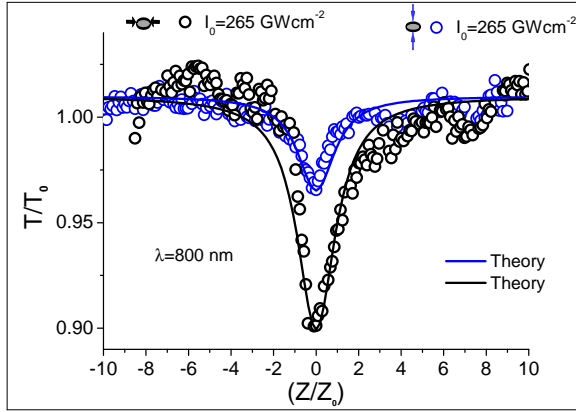


Figure 4.9: Figure shows the open aperture Z-scan curves obtained for sample LSPR_450 under 800 nm excitation in the \parallel and \perp configuration. Open points represent the experimental data points and the continuous lines represent the theoretical fit to the experimental data points.

For 800 nm excitation a positive nonlinear absorption (optical limiting mechanism) due to two-photon absorption is observed in both experimental configurations (\parallel as well as \perp). The anisotropy factor for nonlinear absorption is calculated to be $\frac{\beta_{\parallel}}{\beta_{\perp}} = 2.8$, where $\beta_{\parallel} = 2.89 \times 10^{-11} \text{ m/W}$, $\beta_{\perp} = 1.02 \times 10^{-11} \text{ m/W}$. In comparing to the sample LSPR_550, we could see that for sample LSPR_450 the shape anisotropy plays a minor role in overall nonlinear process.

Unlike pump-probe experiments, in Z-scan technique the excitation pulse itself plays the role of both the pump and probe. We can recall from the chapter 2 that exciting the nanoparticles with femtosecond laser pulses (pulse duration $\sim 100\text{-}300$ fs) [Hamanaka, Link, Flytzains] results in damping of the surface plasmon oscillation corresponding to a temporal regime in which the incoherent electron-electron scattering processes play a dominant role in the overall relaxation mechanism. For the used pulse duration, a well defined temperature can be assigned to the electrons which are participating in the collisional mechanism which leads to a generation

of “hot-electrons”. While exciting the metal nanoparticles with ultra short pulses with 300 fs pulse duration, one can imagine that the source of nonlinearity is assigned due to the generation of hot electrons via $\Delta \varepsilon'_{he} = 3\pi Re\chi_m^{(3)} |E_{local}|^2$ and $\Delta \varepsilon''_{he} = 3\pi Im\chi_m^{(3)} |E_{local}|^2$ where $\Delta \varepsilon'_{he}$ and $\Delta \varepsilon''_{he}$ are the change in real and imaginary parts of dielectric constant due to the ultrafast heating of conduction electrons and E_{local} represents the local electric field.

As a simple explanation, for dipolar excitation the local electric-field E_{local} differs from the applied field E_i by a field enhancement factor \tilde{f} , which can be represented by $E_{local} = \tilde{f} E_i$. The field enhancement factor \tilde{f} strongly modifies the resonant nonlinear optical process near surface plasmon resonance. Specially for silver nanoparticles having spheroidal shapes, the dipolar plasmon absorption stays spectrally much far away from the interband transition threshold. Accordingly the dispersive behavior of optical nonlinearity (magnitude and sign of the complex valued $\chi_{eff}^{(3)}$) is strongly decided by the nature of dispersion of field factor \tilde{f} . On the other hand far way from the resonance $\tilde{f} = |f| < 1$ the hot electron contribution is unaffected by any other dispersive component.

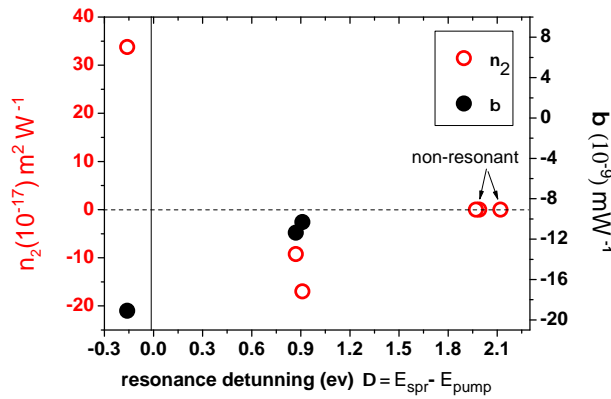


Figure 4.10: The spectral dependence of n_2 and β with respect to the detuning of the SPR peak wavelength from pump wavelength position. The fitted value of β_{\perp} is very small comparison to β_{\parallel} to represent in the graph.

In comparison to the current scenario, for sample LSPR_450 the pump wavelengths stay much far away from the spectral location of both the plasmon resonance (irrespective of the type of experimental configuration) and the interband transition threshold; and thus the sign of the hot-electron contribution is not mixed with any dispersive component which results in an positive nonlinearity. As shown in figure 4.10, by controlling the shape anisotropy to a desired degree, the light interaction can

be tuned to near resonant regime; where the hot electron contribution is influenced by the resonance behavior due the longitudinal plasmon band.

4.4 Nonlinear optical properties in near resonant excitation regime: Local-field effect driven optical nonlinearity

As described in the previous section, in the vicinity of the plasmon resonance, the field enhancement plays a major role in overall nonlinear optical process. The real part of the field factor \tilde{f} shows an anomalous dispersion at the spectral regime of resonance along with a strong enhancement to the imaginary part (chapter 2, section 2.3.3). For a fixed excitation wavelength, the nonlinear process can be pushed to any interaction regime by tuning the shape-factors L of the nanoparticle.

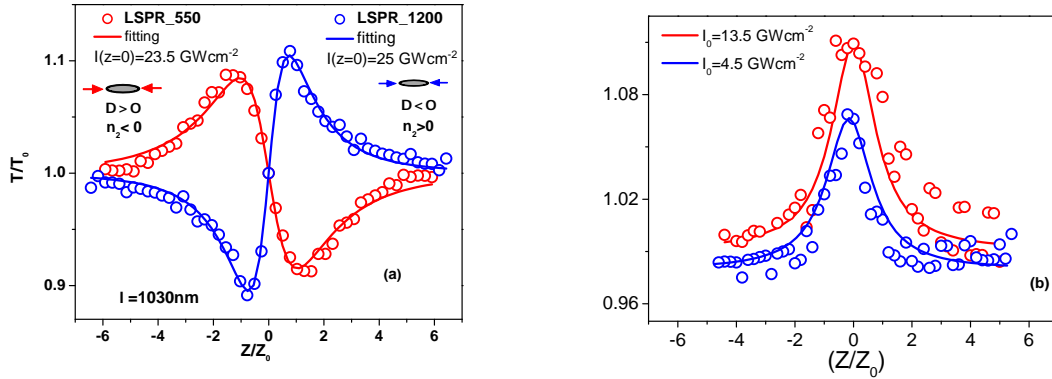


Figure 4.11: Figure a & b represent the closed aperture and open aperture Z-scan curves measured in the \parallel configuration of samples LSPR_1200 and LSPR_550 (exciting at the blue and red side of the Plasmon). Open circles represent experimental points and continuous lines corresponds to theoretical fit.

For instance in our studies we have selected four samples, having different shape factor for the prolate ellipsoidal nanoparticles. From the Mie calculations the shape factor(chapter 2) along the respective semi axis of the nanoparticle are given by $(L_j, L_k)_{i=1,2,4} = (0.481, 0.038), (0.429, 0.142), (0.376, 0.249)$ (described in the Appendix); where L_j and L_k denotes the shape factor for semi-minor and semi-major axis respectively and (here we assume same L values for the sample named LSPR_550) the index i denotes the type of sample (LSPR_1200, 550, 450). For

sample LSPR_1200, small L (large anisotropy) value assumes the band position of the longitudinal plasmon at the infrared spectral regime i.e. at 1200 nm. In the \parallel configuration for either of the pump wavelengths, the excitation falls in the blue side of the plasmon band ($\Delta < 0$). For 1030 nm pump wavelength, the excitation falls very close to the plasmon resonance and correspondingly a positive nonlinear refraction is observed at the closed aperture scan. Figure 4.11 shows the comparison of Z-scan signal measured between the sample LSPR_1200 and LSPR_550 under 1030 nm excitation.

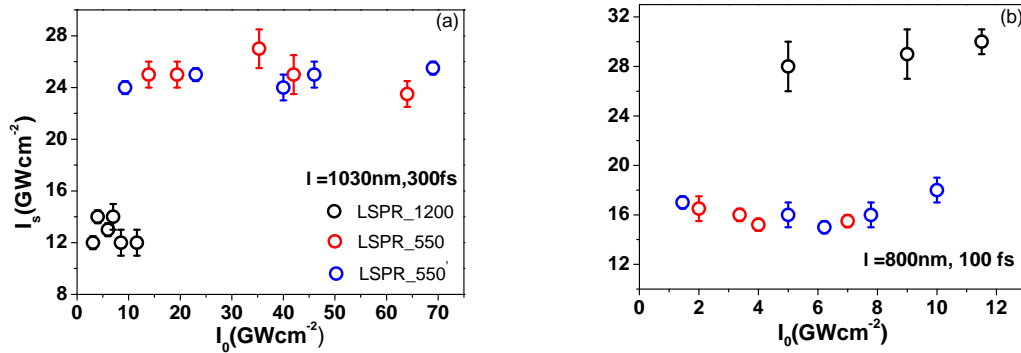


Figure 4.12: The Figure represents the values obtained in saturation intensity I_s at different excitation intensities for sample 1200, LSPR_550's. Figure (a) represents for 1030 nm excitation and (b) that for 800 nm excitation.

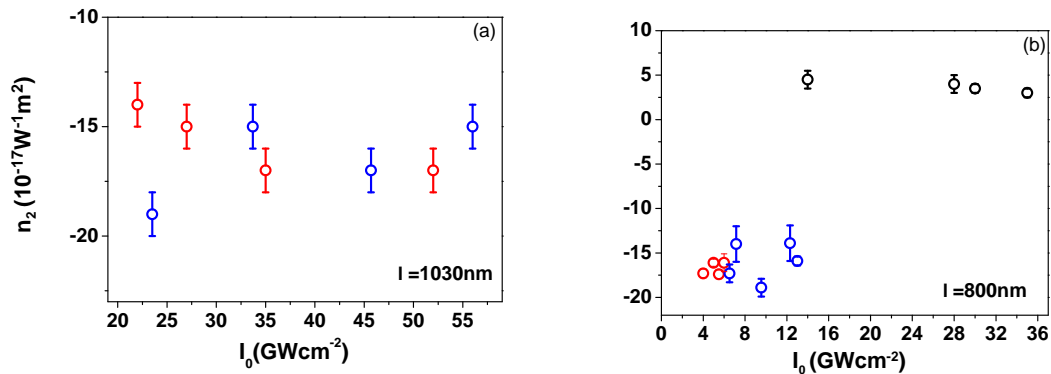


Figure 4.13: The Figure represents values obtained for nonlinear refractive index n_2 at different excitation intensities for sample LSPR_1200, LSPR_550. Figure (a) represents for 1030 nm excitation and (b) that for 800 nm excitation.

In the \parallel configuration while switching from blue(LSPR_1200) to the red side of the plasmon (LSPR_550) we could see a sign reversal in nonlinear refraction (from positive nonlinear refraction to negative) with a negative nonlinear absorption (saturable absorption), which is found to be in accordance with the dispersion behavior of $\chi^{(3)}$ of the two-level system; in which $n_2(m^2/W) = \frac{3}{4\varepsilon_0 n_0^2 c} Re \chi^{(3)}$ and $\beta_{II}(m/W) = \frac{3\omega}{2\varepsilon_0 n_0^2 c^2} Im \chi^{(3)}$ [12].

In the \parallel configuration, the saturation intensity I_s acts as a good parameter for calculating the dispersive nature of two-level model system. As shown in figure 4.12, the saturation intensity calculated for samples (LSPR_1200, LSPR_550's) are found to follow the spectral dependence as given in equation 4.5. The variation of n_2 (figure 4.13 (a) and (b)) with intensity shows a linear behavior within a 20% compound error which concludes a dominant $\chi^{(3)}$ mechanism. In order to analyse the dispersive nature of n_2 and β in the \parallel configuration, we have made use of the shape anisotropy of the nanoparticles. For the calculation, the spectral gap is defined to be $\hbar \Delta = \hbar\omega_{Lspr} - \hbar\omega_{excit}$.

As described in chapter 2 in the resonant interaction regime, the nonlinear processes arising from the saturation of two-level model can be represented as

$$\overline{\chi(\omega; E)} = \frac{\chi^{(1)}(-\omega; \omega)}{1 + I_\omega/I_s(\Delta)}$$

Where $\chi^{(1)}(-\omega; \omega)$ corresponds to the linear susceptibility due to the single photon absorption process represented by

$$\chi^{(1)}(-\omega; \omega) = \frac{-w_0 N e^2}{\varepsilon_0 \hbar (\Delta - i/T_2)} |r_{ab \cdot e}|^2 \propto \frac{1}{(\Delta - i/T_2)}.$$

As we discussed in the previous section, while exciting with 100 fs laser pulses, the collisional mechanism of the conduction electron gas results in heating of electron gas system which are participating in the plasmon oscillation. Hence it leads to the washing out of plasmon oscillation which is otherwise known as bleaching or saturation of the LSPR band. In general the saturation intensity I_s acts as a good physical parameter to describe the strength of the saturable absorption mechanism. We could see from figure 4.12 that the saturation intensity $I_s(\Delta)$ is found to follow the spectral dependence governed by equation 4.5.

For a fixed excitation pump wavelength, the strength of the nonlinearity is decided by the shape anisotropy of the nanoparticles. For highly anisotropic nanoparticles, under infrared laser pulse excitation, the light interaction falls in the near resonant

regime. For instance under 1030 nm excitation, for highly stretched nanocomposite system LSPR_1200, the excitation falls near to the plasmon resonance. Which says that the spectral gap is found to increase with the decrease in the degree of structural anisotropy of the nanoparticles. Thus we could conclude that for a fixed excitation wavelength by controlling the degree of shape anisotropy of the nanoparticles the excitation regime can be spectrally shifted to either the blue or red side of the plasmon (Figure 4.11(a)). Thus one can study the dispersive nature of the optical nonlinearity by making use of the shape factor L of the nanoparticles.

As the light interaction falls in the near resonant regime, even a weak field is sufficient to perturb the material system strongly to make the effect easily detectable. Following this point we could notice from figure 4.12 that in the \parallel configuration, under 1030 nm excitation, the excitation intensities used for the sample LSPR_1200 are restricted to a range of intensities below 20 GWcm^{-2} . On other hand a spectral gap $\Delta(L)$ is developed for samples with considerably less degree of anisotropy (for instance LSPR_550's), accordingly intensities in the range of $10 \leq I_0 \leq 70 \text{ GWcm}^{-2}$ has been used to excite the nanocomposite system.

Each sample is characterized by a particular saturation intensity I_s which is found to be an invariable quantity in the used range of intensity regime. Hence to calculate the dispersive behavior in the \parallel configuration, we have carefully chosen a particular characteristic value for the ratio $\frac{I_{pump}}{I_s}$ such that I_{pump} remains in the proven range of I_s being constant for each sample. The corresponding ratio is $\left(\frac{I_{pump}}{I_s}\right) = 0.35$. Using this constant ratio we calculated the real and imaginary parts of field corrected susceptibility $\Delta \chi(\omega, E)$ using the two level as described in chapter 2 (section: 2.2.1). The field corrected susceptibility of the medium in the nonlinear regime is defined as the difference between the susceptibilities in the presence and absence of strong laser field as

$$\Delta \chi(\omega; E) = \chi(\omega; E) \Big|_{\left(\frac{I_{pump}}{I_s}\right)=constant} - \chi(\omega; E = 0)$$

The comparison between the theory and experiment is shown in figure 4.14, a qualitative agreement between the theory and experiment is found in the over all spectral range. The observed resonant enhancement of β together with the dispersive nature of n_2 in the vicinity of the plasmon resonance is in agreement with the characteristic dispersive behavior of two-level model. The discrepancy observed in the nonlinear refraction probably due to the effects of higher order nonlinearities such as $\chi^{(5)}$ which follow a characteristic dispersion with respect to the resonance.

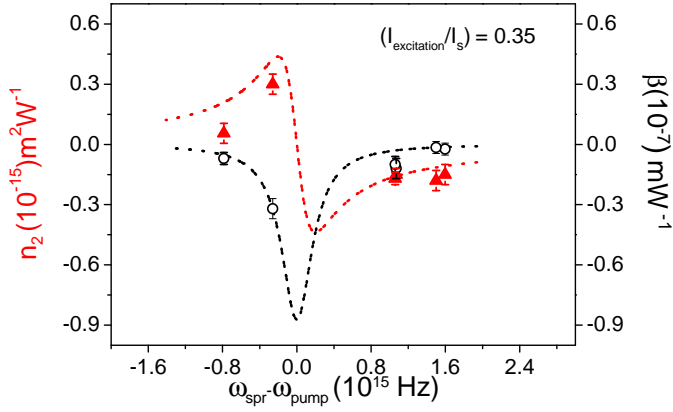


Figure 4.14: Figure represents the spectral dependence of n_2 (non-linear refraction part) and β (nonlinear absorption) of the samples with respect to the detuning of SPR peak wavelength from pump wavelength position in the \parallel configuration. Solid line represents the theoretical curves for real and imaginary parts of complex nonlinear refractive index which in turn is proportional to corresponding complex nonlinear susceptibilities. Open circles represents the nonlinear coefficients obtained from experiments.

4.5 Intensity dependent nonlinear optical properties

Particle plasmon oscillation is extremely sensitive to ultrashort laser pulses. The excitation of nanoparticles with femtosecond pulses results in the damping of the particle plasmon oscillation; corresponding nonlinear optical process is governed by hot electrons. Hence to understand the photo-physical mechanism of the nanoparticle composite systems we have performed intensity dependent nonlinear transmission measurements. The experimental results are shown in figure 4.15.

4.5.1 Photo-Physics of Sample LSPR_550

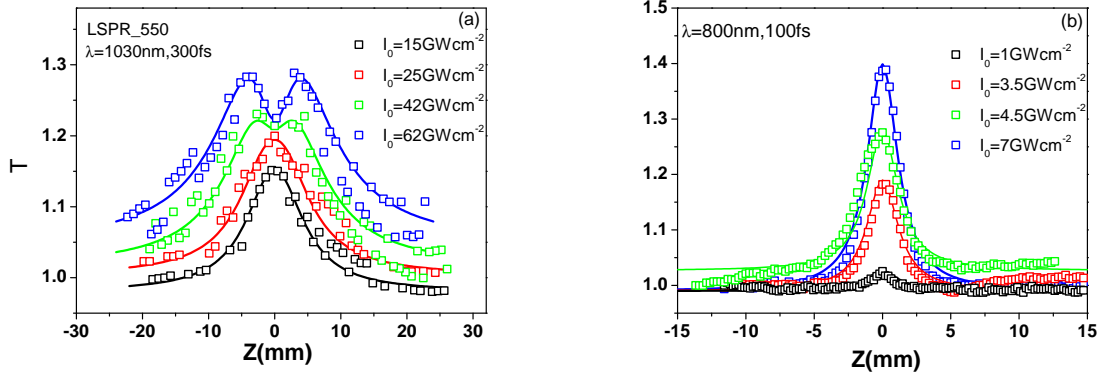


Figure 4.15: The figure represents the intensity dependent open aperture Z-scan measurements performed on LSPR_550 in the \parallel configuration. Figure (a) represents for 1030 nm excitation and (b) for 800 nm excitation.

Figure 4.15 represents the open aperture Z-scan measurements performed on sample LSPR_550 at different excitation intensities, in the \parallel configuration. Under 800 nm excitation, a large absorption cross-section of the nanoparticle assigns a strong saturable absorption. Observed increase in the amplitude of bleaching with increasing excitation intensity assumes a negligible non-resonant nonlinear absorption.

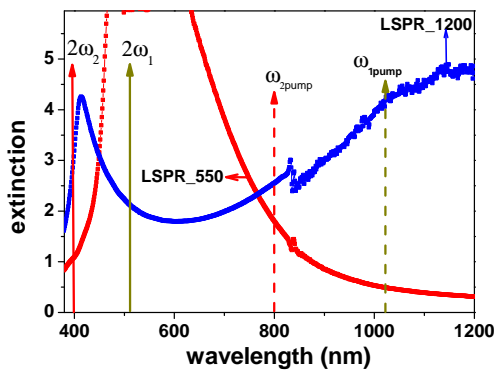


Figure 4.16: The figure represent the polarized linear extinction spectra of sample LSPR_1200 & 550 in the \parallel configuration. The dotted lines represents the position of the pump excitation wavelengths and the solid lines represents the corresponding spectral positions of two-photon absorption.

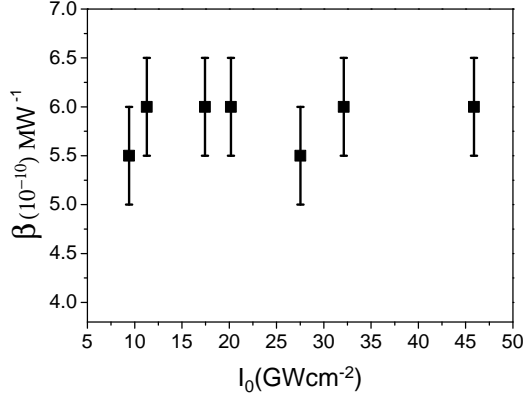


Figure 4.17: The fit values of two-photon absorption coefficient at different intensities for LSPR_550 in the \parallel configuration at 1030 nm excitation.

In order to understand the photo-physical nonlinear mechanism in the \parallel configuration, we have invoked a two level model as described in the previous section through equation (1). In figure 4.15(b), the solid lines represents the theoretical fitting to the experimental data points (represented by open square points). Under 1030 nm excitation, the open aperture scan shows a saturable absorption at low excitation intensity. With increasing intensity (> 8 GWcm $^{-2}$), we could see a two symmetric humps (increase in transmittance) flanking the valley around the focus (figure 4.15(a): green points); i.e. the presence of two composite nonlinear absorptions with opposite signs. As mentioned previously, the saturable absorption assigns a negative sign for nonlinear absorption and hence the observed decrease in the transmission at higher intensities (> 8 GWcm $^{-2}$) must be counteractive effect due to an additional positive nonlinear absorption. From the linear absorption spectra (figure 4.16) one can learn that a strong linear absorption at 512 nm maximizes the two photon transition probability. Taking this point into account we have defined an effective nonlinear absorption as sum of saturable absorption and two photon absorption both originating from the same LSPR as $\beta_{eff} = \left(\frac{\alpha_0}{(1+(I/I_s))} + \beta \right)$ where β is the two-photon absorption coefficient. The theoretical fitting to the experimental data shows a quite good agreement. The value of β is found to be 6×10^{-10} m/W, and in the investigated intensity regime no further saturation in the two photon coefficient is observed (figure 4.17).

Its clearly seen from the figure 4.15(a) that the Z-scan technique is capable of resolving intensity dependent saturable and two-photon absorption spatially. In other words as the sample is far away from the focus negligible nonlinear absorption occurs

as it moves towards the focus the saturable absorption starts dominating, resulting in bleaching of ground state plasmon and at the focus the peak intensity experienced by the sample is high enough that the two photon absorption starts dominating at the focus. Similar phenomena have been reported [56] where octanethiol capped gold clusters showed a saturable absorption and a free carrier absorption under picosecond laser excitation condition.

4.5.2 Photo-Physics of Sample LSPR_1200

Under 1030 nm excitation, with increasing excitation intensity, an increase in the amplitude of the bleaching signal is observed. The very large absorption cross-section at 1030 nm implies the pre-dominant role of dielectric field enhancement in the over all mechanism. The saturation intensity is found to be constant for excitation intensity $I_0 < 40 \text{ GWcm}^{-2}$ (figure 4.18(a)) which indicates the presence of pure saturable absorption mechanism. The fitted value of saturation intensity is $I_s = 12 \text{ GWcm}^{-2}$ and the corresponding linear absorption coefficient is $\alpha_0 = 3.8 \mu\text{m}^{-1}$.

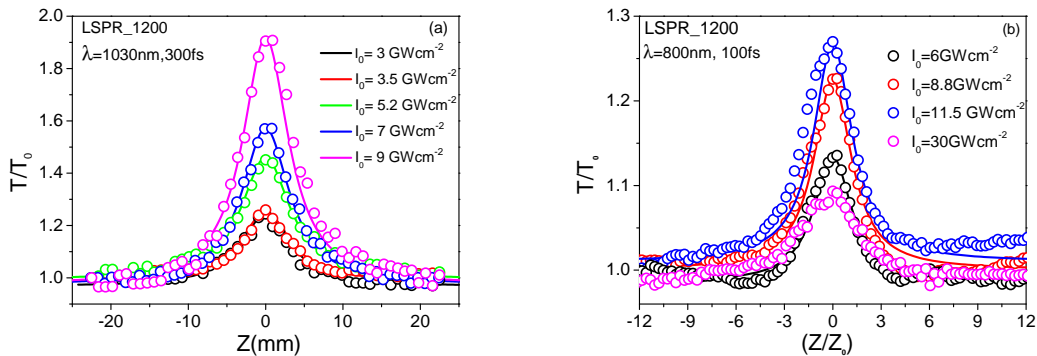


Figure 4.18: The figure represents the intensity dependent open aperture Z-Scan measurements performed on LSPR_1200 in the ||configuration. Figure (a) represents for 1030 nm excitation and (b) for 800 nm excitation

Under 800 nm excitation, an increase in bleaching signal is observed for excitation intensity $I_0 < 20 \text{ GWcm}^{-2}$, on the other hand a sharp drop is observed at 20 GWcm^{-2} intensity implies the presence of a strong (or an additional) optical limiting mechanism. From the figure 4.15, it can be seen that the presence of quadrupolar absorption band peaked at 400 nm. Hence at higher intensities it increases the probability of non-resonant nonlinear absorption i.e, two-photon absorption process

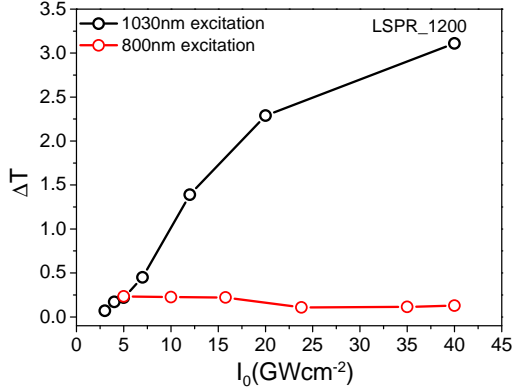


Figure 4.19: Figure shows the variation of transmission change ΔT measured for LSPR_1200 with respect to excitation intensities. The black dots denotes for 1030 nm excitation and red dots for 800 nm excitation

with 800 nm photons. The fitted values of I_s , $\beta_{1,qu}$ (two-photon absorption due to quadrupolar band at \parallel configuration) are found be 30 GWcm^{-2} and $10 \times 10^{-10} \text{ m/W}$ respectively and corresponding α_0 is $2 \mu\text{m}^{-1}$.

Figure 4.19 shows the change in transmission $\Delta T = (T_{(z=0)} - T_{z=\pm z_{max}})$ calculated for two-excitation wavelengths; which implies that for 800 nm excitation, the change in transmission at higher intensities appears rather small which indicates the competition between the bleaching due to the ground state absorption cross-section and two-photon absorption. Speaking in context of local electric field driven nonlinear effects the large absorption cross-section at 1030 nm excitation causes a strong bleaching and hence there is negligible probability for non-resonant processes. By spectrally moving far away from the resonance reduces the bleaching contribution which promotes the non-resonant effect such as two-photon absorption.

$\lambda (nm)$		$\alpha_0(\mu m^{-1})$	$I_s (GW cm^{-2})$	$\beta_u(mW^{-1})\times 10^{-9}$
800nm	LSPR_1200	2.0	30	-6.67
	LSPR_550	1.8	15.5	-11.6
	LSPR1_550	1.6	16	-10
	LSPR_450	0.14	-	0.0289
1030nm	LSPR_1200	3.8	12	-31.6
	LSPR_550	0.59	25	-2.36
	LSPR1_550	0.4	26	-1.53
	LSPR_450	0.11	-	0

$\lambda (nm)$		$n_{2 } (m^2W^{-1})\times 10^{-17}$	$\chi_r^{(3)}(esu)\times 10^{-14}$	$\chi_i^{(3)}(esu)\times 10^{-13}$
800nm	LSPR_1200	4.5	1.3976	-1.3176
	LSPR_550	-15	-4.659	-2.294
	LSPR_550	-17	-5.279	-1.977
	LSPR_450	0.6	0.202	0.006
1030nm	LSPR_1200	26	10.547	-10.507
	LSPR_550	-15	-6.085	-0.7845
	LSPR1_550	-18	-7.302	-0.5087
	LSPR_450	0.72	0.28	0

Table 4.1: The fitted values of nonlinear coefficients for the samples in the \parallel configuration

The table represents the the linear and nonlinear parameters of the samples in \parallel configuration.

4.6 Conclusions

In conclusion, our studies on the nonlinear optical properties of mechanically stretched nanoparticles proved the impact of geometrical anisotropy in the nonlinear optical properties. Anisotropy in the geometrical structure of the nanoparticle allows to investigate the optical nonlinearities in the resonant and non resonant interaction regimes. Choosing the laser polarization with respect to the stretched direction of the nanoparticles allows the selective excitation of the long axis and short axis plasmon respectively. A sign reversal in nonlinearity is observed while switching from \parallel (resonant interaction regime) to the \perp (non-resonant) configuration. In the \perp configuration the contribution from transverse plasmon band falls in the off-resonant regime and the observed positive nonlinear refraction is attributed to the instantaneous nature of the optical nonlinearity. Hence anisotropy in the geometrical structure of the nano-particles pre-dominantly contributes to the nonlinear properties of the nanoparticle system.

The saturation of the longitudinal plasmon band is analyzed on the basis of a two level model. The dispersive nature of the real and imaginary parts of the complex nonlinear refractive indices are compared with the field corrected susceptibility. In the temporal regime of excitation it is the hot electron contribution which plays a major role in the optical non-linearity. The effective nonlinearity measured in the Z-scan configuration is largely influenced by the local field enhancement in the \parallel configuration . The experiments performed at higher intensities on either sample LSPR_550 show simultaneous saturable absorption and two photon absorption originating from the same longitudinal plasmon band, on the other hand for LSPR_1200 it is the two-photon absorption from the quadrupolar band playing the pre-dominant role. In particular in the course of the experiments we found that metal nanoparticles belong to the group of materials where saturable and two-photon absorption happens at same pump wavelength at different excitation intensities. Hence a media exhibiting both saturable absorption and reverse saturable absorption like (two-photon absorption) features at same pump wavelength can be realized for the efficient optical limiting applications as well as the implementation of applications like efficient laser pulse narrowing as well.

Chapter 5

Spectral dependence of the third-order optical nonlinearity of nanocomposites

5.1 Introduction

The optical properties of nanocomposite materials are suitably controlled by tuning the material parameters of the composite systems. For mechanically stretched nanocomposites, the polarization dependent optical properties permit the switching of light interaction from the resonant to the non-resonant regime. Accordingly a sign reversal in nonlinearity is seen on flipping the light interaction regime. In addition to that, the amplitude and the phase of the optical nonlinearity is found to be strongly influenced by the shape anisotropy of the nanoparticle.

In this regard, the aim of the present chapter is to investigate the correlation between the material parameters and nonlinear optical properties of the nanocomposites. The composite systems selected for the nonlinear measurements are found to possess a Maxwell-Garnett type of geometric structure. The nonlinear measurements performed at the near resonant interaction regime show a precise correlation between the optical nonlinearity to the constituent elements of the composite system.

5.2 Experimental Results

Glasses containing ellipsoidal nanoparticles prepared via laser irradiation technique has been used for the nonlinear measurements. The details of the sample preparation method together with its structural properties are described in chapter 3 (section: 3.1.3). The laser irradiation technique is a powerful method to tailor the

material properties of the nanocomposite systems. The samples which are prepared by irradiating the area containing spherical nanoparticles line by line introduces a microscopic inhomogeneity. Accordingly the Z-scan signal measured from the respective area is strongly influenced by the scattering due to the surface inhomogeneity. As described in chapter 3, an alternative solution is to go for Intensity scan (I-scan) technique; in which the sample is fixed in a single Z-position and the output transmission is measured for various input intensities.

The cross-sectional area of each irradiated section of the sample is found be $(2 \times 2) \text{ mm}^2$ which is fixed rigidly in a XY-translational stage at a single Z-position ($Z = -3.5 Z_0$) along the beam propagation direction. The beam radius at the local position of the sample is measured to be $130 \mu\text{m}$ which ensures a full coverage of the entire beam area upon traversing through the selected sample areas. The experimental parameters used for the I-scan technique are an excitation beam of wavelength 515 nm with a pulse duration 300 fs and a repetition rate 1 kHz. Prior to collecting the data, the system is calibrated to ensure the linearity between all the three detectors over the entire range of available energy. We have selected ten sample areas for nonlinear transmission measurements, which are designated as A1 to A10. The spectral location of the excitation pump wavelength with respect to the plasmon peak position of the silver nanocomposite is shown in figure 5.1.

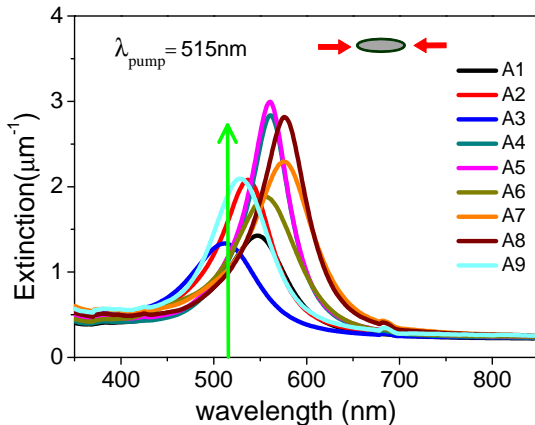


Figure 5.1: The polarized extinction spectra of the nanocomposites measured from different irradiated areas within the sample. The spectra measured from each area possess specific morphological property.

For the nonlinear measurements, the sample is oriented in such way that the long axis of the ellipsoid is in parallel to the laser polarization direction (\parallel configuration

as described in chapter 3) hence the contribution from longitudinal plasmon (LSPR) plays a major role in the over all nonlinear process. We could see from figure 5.1 that for area A3, the pump wavelength falls exactly in resonance with the LSPR absorption band. For the better view the polarized extinction spectra recorded from few sample area with respect to the excitation pump wavelength is shown in figure 5.4. The figure 5.2 shows the open aperture I-scan measurement performed on each sample area. In the used excitation regime, the nonlinear absorption was overwhelming the nonlinear refraction contribution and hence could not be resolved under 515 nm excitation.

We could see from the experimental results that, there are two branches in the nonlinear transmission curves i.e. a set of curve (lower branch) with smaller slope value and another set with large slope value (higher branch). The experimental behavior of the system can be explained by carefully modelling the measured nonlinear transmission spectra.

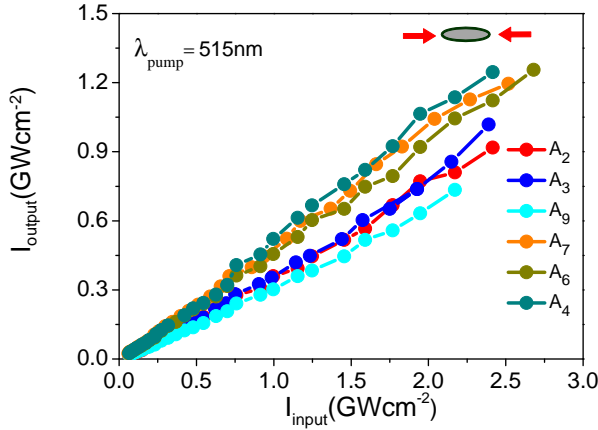


Figure 5.2: The Intensity scan data measured for different irradiated areas performed in the || configuration

5.3 Modelling of Open aperture I-scan

As described in the previous chapter, the ultra short laser pulse excitation of nanoparticles near the plasmon resonance results in the damping of particle plasmon oscillation. Correspondingly a two-level approximation can be used to explain the open aperture I-scan results. The change in input intensity upon traversing through a material medium of thickness z' is represented as

$$\frac{dI}{dz'} = \frac{-\alpha_0 I}{(1 + I/I_s)} \quad (5.1)$$

where α_0 is the linear absorption coefficient and I_s is the saturation intensity of the material medium. If $I_s > I$ the above equation can be approximated as power series expansion of input intensity

$$\frac{dI}{dz'} = -\alpha_0 I + \frac{\alpha_0}{I_s} I^2 - \frac{\alpha_0}{I_s^2} I^3 + \dots = -\left(\alpha_0 + \beta I + \gamma I^2 + \dots\right) I \quad (5.2)$$

Here we prefer to designate $\beta = \left(\frac{-\alpha_0}{I_s}\right)$ and $\gamma = \left(\frac{\alpha_0}{I_s^2}\right)$ thus we can see that the expansion series diverges with increasing excitation intensity.

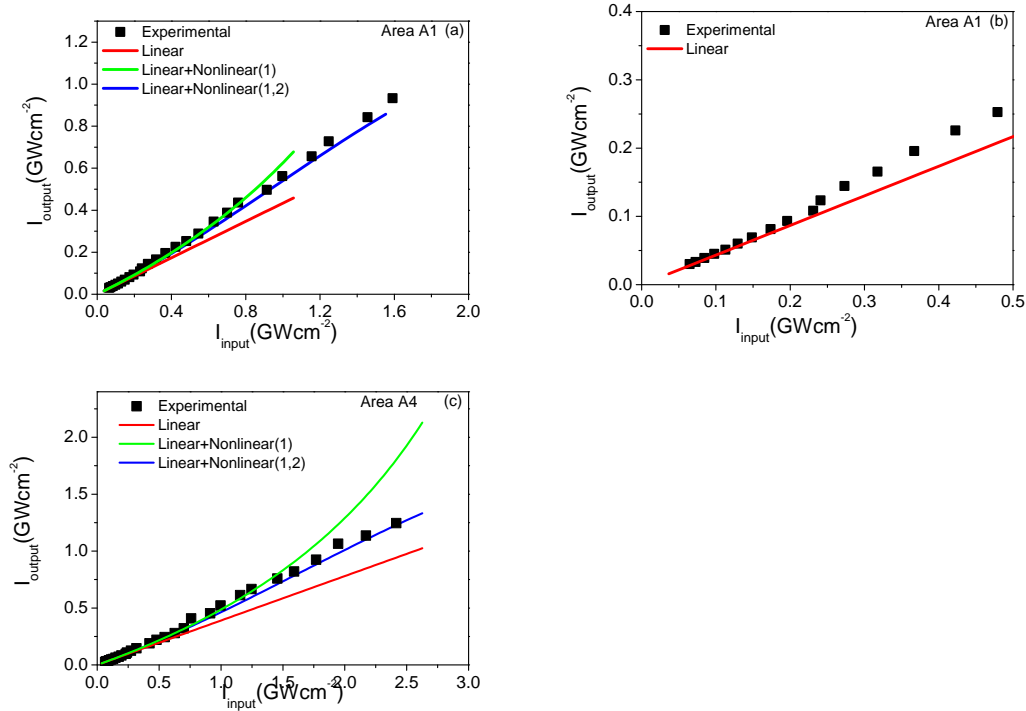


Figure 5.3: The figure represents the comparison between the experimental and theoretical fitting for area A1 (figure.(a)) and area A4 (figure.(c)) respectively. The red line represents the contribution from linear absorption, green and blue line corresponds to the first and second order nonlinear contributions.

The comparison between the theoretical fitting and the experiment data points are shown in the figure (5.3 (a) & (c)). In the figures, the term ‘‘Linear’’ represents the contribution due to the linear absorption α_0 . The terms corresponding to Nonlinear (1) and Nonlinear (1,2) indicates the successive nonlinear contribution which

are given by, $\text{Nonlinear}(1) = \beta I$ and $\text{Nonlinear}(1,2) = (\beta I + \gamma I^2)$ respectively. For excitation intensity $I > 100 \text{ MWcm}^{-2}$, a significant deviation is observed between the experimental measurements and simulated curve (red line) where the calculation includes only the contribution from linear absorption. With increasing input intensity the deviation increases monotonously which concludes the presence of higher order nonlinear process.

First we will discuss the measurements made on the sample area A1. We could see from the figure 5.3 (a & b) that at negligibly small input intensity ($I \leq 9 \text{ MWcm}^{-2}$) the total absorption of the medium is dominated by single photon absorption. However with increasing input intensity a slight increase in transmission is observed. In order to reproduce the experimental results we have added the successive terms in the expansion series. For instance by including the second term i.e. $\text{Nonlinear}(1)$ to the previous one, we could explain the measured output transmission for excitation intensities $I < 0.8 \text{ GWcm}^{-2}$. At higher intensities it necessitates the presence of higher order nonlinear terms for achieving the better fitting.

On the other hand for area A4, including only the first two terms in the calculation could reproduce the nonlinear transmission for excitation intensity $I < 1.5 \text{ GWcm}^{-2}$. The possible explanation is that while selecting from area A1 to area A4, the spectral gap (between the plasmon peak position and the pump excitation wavelength) $\Delta = \hbar(\omega_{\text{spri}} - \omega_{\text{pump}})$ changes from -0.14 eV to -0.2 eV and the corresponding variations in the strength of the dielectric field enhancement boosts the nonlinear process for the sample area A1 as compared to the area A4.

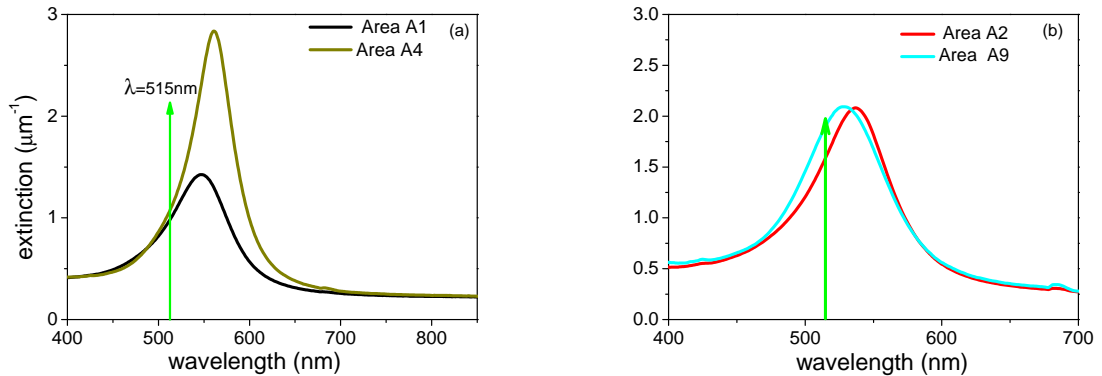


Figure 5.4: The polarized extinction spectra of the area A1 & A4 (figure 5.4(a)), and that of area A2 and A9 (figure 5.4(b)). The green arrow represents the spectral position of pump wavelength with respect to plasmon band absorption.

To study the correlation between the nonlinearity measured from different sample

areas, we have chosen those areas having nearly identical linear absorption spectra (i.e. plasmon bands having similar band width and signal intensity) as shown in figure 5.4(b). For area A9 the excitation wavelength 515 nm falls exactly in resonance with the plasmon band while it is spectrally separated for the plasmon band measured from area A2. The fitted value of β is found to be -8×10^{-8} m/W, -6.67×10^{-8} m/W for area A9 and A2 respectively. It can be seen that the threshold intensity for higher order nonlinear process is smaller for area A9 than that of area A2.

As described in chapter 3, by tuning the laser irradiation parameters (intensity & number of pulses), one could shift the position of the plasmon band to wide spectral range. However the material properties can fluctuate from one area to another. Looking at the figure 5.1, the variations observed in the band intensity within the spectral window of 60 nm could be resulting from corresponding variations (fluctuations) in the material parameters such as the filling factor, effective layer thickness of glass containing metal nanoparticles, refractive index of the host matrix and finally the size and shape distribution of the nanoparticles.

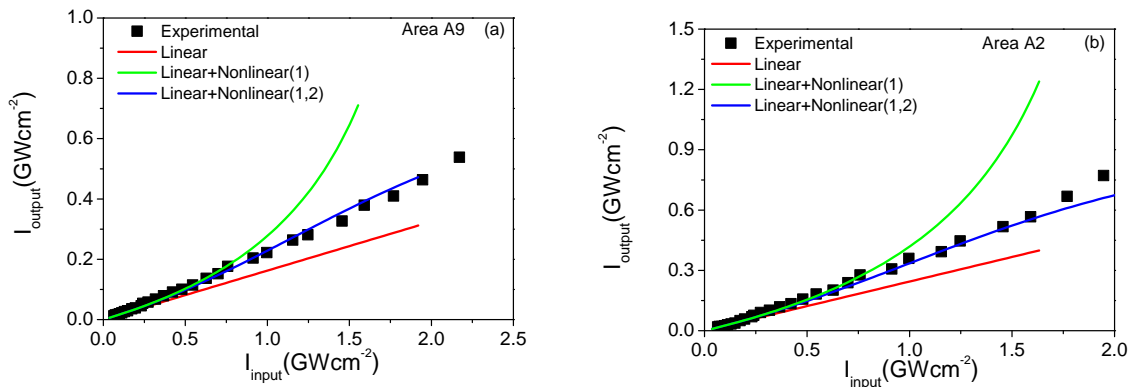


Figure 5.5: The figure represents the comparison between the experimental and theoretical fitting for area A9 (figure 5.5(a)) and area A2 (figure 5.5(b)) respectively. The red line represents the contribution due to linear absorption, green and blue line corresponding to the first and second order nonlinear contributions.

5.4 Maxwell Garnett samples

In quasi-static limit ($\lambda \gg 2R$) the Maxwell-Garnett theory acts as a nice tool to understand the correlation between the material parameters and the optical properties (both linear and nonlinear) of the composite systems. The finite optical features of the dipolar absorption band (plasmon band intensity & width) resulting from the low filling factor and smaller size of the nanoparticles in the laser irradiated

nanocomposite, makes them a suitable candidate in the family of Maxwell Garnett (MG) systems. One can extend the MG theory for the nanocomposite containing the spherical nanoparticles into ellipsoidal shapes through a suitable effective dielectric function ε_{eff} .

The functional dependence of material parameters on effective dielectric function ε_{eff} can be represented as $\varepsilon_{eff}(p, L, \varepsilon_m(\omega), \varepsilon_d)$, where p , L , ε_m & ε_d signifies the volume filling factor, the nanoparticle shape, dielectric function of the metal nanoparticles and the dielectric host matrix respectively. In high dilution limit the effective dielectric function of composite material can be expressed as [5, 41, 64]

$$\varepsilon_{eff}^z \approx \varepsilon_d + p \frac{\varepsilon_d(\varepsilon_m - \varepsilon_d)}{L_z \varepsilon_m + (1 - L_z) \varepsilon_d} \quad (5.3)$$

where the index z denotes the orientational direction of semi-major axis and corresponding linear absorption coefficient is $\alpha(\omega) = \frac{2\omega}{c} [Im(\varepsilon_{eff})]^{1/2}$. For the calculation, we have used Johnson and Christy [34] values for the metallic dielectric function ε_m with a size correction applied to the imaginary part; given by $\varepsilon_{m2} = \frac{\omega_p^2}{\omega^3} (\Gamma_{bulk} + \Gamma(R_{eff}))$. The term $\Gamma(R_{eff}) = A \frac{V_F}{R_{eff}}$ denotes the surface scattering mechanism where A denotes the parameter describing the interface interactions, V_F the Fermi velocity of the electrons and R_{eff} the effective radius of the long axis of the nanoparticle which is found to be 15 nm. By taking the shape factor L of the nanoparticle as a variable parameter, we could successfully match the plasmon peak position with the measured absorption spectra. The filling factor p for each area is then calculated from linear absorption coefficient α_0 by using the resonance condition i.e. $\alpha_0(\omega_{Lspr}) = \frac{\omega}{n_0 c} p \frac{\varepsilon_d \varepsilon_{m2}}{(L \varepsilon_{m2})^2}$.

The comparison between the calculated and the measured spectra is shown above in the figure 5.6(a) & (b). In the fitting routine the peak position of the plasmon band (which is a measure of shape anisotropy of nanoparticles) is taken as an important parameter. The observed broadening of the spectra can be attributed to the size and shape distribution of the nanoparticles. A quite good agreement is observed between the simulated and the measured extinction spectra. From figure 5.7(a) we could infer that there is a fluctuation in filling factor p from one area to another. A similar fluctuation is observed in the plasmon band intensity $\alpha_{\lambda_{spr}}$ which underlines the influence of material parameters on the linear optical properties of the nanocomposite systems.

CHAPTER 5. SPECTRAL DEPENDENCE OF THE THIRD-ORDER OPTICAL NONLINEARITY

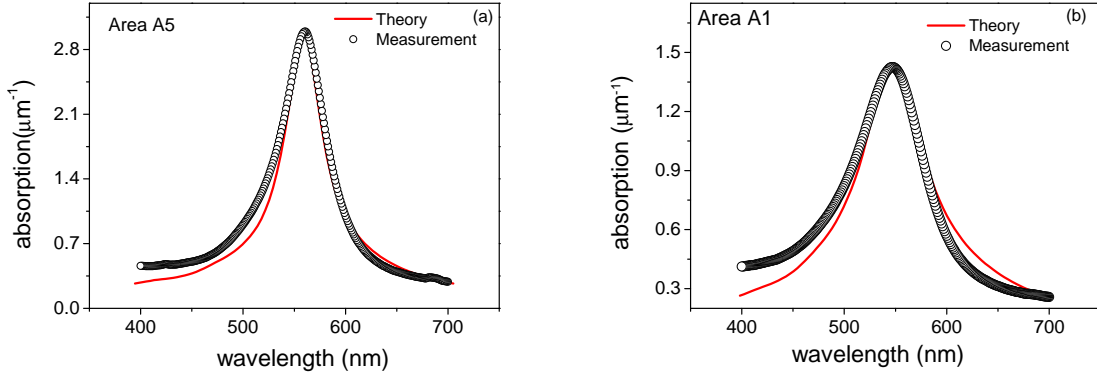


Figure 5.6: The figure represents the comparison between the extinction spectra calculated using the Maxwell-Garnett theory and the measured spectra. figure 5.6(a): area A5; figure 5.6(b): Area A1.

Figure 5.7 shows the variation of β (corresponding to the saturable absorption) with the spectral gap $\hbar \Delta (= \hbar (\omega_{spr} - \omega))$. Looking at figure 5.7(a) we could see that the calculated nonlinear coefficients are largely influenced by the material parameters of the composite system. The observed fluctuation in the nonlinear coefficients is closely connected to the variation in the material parameters within each areas. An enhancement in nonlinear coefficients is observed near surface plasmon resonance.

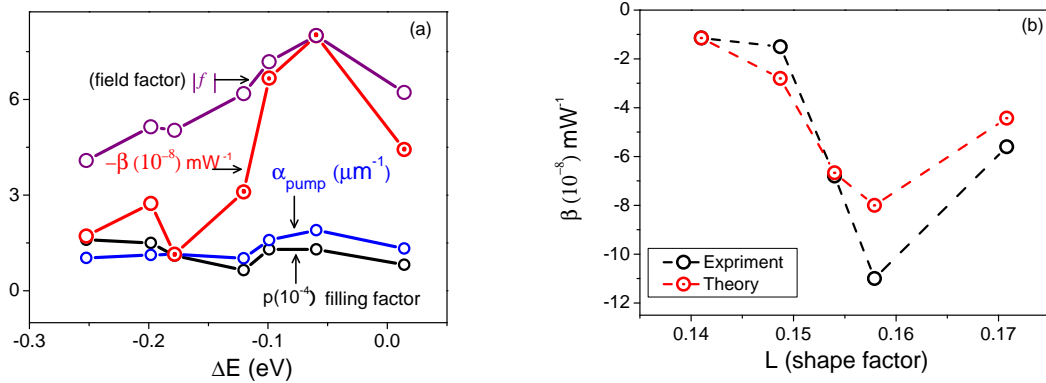


Figure 5.7: Figure (a): The variation of nonlinear absorption coefficient (β), filling factor (p) and linear absorption coefficient ($\alpha_{\lambda_{pump}}$) at excitation wavelength with respect to the spectral gap ($\hbar \Delta = \hbar (\omega_{spr} - \omega_{pump})$). Figure (b): The variation of β with the shape of the nanoparticles. The circled dot in two graphs corresponds to the experimental β values measured from same area.

By extending the Maxwell-Garnett theory for the ellipsoidal nanocomposites to the nonlinear optical regime[5, 42, 22, 23, 24], we calculated the effective nonlinear

susceptibility $\chi_{eff}^{(3)}$ for the nanocomposites (details of the calculations are available in the Appendix) for each sample area having a characteristic shape factor L_i and filling factor p_i . In the quasi-static regime $\chi_{eff}^{(3)}$ can be expressed as

$$\chi_{eff}^{(3)} = p |f_i|^2 (f_i)^2 \chi_m^{(3)}$$

where f_i is the field enhancement factor and $\chi_m^{(3)}$ is the intrinsic nonlinearity of nanoparticles. A quantitative agreement is observed between the theoretical and experimental β values (Figure 5.7(b)). The formula connecting β to χ_{eff} is given by

$$\beta = \frac{4\pi}{\lambda} Im \left\{ \frac{12\pi}{n Re(n)} \chi_{eff}^{(m)} \right\} \quad (5.4)$$

We could see an enhancement in the value of $\chi^{(3)}$ for the shape factor 0.1575 corresponding to the area A9 where pump wavelength falls nearly in resonance with the plasmon absorption. The observed fluctuation in β is likely to be resulting from the variation in f which is a wavelength dependent factor together with the variation in the filling factor of the nanoparticles from one area to another. Hence we can conclude that the observed trend in the optical nonlinearity nearly maps the material properties of the nanocomposite systems together with the spectrally dependent field enhancement factor.

In general, the ultrashort laser pulse excitation of nanoparticles at the surface plasmon resonance results in a damping of plasmon oscillation corresponding to a broadening of plasmon resonance. The heating of the conduction electrons (T_e —*electronic temperature*) results in an increment in the damping constant $\Gamma(T_e)$ which gives a large imaginary part ε_{m2} of the nanoparticle dielectric function. As discussed in the reference [69, 58] at plasmon frequency, the resonance condition is given by $[(L\varepsilon_{m1}) + (1 - L)\varepsilon_d]^2 \approx 0$, hence any increase in the value ε_{m2} results in a decrease of plasmon absorption. For the current scenario, under ultrashort laser pulse irradiation an increased damping in the plasmon oscillation due to single photon absorption increases the value of the ε_{m2} resulting in a bleaching of the plasmon band intensity. Such decreased absorption is interpreted as saturable absorption and the corresponding absorption of the nanocomposite is defined as $\alpha(I) = \alpha_0 + \left(-\frac{\alpha_0}{I_s}\right) I$.

5.5 Conclusion

Area	$p(10^{-4})$	$\alpha_0(10^6)\mu m^{-1}$	$-\beta(10^{-8})\left(\frac{m}{W}\right)$	$ f $	$\Delta E(\text{eV})$	$I_s\left(\frac{GW}{cm^2}\right)$
A1	0.88	1.018	3	6.182	-0.1204	2.5
A2	1.82	1.5911	6.67	7.186	-0.0990	2.3
A3	0.92	1.329	4.43	6.22	0.0142	1.8
A4	0.74	1.123	2.740	5.144	-0.1982	4.1
A6	1.55	1.147	1.147	5.034	-0.1783	10
A7	2.2	1.0298	1.716	4.087	-0.2523	6
A9	1.8	1.9016	8	8.008	-0.0595	2

Table 5.1: The fitted values of nonlinear coefficients for the samples in the \parallel configuration

We have studied the nonlinear optical properties of metal nanocomposite glass in a I-Scan setup utilizing femtosecond laser pulses. The nonlinear measurements performed at the resonant interaction regime (\parallel -configuration) is analyzed and compared with the Maxwell Garnett systems. An enhancement in optical nonlinearity is observed near surface plasmon resonance. The Maxwell Garnett approximation could give physical insights into the correlation between the material parameters and the nonlinear optical properties of the nanocomposite system. The observed variations in the nonlinear absorption is closely connected with the fluctuations in the filling factors and the spectral dependence of the field enhancement factor $|f(w)|$ of the nanoparticle systems.

The above results shows that by suitably tailoring the material properties of the nanocomposite systems their optical nonlinearity can be tuned for desired material applications.

Chapter 6

Directional selective optical limiting in bi-layer glass-metal nanocomposites

6.1 Introduction

Non-reciprocal systems are of fundamental interest in optical physics because of their unidirectional nature. The one-way electromagnetic transmission is analogous to an optical diode effect. In general a diode is an essential element in most electronic circuits, enabling the current flow in the forward direction and blocking it in the backward direction. Similarly an optical analogue of electronic diode can transmit light in one direction and block it in reverse direction (and the device can be called as “optical diode”). One well-known example is an optical isolator based on linear polarizers and a Faraday rotator.

In recent years several new concepts of optical diodes have been proposed and practically demonstrated. Magnetic effects on helical periodic medium, absorbing multi-layer systems and asymmetric nonlinear distributed Bragg grating have been theoretically found to show the optical diode like behavior [16]. On the other hand it has been experimentally demonstrated that a system of cascaded nonlinear meta-atoms [13], an anisotropic nematic layer sandwiched between two polymer cholesteric liquid crystals with different periodicity of helix [30], asymmetric nonlinear absorption in layered materials [55] and nanocomposite microcavities made of gold nanoparticles were showing a directionally anisotropic response under linearly polarized light [29].

While the above mentioned successful efforts rely on complex structures, we have theoretically and then experimentally examined an optical-diode like mechanism

in a very simple material structure. The idea is came out from the identification of nonlinear refractive mechanism observed in the non-resonant light interaction regime, where the substrate material is found to play a significant contribution in overall nonlinear mechanism. If the substrate material plays a role in the nonlinear process, then the effective nonlinearity of the samples has to be analysed using the concept of bi-layer (bi-or multi- layered system) model structures. To testify the above mentioned arguments, we have used the following strategy: the geometrical structure of the sample is taken as a thin layer of nonlinear sample placed over a comparatively thick transparent substrate material. The physical scenario can be equally picturised as a thin nonlinear sample layer which is placed in tandem with comparably thick nonlinear refractive lens whose focal length strongly depends on the irradiance of the input laser beam.

In this regard the present chapter will focus on the Gaussian beam propagation through the bi-layer sample structure in the nonlinear optical regime. At first we will theoretically analyse the evolution of Gaussian beam through the bi-layer sample and then we will compare the theoretical predictions with the experimental observation. The experimental measurements are performed mainly on glass containing spherical nanoparticles; finally we cross-checked the experimental behaviour in even simpler sample structure of TiO_2 coated on SiO_2 .

6.2 Theoretical modelling

In general the laser beam propagation through a nonlinear medium can be well described using the nonlinear wave equation as given below

$$\nabla^2 E - \frac{1}{c^2} \frac{\partial^2}{\partial t^2} [(n_0 + \Delta n)^2 E] = 0 \quad (6.1)$$

where E represents the electric field and n_0 the refractive index of the medium under low intensity illumination. The term Δn includes the contribution from the intensity dependent refractive index (also known as Kerr lensing effect) which is given by $\Delta n = n_2 \left(\frac{E^2}{2} \right)$. In the above equation the Laplacian ∇^2 deals with the transverse variation of the intensity profile while propagating through a thick sample and an exact numerical solution to the above equation is a complex task [46, 68].

On the other hand a model based on the nonlinear non-aberrational lens approach can be used to (also known as constant shape approximation) describe the Gaussian

beam propagation through a thick nonlinear medium. The aberrationless approach assumes that the laser beam maintains its Gaussian profile during its propagation through the medium; i.e. if a spherical wave with a modulated wavefront falls on a layer of thickness L , then the aberrationless approximation assumes that the radial variation of the index of refraction to be parabolic [38, 68, 67]. For a Gaussian beam and cubic nonlinearity such a requirement is satisfied by the following approximation:

$$\Delta n(r) = \Delta n(0) \exp(-2r^2/w^2) \approx \Delta n(0) (1 - 2r^2/w^2) \quad (6.2)$$

where $\Delta n(0)$ is the on-axis index change, w is the local beam radius.

In thin sample approximation, the thickness of the sample L is less than the Rayleigh length Z_0 of the laser beam. This corresponds to an external self-lensing effect, i.e. the thickness of the layer of material is insufficient for the self-focusing of the beam to occur inside the sample. Hence the material layer acts like a nonlinear lens. The focal length of the nonlinear lens depends on the laser beam irradiance.

In general the phase shift introduced on the electric field exiting from a layer of nonlinear sample of thickness L is defined as $e^{i\Delta\phi(r)}$ where the induced phase-shift is given by

$$\Delta \phi_0 = \frac{2\pi}{\lambda} n_2 I_0 L_{eff} \quad (6.3)$$

where I_0 and L_{eff} represent the on axis peak intensity and effective interaction length respectively. On comparing the situation with the linear lensing effect, where the phase of the Gaussian beam exiting from the thin lens is modulated by a phase factor $e^{ik_0 \frac{r^2}{2f}}$ (where f represents the focal length of convex/concave lens); correspondingly one can associate a nonlinear lensing behavior with the sample in the nonlinear optical regime [67, 68, 38]. The self-lensing effect of such sample is described by an intensity dependent focal length given by

$$f_{Kerr} = \frac{aw^2}{4n_2 I_0 L} \quad (6.4)$$

A nonlinear $ABCD$ matrix has been used for dealing the Gaussian beam propagation through a nonlinear medium. For a given Z position, the Gaussian beam propagation through a nonlinear medium is described using the $ABCD$ matrix as follows

$$\begin{pmatrix} A_T & B_T \\ C_T & D_T \end{pmatrix} = \begin{pmatrix} 1 - L/n_0 f_{Kerr} & L/n_0 \\ -1/f_{Kerr} & 1 \end{pmatrix} \quad (6.5)$$

L denotes the thickness of the nonlinear lens which was chosen to be much smaller than both Rayleigh length of the beam and f_{Kerr} .

We will now explain the Gaussian beam propagation through the nonlinear sample step by step. The complex beam parameter at the focal point of the lens, q_f is given by

$$q_f = i \frac{\pi w_0^2}{\lambda}. \quad (6.6)$$

The corresponding q-parameter at the entrance plane of the sample (located at Z) is

$$q_0 = (q_f + Z)n_0.$$

Inside the sample, the connection between the q_i and q_{i+1} parameters of the neighbouring zones are connected using the matrix elements by [40, 51, 68, 79]

$$q_{i+1} = \frac{A_T q_i + B_T}{C_T q_i + D_T},$$

where in general q_i is defined as

$$\frac{1}{q_i} = \frac{1}{R_i(Z)} - \frac{i\lambda}{\pi n_0 w_i^2(Z)}.$$

Here w_i represents the beam irradiance at the entrance plane of the nonlinear sample which is related to q_i through

$$w_i = \left[-Im \left(\frac{1}{q_i} \right) \frac{\pi n_0}{\lambda} \right]^{\frac{-1}{2}}.$$

6.2.1 Gaussian beam propagation through layered structures

The theoretical calculations are performed at the non-resonant excitation regime of the sample. Thus the effects arising from the resonant enhancement will not be considered in the further sections. As shown in figure 6.1, a bi-layer geometrical model with layers having different linear and nonlinear optical properties has been taken into account. The linear and nonlinear refractive indices of the first and second layer are designated as $[n_{01}, n_{21}]$ and $[n_{02}, n_{22}]$ respectively and corresponding absorptive parts by $[\alpha_{01}, \beta_1, \gamma_1]$ and $[\alpha_{02}, \beta_2, \gamma_2]$ where α , β and γ represent the

single, two and three photon absorption coefficients of the two layers respectively. The thickness of the substrate material and sample layer has taken to be of the order of $\sim 500 \otimes L_{sam}$ and $\sim L_{sam}$ respectively; where L_{sam} represents the thickness of thin nonlinear sample layer.

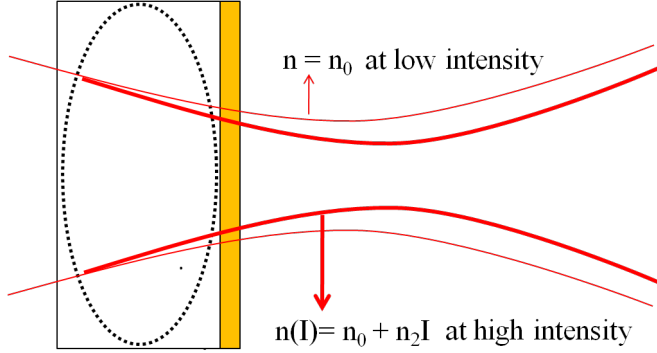


Figure 6.1: The figure represents the schematic of bi-layer sample structure used for the theoretical modelling. The thin yellow colored block represents the thin layer of nonlinear sample whose nonlinearity has to be measured which is placed in tandem with the thick substrate material. At low intensity (thin curved red solid line) the self-lensing effects from the glass substrate can be neglected. At high intensities (thick curved red solid line) the self-lensing effects results in considerable changes in laser beam parameters at the exit plane of the substrate.

At first we calculated the beam waist radius at the exit surface of the substrate which is placed along the beam propagation direction. The calculations are performed by choosing the nonlinear refractive index of the transparent substrate to be $n_{21} = 2 \times 10^{-20} \text{ m}^2/\text{W}$ (measured from the closed aperture scan measurements), the thickness of the substrate and Rayleigh length of the laser beams are selected to be 1 mm and 4 mm respectively. Figure 6.2(a) represents the evolution of beam radius calculated at the exit plane of a lossless substrate material. We could infer from the calculations that the effect of the nonlinear refraction at the substrate material results in a contraction of the beam radius together with a slight shift in the position of focal spot of the laser beam [53]. The change in the beam curvature is related to the phase profile of the beam at the output of the nonlinear sample and thus to the intensity dependent refractive index of the material. As shown in figure 6.2(a), at higher excitation intensities, the degree of contraction in beam radius is found to increase due to enhanced nonlinear refractive effects.

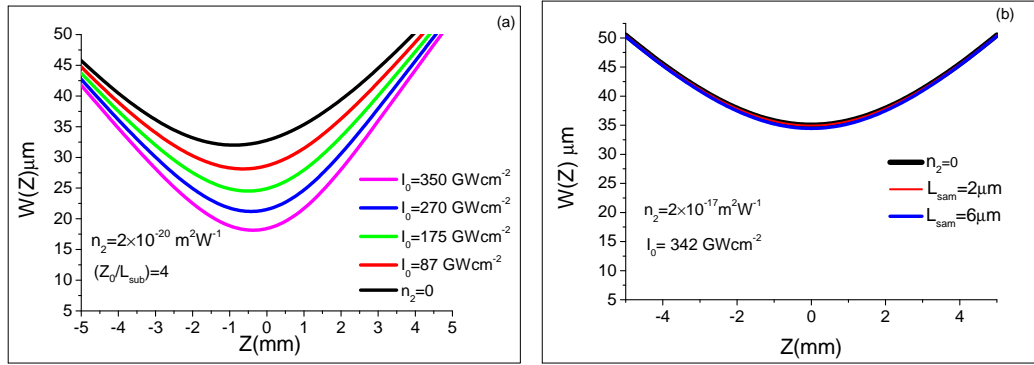


Figure 6.2: The figure (a) represents the beam radius calculated at the exit of substrate material along the beam propagation direction. The black solid line represent the beam propagation through a transparent substrate material in the linear optical regime, different colours in the figure represents the beam radius calculated at the nonlinear optical regime. Figure (b) represents the beam radius calculated at the exit plane of thin nonlinear sample layer.

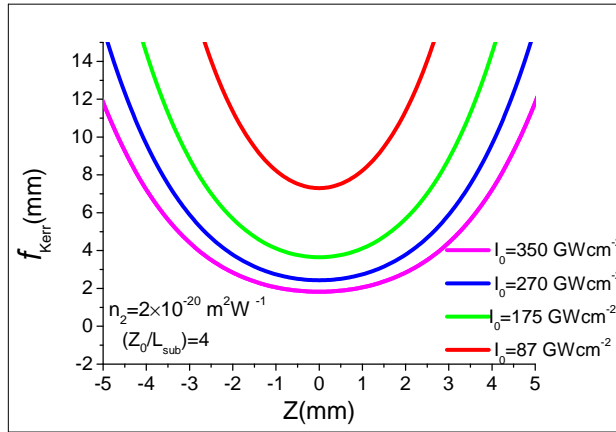


Figure 6.3: The intensity dependent focal length (arising from the nonlinear refractive effects of substrate material) calculated along the beam propagation direction for different excitation intensities.

Correspondingly, the nonlinearity modifies the Rayleigh length of the laser beam to a considerable extent, which is given by $\frac{\pi W_{new}^2}{\lambda}$ where W_{new} represents the contracted beam radius due to nonlinear refraction. Figure 6.3 represents the corresponding intensity dependent focal length of the substrate material calculated for each laser excitation parameters used for the calculation of beam radius at exit plane of the substrate (figure 6.2(a)). The simulated results are shown in figure 6.3. Hence with increasing excitation intensity, we could observe a shrinking in the focal length of the nonlinear lens; analogous to a tight focusing situation arising from the nonlinear refractive effects from 1-mm-thick substrate plate. As expected an increase in

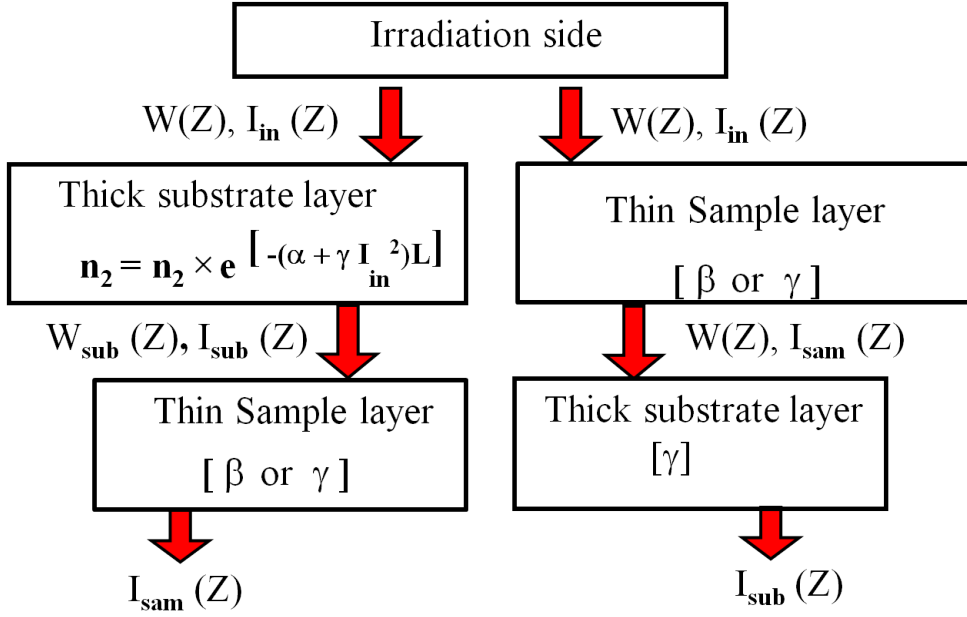


Figure 6.4: Schematic of the beam-sample configuration used for the calculation of open aperture transmission curve while irradiating from either side of the bi-layer sample. $I_{in}(Z)$ is input intensity to the bi-layer sample irrespective of the direction of propagation. $I_{sam}(Z)$ denotes the output intensity at the exit plane of the sample while irradiating from the glass substrate. $I_{sub}(Z)$ indicates the intensity at the exit plane of substrate while irradiating from the thin nonlinear sample side of the bi-layer structure

excitation intensity shifts the focal point closer to the substrate material.

As a second step, using the above described procedure we calculated the beam radius at the exit plane of thin sample layer. The thickness and the nonlinear refractive index of the thin sample layer has been taken to be $2 \mu m$ and $2 \times 10^{-17} m^2/W$ respectively. The theoretical calculations (figure 6.2(b)) show a negligible change in the laser beam parameters while exiting from the thin sample layer of the material. Thus the overall phase change induced in the laser beam upon interaction with the Kerr medium is strongly depends on the interaction length within the material system. Equivalent physical senario is picturised in figure 6.1.

In the nonlinear optical regime, we adopted two configurations for the calculation of the transmission through a bi-layer medium as depicted in figure 6.4. While irradiating from the substrate side of the sample, the beam radius $W_{sub}(Z)$ at the exit plane of the glass substrate is calculated by taking into account of both nonlinear refractive and absorptive effects. In the next step we re-calculated the intensity at the exit plane of the substarte material by taking into account the nonlinear absorption loss as $I_1(Z) = \left(\frac{2P}{\pi W_{sub}^2}\right) e^{-(\alpha + \gamma I^2)L}$ where the absorption losses are taken care

in the nonlinear-refractive index of the substrate material as $n_2(I) = n_2 e^{-(\alpha+\gamma I^2)L}$. The re-calculated intensity at the exit plane of the substrate material is used as the input for the thin nonlinear sample which can exhibit either two or three photon absorption process or both.

The intensity evolution through the sample layer is evaluated using the propagational differential equation given by

$$\frac{dI}{dz'} = -(\alpha I + \beta I^2 + \gamma I^3 + \dots)$$

where z' describes the propagation depth within the thin sample layer. As discussed in the previous section while irradiating from the thin sample side of the bi-layer structure, the change in beam width parameter within the sample side has not been taken into account. Thus the output intensity at the exit plane of the sample layer is decided by the strength of the nonlinear absorption arising either from two or three photon absorption process. Corresponding output intensity at the exit plane of the sample layer is used as the input for the substrate layer.

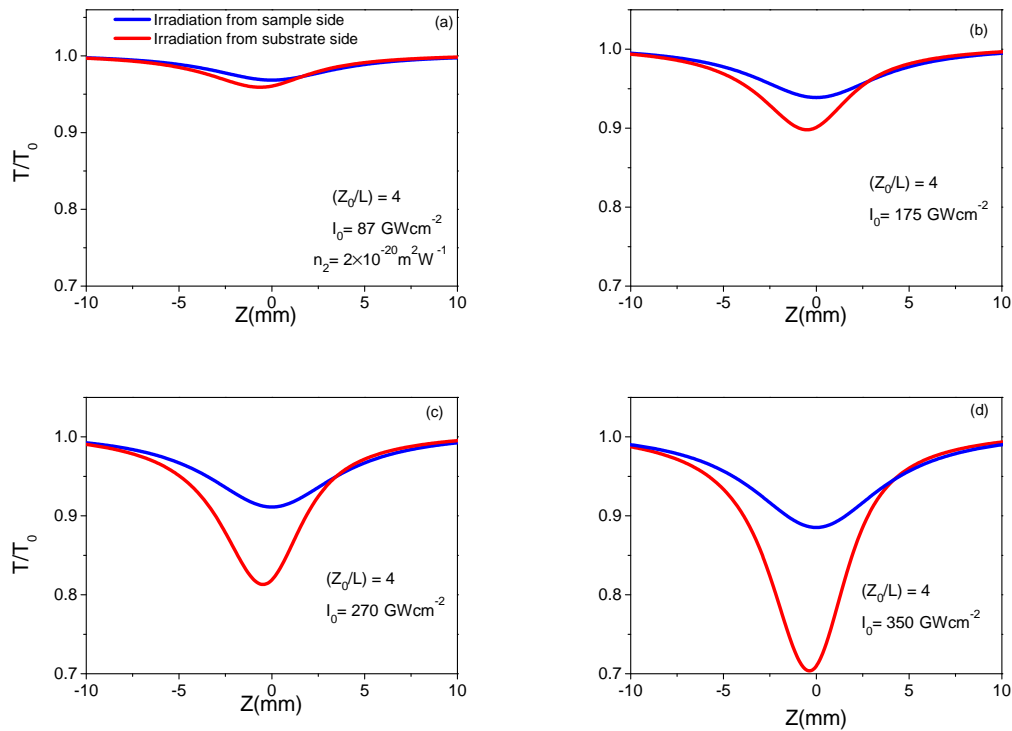


Figure 6.5: The simulated open aperture Z-scan curves for various excitation intensities at a fixed Rayleigh length of the laser beam.

6.2.2 Propagation through bi-layer structure (Lossless substrate)

Figure 6.5 (a to d) represent the open aperture transmission curves calculated for a bi-layer sample structure for different excitation intensities. Calculations are performed for a lossless substrate material. From the simulated open aperture Z-scan signals, we could infer a directionality in the nonlinear transmission while irradiating from either side of the sample. The observed anisotropic transmission is explained by a reduced transmission (an enhanced two photon absorption) while irradiating from the substrate side of the sample, as compared to the irradiation from the thin nonlinear sample side of the material system. Unitary contrast observed in the nonlinear transmission reveals an optical diode like behavior. In general an ideal optical diode is described as a device with full light transmission along one direction known as forward bias but with a reduced transmission in the opposite direction called the reverse bias without an aid of an external agent. The theoretical calculation yields a similar observation, i.e. a directional behavior in the nonlinear transmission resulting from the asymmetry in the geometrical structure bi-layer medium. The magnitude of the asymmetry is decided by the thickness of the substrate material in comparison to the entire sample thickness (thickness of substrate+sample).

The strong self-focusing effect from the thick glass substrate is found to play a key role in the observed anisotropic transmission. Laser beam passing first through the substrate side of the sample results in a contraction of beam radius (corresponding to an increased beam intensity) resulting in an enhanced nonlinear absorption while passing through the thin nonlinear sample side. While for a laser beam passing in the opposite direction, the magnitude of the nonlinear absorption depends only upon the material parameters (β , L_{sam}) of thin nonlinear sample layer.

Hence we could assign a forward bias configuration $T_{forward}$ for the irradiation from the thin nonlinear sample side and a reverse bias configuration while irradiating in the opposite direction $T_{reverse}$. Here $T_{forward}$ and $T_{reverse}$ represent the transmission in the respective irradiation direction. We defined the magnitude of anisotropic transmission as $\Delta T = T_{forward} - T_{reverse}$. The ΔT is found to reduce with the decrease in excitation intensity. In other words the strength of self lensing effect from the substrate material is found to decrease (similar to a loose focussing situation) at lower excitation intensity which replicates in the magnitude of ΔT . Thus in general the magnitude of ΔT is strongly decided by the focal length of the nonlinear lens (which in effect strongly depends upon n_2 , I_0 and L_{eff}) which can be represented by

the following functional form $\Delta T \propto \frac{1}{f_{Kerr}}$.

6.2.3 From the limit of thin sample to thick sample approximation

We will now discuss the dependence of Rayleigh length of the laser beam on the magnitude of the anisotropic transmission. The calculations are performed for a set of Rayleigh length values at a single excitation wavelength. For each value of Z_0 (which is decided by the focal length of the external bi-convex lens), the peak intensity $I_0 = \left(\frac{2P_{peak}}{\pi W_0^2}\right)$ is kept at a constant value of 350 GWcm^{-2} . A lossless substrate material (\sim thickness 1 mm) with nonlinear refractive index $n_2 = 2 \times 10^{-20} \text{ m}^2/\text{W}$ has been taken into consideration. We assigned a two-photon absorption ($\beta = 2 \times 10^{-11} \text{ m/W}$) coefficient for the thin sample layer (thickness $\sim 2 \mu\text{m}$). Figure 6.6 represents the open aperture curve calculated for four different values of Rayleigh range (a-d). It is obvious that the magnitude of anisotropic transmission ΔT increases with the decrease of Z_0 .

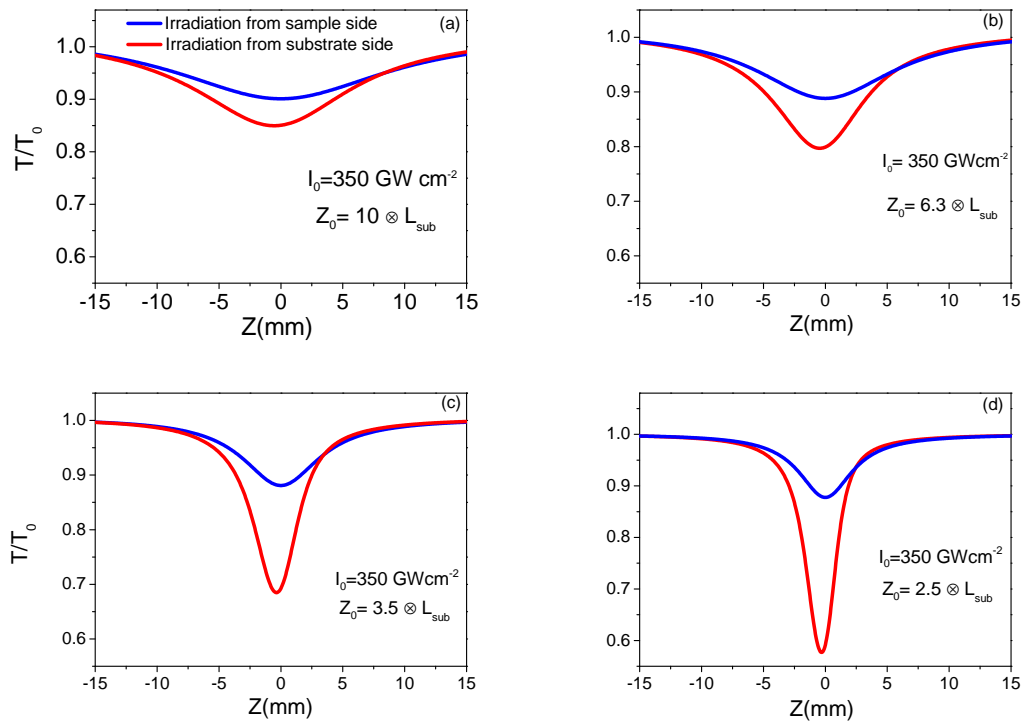


Figure 6.6: The simulated open aperture Z-scan curves calculated for lossless substrate material for various Rayleigh length of the laser beam at a fixed excitation intensity

In general, the decrease in the Rayleigh length of the focussed Gaussian beam results in a tight focussing situation (in the absence of the nonlinear medium). As we learned from the section 6.2.1, upon introducing the nonlinear refractive medium along the beam propagation path, with the substrate layer facing the laser beam can result in further reduction in the Rayleigh length. As a result the collimation point will shift more towards the thin nonlinear sample side. The shifting of focal point is more prominent for laser beam with reduced Rayleigh length. Similarly the thin nonlinear sample layer is more sensitive to the contracted beam radius due to the additional focussing from the substrate plate. Hence one can conclude that the magnitude of the anisotropic transmission increases with the decrease in the Rayleigh length of the focussed laser beam.

The thin sample approximation is strongly valid with the increase in ratio of (Z_0/L) . Equivalently an external self-lensing effect ($|f_{Kerr}| \gg L$) is realised where the transmission takes an isotropic nature irrespective of the direction of illumination. Thus for fixed Rayleigh length and excitation intensity the magnitude of the anisotropic transmission can be controlled by varying the thickness of the substrate material.

6.2.4 Propagation through bi-layer structure (Lossy substrate)

We have extended the calculations by including the absorptive losses from the substrate material. For the calculation we have assigned a three photon absorption process for the substrate layer and its numerical value is selected to be $\gamma = 10 \times 10^{-30}$ m³/W. The comparison of ΔT between the lossless and lossy substrate is shown in figure 6.7. A noticeable effect is the decrease in ΔT for a lossy substrate material. The inclusion of the nonlinear absorption loss for the substrate side reduce the magnitude of the anisotropic transmission. Including the attenuation in the substrate side of the sample reduces the strength of the nonlinear refractive effects which leads to slightly less changes in the laser beam parameters as compared to the lossless substrate material.

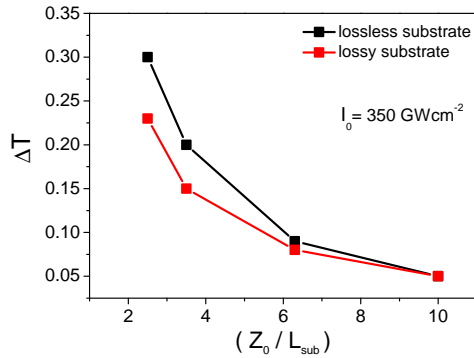


Figure 6.7: Figure represents the comparison of anisotropic transmission between the lossless and lossy substrate material

6.3 Theoretical conclusions

An enhanced nonlinear absorption is observed while irradiating from the substrate side of the sample as compared to the irradiation from the thin nonlinear layer side. The strength of the diode action is found to be strongly dependent on the phase shift induced on the laser beam exiting from the substrate side. For a fixed excitation wavelength, the phase shift induced on the laser beam strongly depends upon the interaction length L_{eff} and the peak intensity I_0 . Hence one can assign a minimum phase shift value $\Delta\phi_{min}$ for the observation of diode action in a bi-layer media. In the course of the theoretical analysis it is found that the magnitude of the directional behavior can be tuned to any desired degree by suitably engineering the geometrical structure (for instance multi-layered structures) and by tailoring the material properties of the nonlinear samples.

To confirm the theoretical predictions we performed experimental measurements on some bi-layer structure such as glass containing silver nanoparticles and TiO_2 coated SiO_2 .

6.4 Sample specification

Glass containing spherical silver nanoparticles are selected for nonlinear measurements. The samples are prepared using Ag^+ - Na^+ ion exchange technique for soda-lime float glass followed by annealing in H_2 reduction atmosphere which results in the formation of spherical silver nanoparticles of 30-40 nm mean diameter (chapter

3, section 3.1.1). The size and distribution of Ag nanoparticles in the depth of the glass sample is studied using scanning electron microscopy (SEM). We paraphrase the geometrical structure of the composite glass as a bi-layer structure consisting of a thin layer of glass containing graded distribution of silver nanoparticles (thickness $\sim 6 \mu\text{m}$) within a thick glass substrate (thickness $\sim 1 \text{ mm}$). For nonlinear characterization, samples with two different concentrations of Ag nanoparticles are used. Samples with highly concentrated Ag nanoparticles in the surface layer is named as ‘heavy doped’ and that with less concentration of particles as ‘light doped’ which were prepared from the heavy doped samples by etching its very immediate surface layer. The linear transmission spectrum (figure 6.8) of the sample shows the SPR absorption band centered at 400 nm which confirms the presence of Ag nanoparticles in the glass matrix.

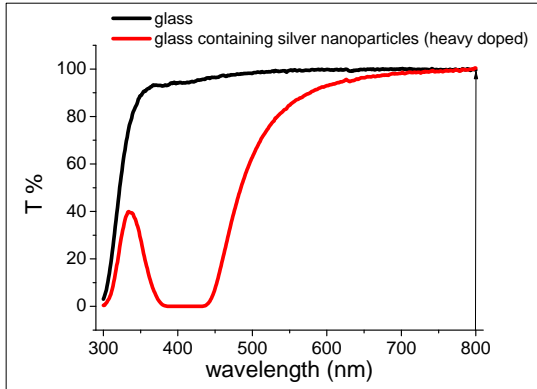


Figure 6.8: The linear transmission spectra measured from pure glass, and glass containing silver nanoparticles

6.5 Experimental results

For the nonlinear measurements we have used 800 nm pump wavelength with a pulse duration 100 fs and repetition rate 1 kHz . The nonlinear transmission measurements were performed using open-aperture Z-scan technique (details are described in chapter 3).

For nonlinear measurements, we have adopted the same strategy as we used for the theoretical calculations. Figure 6.9 shows the experimental configuration used for the nonlinear measurements i.e, the nonlinear transmission measurements are performed by irradiating successively from either side of sample.

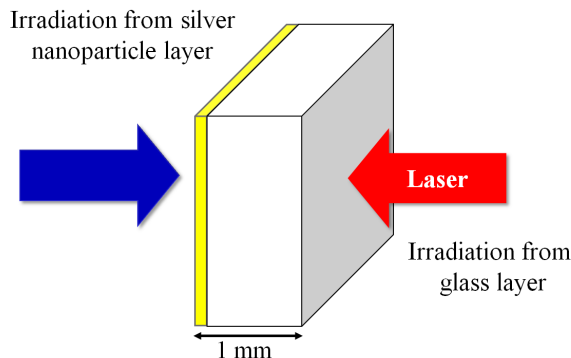


Figure 6.9: Experimental configuration used for nonlinear measurements of bi-layer sample structure.

In figure 6.9, the direction of the blue arrow represents the nonlinear transmission measurements performed with laser beam facing towards the particle side of the sample whereas the red arrow symbolizes the irradiation of the same sample under the same condition from the glass side. In other words while irradiating from the particle side, at first the laser pulse will pass through the particle side and then propagate through the glass side.

Figure.6.10 and 6.11 represent the open aperture Z-scan measurements performed on heavy and light doped samples. The measurements are performed for four different excitation intensities. For each excitation intensity, we separately measured the closed and open aperture signals from a pure glass substrate. A directional selective nonlinear transmission is observed upon irradiating from either side of the sample. The observed directional dependence (figure 6.10(a-d)) is found to be in agreement with the theoretical calculations.

An enhanced optical limiting mechanism is observed upon irradiating the glass side of the sample as compared to the measurements performed from the particle side of the nanocomposite glass. Such a highly directional selective optical limiting mechanism resembles the electrical behavior of diode. The nonlinear measurements performed with irradiation from the particle layer correspond to the forward biasing configuration while irradiation from the glass side corresponds to the reverse bias. The experimental measurements are performed for a fixed Rayleigh length of the beam and it is found that the magnitude of the anisotropic transmission is strongly decided by the input intensity of the laser beam i.e. for intensity below 150 GWcm^{-2} the optical diode action is found to be negligibly small.

6.5. EXPERIMENTAL RESULTS

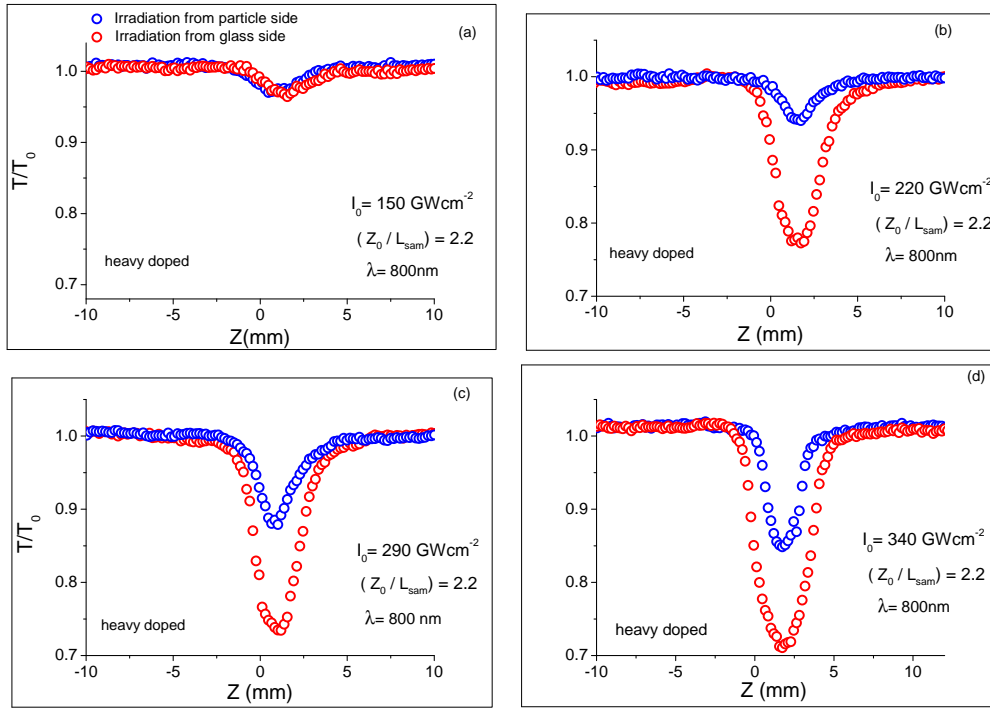


Figure 6.10: The open aperture Z-scan curves measured from the heavy doped nanocomposite glass with varying intensities for $(\frac{Z_0}{L}) = 2.2$.

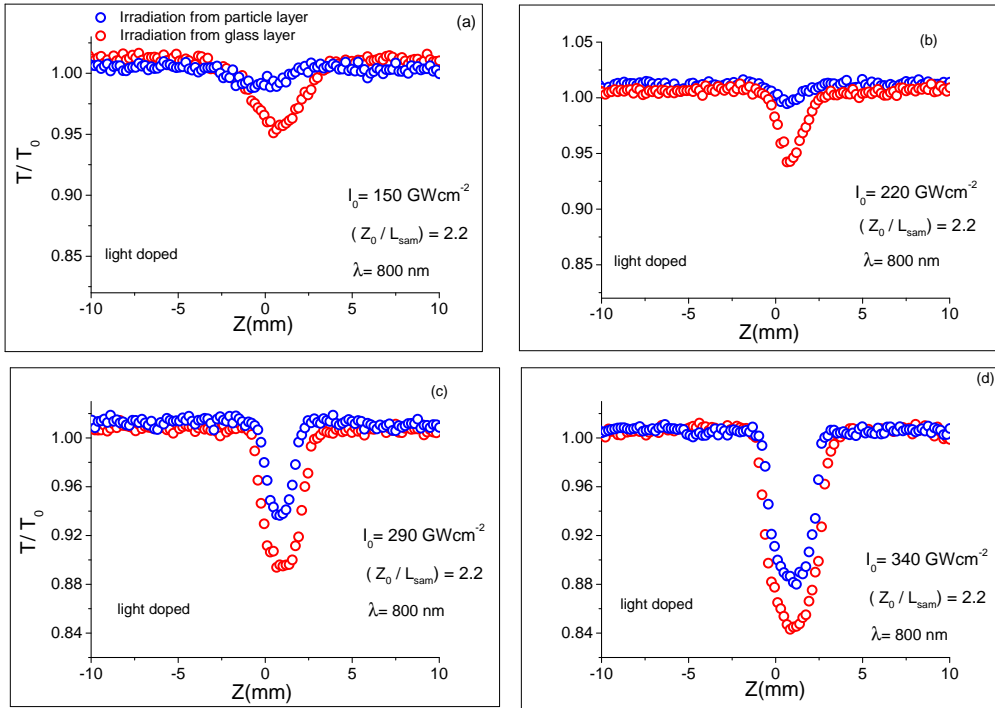


Figure 6.11: The open aperture Z-scan curves measured from the light doped nanocomposite glass with varying intensities for $(\frac{Z_0}{L}) = 2.2$.

For heavy doped samples, for intensity below 150 GWcm^{-2} , the diode behavior is hardly noticeable. The directional dependence is strongly observed for intensities larger than 200 GWcm^{-2} . Figure 6.12 shows the variation in magnitude of anisotropic transmission (ΔT) with the excitation intensities I_0 . For heavy doped sample, the magnitude of ΔT is found to be maximum at an excitation intensity of 220 GWcm^{-2} . After wards ΔT decreases with the increase in excitation intensity I_0 . The observed decrease in the magnitude of ΔT beyond the excitation intensity 220 GWcm^{-2} due to the presence of nonlinear absorption in the substrate side.

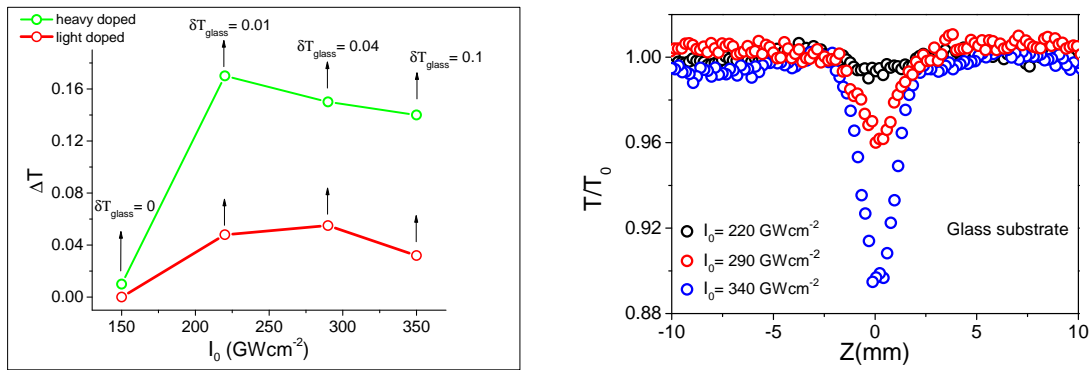


Figure 6.12: Figure represents the comparison of anisotropic transmission between the heavy and light doped sample (left). The open aperture Z-scan signal measured from substrate glass (right).

Figure 6.12(right) shows the nonlinear absorption measurements performed on pure substrate glass. We have defined the strength of the nonlinear absorption from the glass substrate as $\delta T_{\text{glass}} = |T_{Z=0} - T_{Z=\pm Z_{\text{max}}}|$. Upon exciting with 800 nm pump wavelength at the transparency regime of the glass substrate, system can absorb the pump photons through the three photon absorption process. The probability of the multi-photon absorption cross-section is found to depend upon the pump excitation intensity I_0 . At higher intensities ($I_0 > 250 \text{ GWcm}^{-2}$), the nonlinear effects from the glass substrate possess both refractive and absorption parts. In principle, the presence of absorptive events in the glass substrate results in a reduced excitation intensity. While propagating through the glass substrate, the attenuation in the excitation intensity due to the three photon absorption can suppress the nonlinear lensing effects from the glass substrate. As discussed in the theoretical section (section: 6.2.4), once the excitation intensity exceeds the threshold intensity

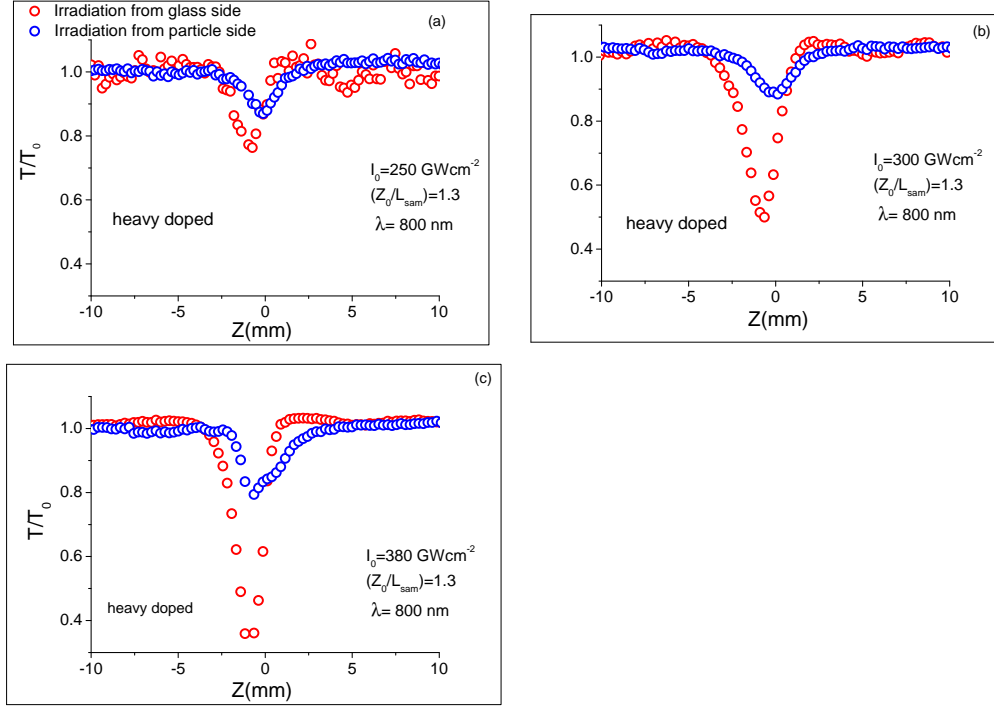


Figure 6.13: The open aperture Z-Scan curves measured from the heavy doped nanocomposite glass with varying intensities for $(\frac{Z_0}{L}) = 1.3$.

for the multi-photon absorption in the substrate side of the sample, the degree of beam contraction decreases with further increase in the excitation intensity. On the other hand for moderate intensities, (just below the threshold intensity for the three photon absorption) irradiating from the glass side of the sample results in an enhanced self-focusing and finally a strong two-photon absorption at the particle side. Irradiating from the particle side results in two photon absorption from the particle layer with negligible self-focusing and much weaker three photon absorption from the glass layer.

Compared to heavy doped samples, a decrease in the magnitude of anisotropic transmission is observed for light doped samples (Figure 6.11). Composites with much thinner particle layer can reduce the strength of the two photon absorption mechanism to a considerable extent. Thus for light doped samples, while irradiating from the particle side, the nonlinear absorption contribution with considerably less number of two-photon absorbers result in much weaker absorption and correspondingly there is considerable amount of intensity available for the pure glass substrate. In effect while irradiating from the two different directions of the light doped sample the magnitude of ΔT reduces to a considerable extent.

Figure 6.13 (a,b and c) represents the open aperture scan measurements performed for short focal length lens with Rayleigh length $Z_0 = 1.3 L_{sam}$. The observed enhanced anisotropic transmission is found to be in agreement with the theoretical predictions i.e. an enhanced anisotropic transmission ΔT resulting in the modification of the Rayleigh length of the laser beam.

As shown in figure 6.11, below certain threshold intensities, ($< 320 \text{ GWcm}^{-2}$) an enhancement in the magnitude of the anisotropic transmission ΔT is observed with the increase in excitation intensity. On the other hand a decrease in ΔT is observed with further increase in excitation intensity. On the contrary, the theoretical calculation (Figure 6.5) predicted a monotonous increase in the anisotropic transmission with the increase in excitation intensity.

The observed reduction in ΔT at higher excitation intensity could be explained by including the higher order nonlinear absorption processes in the substrate glass side. It can be inferred from the linear transmission spectra (Figure 6.8) that the band gap of glass falls in the range of $E_g > 4 \text{ eV}$. Under 800 nm excitation, a three photon absorption mechanism could promote the energetically deep electrons from the valence band to the conduction band. With increasing excitation intensity, the enhanced probability of three photon absorption process might result in an increased density of free electrons in the conduction band. These free-carriers subsequently gain the kinetic energy by the linear absorption from the laser beam. Hence, for alkali-silicate glass, excitation at higher intensities could result in a three-photon absorption and three photon absorption generated free-carrier absorption [18, 32].

Following the above discussion, while irradiating from the substrate side of the sample, the simultaneous occurrence of three photon and three photon induced free carrier absorption could suppress the nonlinear refractive effects in the substrate side. Which reduces the rate of contraction of beam radius due to the nonlinear refraction. On the other hand while irradiating from the particle side, a strong optical limiting mechanism prior to the glass substrate could reduce the input intensity to a considerable extent. The amount of intensity available for the glass substrate may not be sufficient enough to promote the higher order nonlinear absorption process. Hence it might be possible that the occurrence of higher order nonlinear absorption process follows a direction selectivity upon irradiating from either side of the sample.

The experimental measurements (figure 6.10 and 6.11) reveal that the rate of decrease of anisotropic transmission is found to be strongly dependent upon the thickness of the particle containing layer. Following the discussion from the previous

paragraph, for heavy doped samples, a strong limiting mechanism in the particle layer reduces the output intensity to a considerable extent. The reduction in intensity prior to the thick substrate layer, suppresses the additional nonlinear absorption mechanism in the substrate side. Alternatively for light doped samples, much of the intensity is available for the thick glass substrate layer. In short for light doped glass, the transmission takes an isotropic nature at very low excitation intensities, an anisotropic nature at moderate intensities and finally a cross-over to isotropic transmission at higher excitation intensities. On the other hand for the theoretical calculation, the nonlinear absorption is restricted to a pure three photon absorption process for the substrate side. The absorption loss arising from the higher order nonlinear process has not been taken into account. Hence in order to explain the experimental trends, one needs to take care of all nonlinear absorption losses initiated at higher excitation intensities at the substrate side of the sample.

Even though the experimental measurements have unmistakably demonstrated the theoretical predictions, a slight disagreement between the theoretical predictions with experimental measurements can arise due to the complex geometrical structure of the nanocomposite glass. As discussed in chapter 3, section 3.1.1 in which the nanoparticles are distributed gradually within a thin layer of glass substrate. For the Z-scan measurements, while irradiating from either direction, the laser beam may not exactly pass the same area of the of the sample can resulting in slight contradiction in experimental measurements.

6.6 Nonlinear transmission measurements performed on simple bi-layer structures

TiO₂ -SiO₂ thin films

In this context we have cross-checked the behavior of nonlinear transmission in other simple structures such as TiO₂ (of thickness 1 μm) on thick glass SiO₂(thickness 1mm). The experimental results are shown in figure 6.14. The measurements show an anisotropic transmission while irradiating from either side of the sample. i.e. an enhanced optical limiting mechanism upon irradiation from glass side of the sample compared to irradiation from the TiO₂. Compared to the nanocomposite glass structure, the TiO₂- SiO₂ shows a strong contrast in transmission. For instance from figure 6.14(a), for excitation intensity 290 GWcm^{-2} we could see a perfect transmis-

sion while irradiating from the TiO_2 side of the sample. Here we could remember the fact that, while irradiating from the TiO_2 side of the sample, a strong refractive index contrast at the air- TiO_2 interface (corresponding to Fresnel reflection) reduces the input intensity to the TiO_2 side of the sample which indeed reduce the probability of nonlinear absorption mechanism.

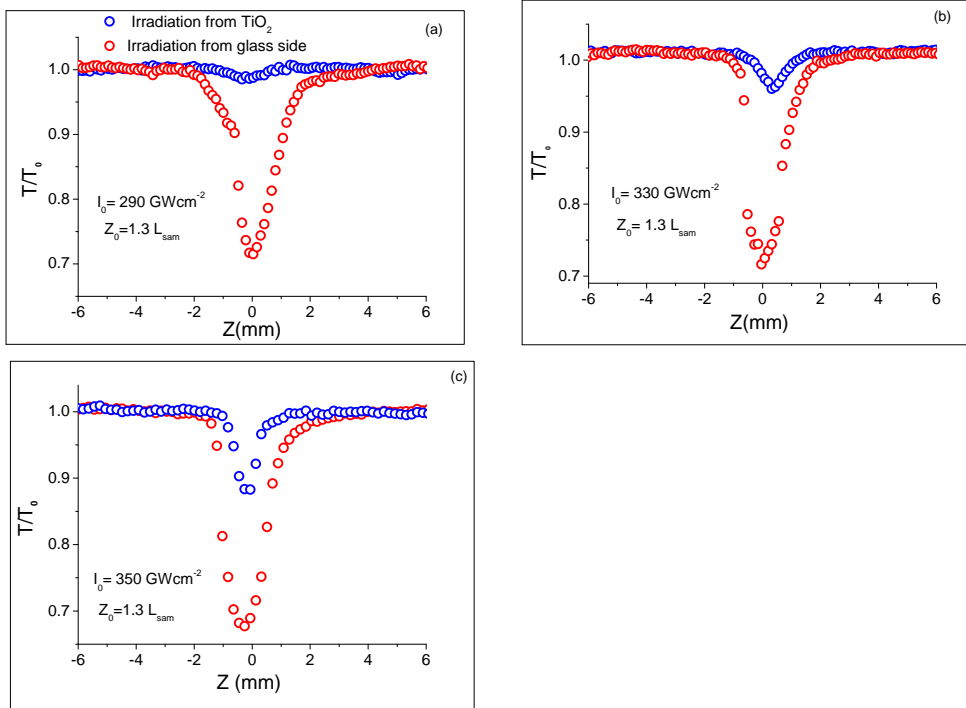


Figure 6.14: The open aperture Z-scan curves measured from the TiO_2 - SiO_2 with varying intensities for $\left(\frac{Z_0}{L_{\text{sam}}}\right) = 1.3$.

6.7 Conclusions and Outlook

The present chapter is focused on the optical diode behavior observed from a bi-layer structure sample structure (a thin sample layer on thick glass substrate). A directional selective nonlinear transmission is seen during the successive irradiation from either side of the bi-layer sample. The observed non-reciprocal transmission is explained by combining nonlinear refractive effects from the thick substrate material with the optical limiting mechanism from the thin nonlinear sample layer. It is found from the theoretical and experimental studies that the magnitude of the transmission can be tuned by suitably tailoring the structural geometry of the layered material (thickness of both substrate and nonlinear sample layer). For instance a high contrast in nonlinear transmission is seen for heavy doped samples. The

principle behavior is seem to be observable for all bi-layer structures ($\text{TiO}_2\text{-SiO}_2$), all type of laser polarizations without any phase matching requirement. The identified optical diode like behavior from simple bi-layer structure can be used as an alternative for the recently proposed complex geometrical structures.

By suitably engineering the bi or multi-layered structures, light itself can selectively control its intensity while its propagation through a layered structural media. The observed directional selective nonlinear optical limiting can be extended to any spectral regime of interest by suitably selecting the proper nonlinear material. Our study suggests that multi-layer samples based on glass metal nanocomposites are very promising materials for tailoring novel optical elements such as optical diodes, optical switches with unprecedented directional properties.

Chapter 7

Summary

The goal of this work was to study the third-order optical nonlinearities of glass-metal nanocomposites, showing very special nonlinear properties due to structural anisotropy on the nanoscale or its macroscopic geometric structure.

Nanocomposite materials with special geometrical structure prepared via mechanical stretching method have been selected for the nonlinear measurements. Mechanical stretching method introduces a shape anisotropy in the geometrical structure of the nanoparticle. Macro as well as microscopic anisotropy results when the nanoparticles undergoes a change in shape from spherical to spheroidal one with a common orientation of the symmetry axis of the spheroids. Samples with varying aspect ratio for the prolate ellipsoidal nanoparticles has been used for the nonlinear studies. The phase and the amplitude of the third order nonlinearity is measured using femtosecond Z-scan technique. By suitably selecting the polarization state of interacting laser pulse, we could study the nonlinear properties arising from the individual particle axis separately.

Under infrared laser pulse excitation, for highly anisotropic nanoparticles (highly stretched nanoparticles-LSPR₅₅₀) the light interaction can be switched from the near to far resonant regime. A sign reversal in nonlinearity is observed upon switching between the light interaction regime. The shape anisotropy of the composite material is found to play a major role in overall nonlinear optical process. Under sub-picosecond laser pulse excitation, the optical nonlinearity of the nanoparticles is found to be a positive hot-electron contribution. In this context the saturable absorption observed in the near resonant regime has been interpreted as the process resulting from the damping of the surface plasmon oscillation; where the sign of the nonlinearity is strongly influenced by the dispersive nature of the local field factor. On other hand an optical limiting mechanism (due to two-photon absorption) is

observed in the non-resonant regime. Irrespective of the light interaction regime, the sign of the optical nonlinearity is retained for nanoparticles with lesser degree of structural anisotropy. The dispersive nature of the optical nonlinearity is calculated by making use of the structural anisotropy of the nanoparticle. In the near resonant regime, the calculated dispersion of the optical nonlinearity is strongly dependent on the topological structure of the nanoparticle.

Following the discussion on the shape induced optical nonlinearity, we have extended our studies on Maxwell Garnett type of samples, which are prepared via laser irradiation technique. The measured nonlinear properties of the sample is found to replicate the effective medium characteristics in the nonlinear optical regime. Especially the trend of the optical nonlinearity nearly maps the material properties of the nanocomposite systems together with the spectrally dependent field enhancement factor.

The chapter “Directional selective optical limiting” deals with the optical diode like behavior observed in simple bi-layer structures. The theoretical prediction shows uni-directional transmission for a simple bi-layer structure. The nonlinear refractive effects arising from the thick substrate material plays a key role in the observed anisotropic transmission. Accordingly, the magnitude of the anisotropic transmission is strongly dependent upon the intensity of the input light beam. The experimental results undoubtedly demonstrated the theoretical predictions. Our studies show that, a strong self-focusing effect from the glass substrate prior to the thin nonlinear sample results in contraction of the laser beam radius to a considerable extent. Correspondingly an enhanced optical limiting mechanism is observed while irradiating from the substrate side of the sample as compared to the irradiation from the thin nonlinear sample side. The magnitude of the anisotropic transmission is suitably controlled by optimizing the thickness of both substrate plate and nonlinear sample layer. The uni-directional transmission is found to be a general characteristic behaviour of a bi-layer sample structure. Compared to the other proposed complex structures, the present material structure will work for all light polarizations without any phase matching requirements.

For the future prospective, one can think of generating a structure which combines the shape anisotropy of the nanoparticles with the bi-layer structure, which can result in strong contrast in the uni-directional transmission. The proposed material structure consists of a thin layer of spherical nanoparticles (which are heavy doped) sandwiched between the thick substrate material and a thin layer of light doped ellipsoidal nanoparticles (with a preferential orientation of the long axis of the

nanoparticles). While irradiating from the particle side of the sample, one can nullify the nonlinear absorption (or enhance the nonlinear transmission) by tuning the angular orientation of the long axis ellipsoid with respect to the laser polarisation direction. In effect one can cancel the interplay between the saturable (negative absorption-from ellipsoidal) and two-photon absorption (positive absorption-from spherical nanoparticle) mechanism.

Appendix A

Appendix 1: Mathematical calculations

A.1 Symmetrisation technique for the evaluation of nonlinear refraction

Z-scan technique allows the simultaneous determination of nonlinear refraction (NLR) and absorption (NLA) through the closed and open aperture scheme. If the nonlinear transmission measurements are performed at the vicinity of resonant transition (for instance the single photon, two photon or multiphoton absorption), the closed aperture signal is dominated by the contributions from nonlinear absorption process. To extract the value of NLR index one must first model the the open aperture measurement to determine the numerical value of nonlinear absorption coefficient NLA and then take it into account in the Closed aperture scan modelling. On other hand the contribution due to NLA can be seperated out from closed aperture scan by the mathematical procedure *Symmetrisation technique* proposed by M.Yin et.al [Ref1].

For laser beams with circular symmetry and low irradiances, the normalised transmittance is given by

$$T(z) = 1 + T_{\Delta\Phi}(z) + T_{\Delta\psi}(z) \quad (\text{A.1})$$

$T_{\Delta\Phi}(z)$ is originating from NLR is an odd function of z and $T_{\Delta\psi}(z)$ is caused by NLA is an even function of z which are given by

$$T_{\Delta\Phi}(x) = \frac{4x}{(x^2 + 9)(x^2 + 1)} \Delta\Phi_0 \quad (\text{A.2})$$

$$T_{\Delta\psi}(x) = \frac{-2(x^2 + 3)}{(x^2 + 9)(x^2 + 1)} \Delta\psi_0 \quad (\text{A.3})$$

where $x = z/z_0$, $\Delta\Phi = (k n_2 I_0 f(t) L_{eff})$, $\Delta\psi = \frac{\beta I_0 f(t) L_{eff}}{2}$ and $L_{eff} = \frac{(1 - \exp(-\alpha L))}{\alpha}$ with α & L is the linear absorption coefficient and L is the thickness of the sample I_0 is the on axis irradiance of the laser beam at the focus, $f(t)$ is the temporal envelope of laser beam and $k = (2\pi/\lambda)$ & λ represents the wave vector and the wavelength of the excitation pump.

Consequently $T_{\Delta\Phi}(z)$ and $T_{\Delta\psi}(z)$ are easily separated from a closed aperture Z-scan by the

$$T_{\Delta\Phi}(z) = \frac{T(z) - T(-z)}{2} \quad (\text{A.4})$$

$$T_{\Delta\psi}(z) = \frac{T(z) + T(-z)}{2} - 1 \quad (\text{A.5})$$

A.2 Appendix 2: Calculation of the shape factor L

For our studies we have chosen nanocomposite systems having different degree of shape anisotropy. As described corresponding chapter 2, the shape anisotropy of the nanoparticles can be described interms of shape factor L . For instance in chapter 4, from the polarized linear extinction spectra (figure 4.1) there are two sets of samples having same degree of shape anisotropy factor which is named as LSPR_550. Besides this particular set of samples there are other sets of samples having different degree of shape anisotropy which are named as LSPR_1200 and LSPR_450 respectively.

From the Mie calculation, using the spectral gap between the TSPR and LSPR band of each sample, at first we explicitly calculated the eccentricity e of the nanocomposite geometry .

For sample LSPR_1200, the aspect ratio of the nanoparticle geometry is found out to be 1:6.5 (ratio of semi-minor to semi-major axis) which corresponds to eccentricity value, $e = 0.988$. For LSPR_550, $e = 0.909$ (aspect ratio = 1:2.4) and for the sample LSPR_450, $e = 0.699$ (aspect ratio= 1:1.4).

A.3 Appendix 3: Maxwell-Garnett Calculations

In general the imaginary part of the metal nanoparticle dielectric function is represented as

$$\varepsilon_I(\omega, R) = \varepsilon_{I(bulk)} + \frac{\omega_p^2 \Gamma}{\omega(\omega^2 + \Gamma^2)}$$

where ω_p represents the Drude plasma frequency. Since $\omega^2 \gg \Gamma^2$ we can approximate the above equation as

$$\varepsilon_I = \varepsilon_{I(bulk)} + \frac{\omega_p^2 \Gamma}{\omega^3},$$

Where the first term signifies the imaginary part of interband dielectric function and the second term denotes the Drude contribution. When ever the size of the nanoparticle become comparable or less than the mean free path of conduction electrons l_∞ (Ag = 52 nm at 273 K), an additional surface scattering plays an important role in the overall collisional mechanism. It consists of bulk scattering term (described through Mathessian's rule) and also the scattering of electrons at the surface of the nanoparticle. Thus in general the damping factor Γ can be written as

$$\Gamma [eV] = \Gamma_\infty + \Delta \Gamma (R),$$

$$\Delta \Gamma (R) = A \frac{V_F}{R}, \quad (\text{A.6})$$

here A represents the theory dependent quantity which is strongly depends upon the morphological characteristics of the nanoparticle system, i.e, it includes contributions from the size and the interface effects. As described in work of Kreibig et.al. and Persson in which a decay channel resulting from the chemical interface damping plays a major role in the over all relaxation mechanism. For instance during the chemisorption process, the valence electron eigen state of the gas molecule is degenerated and shifted and a local projected density of states near the Fermi energy of the metallic particle. The resulting structure of the projected density of state depends upon the relative distance between the Fermi-level of the metallic particle and the energy level of the valence electron of the adsorbed molecule. This gives the possibility of the conduction electrons of the particle to occupy the avialable positions through the tunnel effects [41, 57].

For the current scenario, in which the samples are prepared by the laser irradiation technique where the particle shape deformation to ellipsoidal one, can achieved through the selective dissolution of the Ag nanoparticles through the laser irradiation method. In short the laser irradiation method results in field driven removal of silver ions from the nanoparticles. Thus the development of the aspect ratio of the nanoparticles strongly follows the dissolution of silver ions in the selective direction.

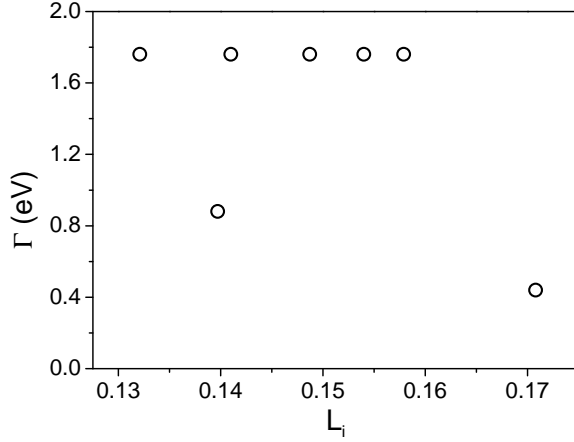


Figure A.1: Fitted value of FWHM for each irradiated area of the sample.

It might be possible that the silver ions in the vicinity of the nanoparticles gets neutrized to form an oxidic core around the silver nanoparticles. Correspondingly the system mimics a core-shell geometry. Also we have observed a red shift in the peak position of the plasmon of the order of 60 nm during the time span of 2 years which is a special signature of oxidic formation around the metallic core. The broadening observed in the extinction spectra (Chapter 5, figure 5.1) could be resulting from the shape distribution of the nanoparticles and also from the interface effects due to core-shell formation. In this context to replicate the full width at half maximum (FWHM) of the plasmon absorption. we have used the parameter A for the calculation of damping term in the imaginary part of the dielectric function of the nanocomposite system as given in equation A.8. Figure (A.1) shows the calculated value of Γ for each irradiated area.

Using the Maxwell Garnett approximation, the expression for effective dielectric function in the high dilution limit is expressed as

$$\varepsilon_{eff} \approx \varepsilon_d + p\varepsilon_d \frac{(\varepsilon_m - \varepsilon_d)}{L\varepsilon_m + (1 - L)\varepsilon_d} \quad (\text{A.7})$$

where ε_m , ε_d , L and p signifies the dielectric function of metal nanoparticle, dielectric host matrix, the shape and the volume filling factor of the nanoparticle in the host matrix. In general the metallic dielectric function in general can be represented as $\varepsilon_m = \varepsilon_{m1} + i\varepsilon_{m2}$. In the nonlinear optical regime, the change in real and imaginary parts of dielectric function due to the ultrashort laser pulse interaction can be represented as $\varepsilon'_{m1} = \varepsilon_{m1} + \Delta\varepsilon_{m1}$ and $\varepsilon'_{m2} = \varepsilon_{m2} + \Delta\varepsilon_{m2}$.

Hence the dielectric function of the metal nanoparticle in the presence of ultrashort laser pulse excitation can be written as

$$\varepsilon'_m = \varepsilon_m + (\Delta\varepsilon_{m1} + \Delta\varepsilon_{m2}) \quad (\text{A.8})$$

Correspondingly the effective dielectric function of the nanocomposite materials can be re-written as

$$\varepsilon'_{eff} \approx \varepsilon_d + p\varepsilon_d \frac{((\varepsilon_{m1} + \Delta\varepsilon_{m1}) + i(\varepsilon_{m2} + i\Delta\varepsilon_{m2})) - \varepsilon_d}{L((\varepsilon_{m1} + \Delta\varepsilon_{m1}) + i(\varepsilon_{m2} + i\Delta\varepsilon_{m2})) + (1-L)\varepsilon_d} \quad (\text{A.9})$$

We assumed the host matrix to be a linear medium.

From equations (A.7) and (A.8), one can calculate the change in real ($\Delta\varepsilon_{eff1}$) and imaginary parts of ($\Delta\varepsilon_{eff2}$) of metal nanocomposite glass as given below

$$\begin{aligned} \Delta\varepsilon_{effR} = \\ \frac{(\varepsilon_d^2 p) \left[(1-L)^2 \varepsilon_d^2 \Delta\varepsilon_{m1} + L(1-L)\varepsilon_d \left(|\varepsilon'_m|^2 - |\varepsilon_m|^2 \right) + L^2 \left(\varepsilon_{m1} |\varepsilon'_m|^2 - \varepsilon'_{m1} |\varepsilon_m|^2 \right) \right]}{\left([L\varepsilon_{m1} + (1-L)\varepsilon_d]^2 + [L\varepsilon_{m2}]^2 \right) \left([L\varepsilon'_{m1} + (1-L)\varepsilon_d]^2 + [L\varepsilon'_{m2}]^2 \right)} \end{aligned}$$

$$\begin{aligned} \Delta\varepsilon_{effI} = \\ \frac{(\varepsilon_d^2 p) \left[(1-L)^2 \varepsilon_d^2 \Delta\varepsilon_{m2} + 2L(1-L)\varepsilon_d \left(\varepsilon_{m1}\varepsilon'_{m2} - \varepsilon'_{m1} \right) + L^2 \left(\varepsilon'_{m2} |\varepsilon_m|^2 - \varepsilon_{m2} |\varepsilon'_m|^2 \right) \right]}{\left([L\varepsilon_{m1} + (1-L)\varepsilon_d]^2 + [L\varepsilon_{m2}]^2 \right) \left([L\varepsilon'_{m1} + (1-L)\varepsilon_d]^2 + [L\varepsilon'_{m2}]^2 \right)} \end{aligned}$$

The change in real and imaginary parts of dielectric constant is related to the third order nonlinear susceptibility through the following expressions

$$\begin{aligned} Re \chi^{(3)} &= \frac{\Delta\varepsilon_1}{3\pi |E|^2} \\ Im \chi^{(3)} &= \frac{\Delta\varepsilon_2}{3\pi |E|^2} \end{aligned} \quad (\text{A.10})$$

For the calculation we have set the value of $\Delta\varepsilon_1 = 0.3$, $\Delta\varepsilon_2 = 0.4$ and $E = 1.5 \times 10^8 \text{V/m}$ [22]. As described in the chapter 5, each irradiated area of the sample is characterized by a particular shape factor L and filling factor p . Hence substituting the parameter values in the equation (10) we calculated the third order nonlinear absorption coefficient for β for each irradiated area.

Bibliography

- [1] N.W. Ashcroft and N.D. Mermin. *Solid State Physics*. Harcourt Brace College, 1976.
- [2] K. J. Berg and H. Hofmeister. Small silver particles in glass-surface layers produced by sodium-silver ion-exchange - their concentration and size depth profile. *Z. Physik D*, 20:309–311, 1991.
- [3] J. Y. Bigot, V. Halte, J. C. Merle, and A. Daunois. Electron dynamics in metallic nanoparticles. *Chemical Physics*, 251:181–203, 2000.
- [4] C. F Bohren. How can a particle absorb more than the light incident on it ? *Americal J. Physics*, 51:323–327, 1983.
- [5] C. F. Bohren and D. R. Huffman. *Absorption and Scattering of Light by Small Particles*. John Wiley & Sons, 1983.
- [6] R. W. Boyd. Order-of-magnitude estimates of the nonlinear optical susceptibility. *Journal of Modern Optics*, 46:367–378, 1999.
- [7] R. W. Boyd. *Nonlinear Optics*. Elsevier, 2003.
- [8] P. N. Butcher and D. Cotter. *The Elements of Nonlinear Optics*. Cambridge University Press, 1990.
- [9] P. Chakraborty. Metal nanoclusters in glasses as non-linear photonic materials. *Journal of materials science*, 33:2235–2249, 1998.
- [10] Anthony J. DeMariaio. Photonics vs electronics technologies. *Optics News*, OSA Annual Meeting Nov.2:22–37, 1989.
- [11] D. F. Eaton. Nonlinear optical materials. *Science*, 253:281–287, 1991.
- [12] E. L. Falcao-Filho, Cid. B. de. Araujo, and J. J. Rodrigues Jr. High-order nonlinearities of aqueous colloids containing silver nanoparticles. *Journal Optical Society of America B*, 24:2948–2956, 2007.
- [13] Y. Fan, J. Han, Z. Wei, C. Wu, Y. Cao, X. Yu, and H. Li. Subwavelength electromagnetic diode: One-way response of cascading nonlinear meta atoms. *Applied Physics Letters*, 98:151903–151905, 2011.

BIBLIOGRAPHY

- [14] N. D. Fatti and F. Vallee. Ultrafast optical nonlinear properties of metal nanoparticles. *Applied Physics B*, 73:383–390, 2001.
- [15] C. Flytzanis. Nonlinear optics in mesoscopic composite materials. *J. Phys. B. At. Mol. Opt. Physics*, 38:S661–S679, 2005.
- [16] A. H. Gavorgyan. Nonreciprocal waves in absorbing multilayer systems. *Technical Physics letters*, 29:60–68, 2003.
- [17] R. J. Gehr and R. W. Boyd. Optical properties of nanostructured optical materials. *Chemistry of Materials*, 8(8):1807–1819, 1996.
- [18] J. K. Ghaleh, N. Mansour, D. Ashkenasi, and J-H. Hoffmann. Nonlinear optical response in alkali-silicate glasses at 800 nm femtosecond irradiations. *Journal of Optics communications*, 246:213–218, 2004.
- [19] Y. Guillet, M. R. Huyeh, and Burno-Palpant. Influence of laser pulse characteristics on the hot electron contribution to the third-order nonlinear optical response of gold nanoparticles. *Physical Review B*, 79(Y Guillet, M. R. Huyeh and Burno-Palpant):045410–045419, 2009.
- [20] F. Hache, D. Ricard, C. Flytzains, and U. Kreibig. The optical kerr effect in small metal particles and colloids. *Applied Physics A*, 47:347–357, 1988.
- [21] F. Hache, D. Ricard, and C. Flytzanis. Optical nonlinearities of small metal particles: surface mediated resonance and quantum size effects. *Journal Optical Society of America B*, 3:1647–1655, 1986.
- [22] Y. Hamanaka, A. Nakamura, N. Hayashi, and S. Omi. Dispersion curves of complex third-order optical susceptibilities around the surface plasmon resonance in ag nanocrystal-glass composites. *Journal of Optical Society of America B*, 20(6):1227–1232, 2003.
- [23] Y. Hamanaka, A. Nakamura, S. Omi, D. N. Fatti, F. Vallee, and C. Flytzains. Ultrafast response of nonlinear refractive index of silver nanocrystals embedded in glass. *Applied Physics Letters*, 75(12):1712–1715, 1999.
- [24] J. W. Haus, N. Kalyaniwalla, R. Inguva, M. Bloemer, and M. C. Bowden. Nonlinear-optical properties of conductive spheroidal particle composites. *Journal of Optical Society of America B*, 6(4):797–807, 1989.
- [25] E. Hecht and A. R. Ganesan. *OPTICS*. Pearson, Fouth Edition, 2002.
- [26] E. J. Heilweil and R. M. Hochstrasser. Nonlinear spectroscopy and picosecond transient grating study of colloidal gold. *Journal of Chemical Physics*, 82:4762–4770, 1985.
- [27] R. Hellwarth, J. Cherlow, and T. T. Yang. Origin and frequency dependence of nonlinear optical suceptibilities of glasses. *Physical Review B*, 11:964–968, 1975.

- [28] H. Hofmeister, W-G. Drost, and A. Berger. Oriented prolate silver nanoparticles in glass-characteristics of novel dichoric polarizers. *Nanostructured Materials*, 12:207–210, 1999.
- [29] Xiaoyong. Hu, Z. Li, J. Zhang, H. Yang, Q. Gong, and X. Zhang. Low-power and high-contrast nanoscale all-optical diodes via nanocomposite photonic crystal microcavities. *Advanced functional Materials*, 21:1803–1809, 2011.
- [30] J. Hwang, H. M. Song, B. Park, S. Nishimura, W. J. Wu, T. Toyooka, Y. Tankanishi, K. Ishikawa, and H. Takezoe. Electro-tunable optical diode based on photonic bandgap liquid-crystal heterojunctions. *Nature Materials*, 4:383–387, 2005.
- [31] J. D Jackson. *Classical Electrodynamics*. Wiley, New York, 1999.
- [32] K. Jamshidi-Ghaleh and N. Mansour. Nonlinear absorption and optical limiting in duran glass induced by 800 nm femtosecond laser pulses. *Journal of physics D: Applied Physics*, 40:366–369, 2007.
- [33] H. John Caulfield and Shlomi Dolev. Why future supercomputing requires optics. *Nature Photonics*, 4:261–263, 2010.
- [34] P. B. Johnson and R. W. Christy. Optical constants of the noble metals. *Physical Review B*, 6:4370 – 4379, 1972.
- [35] M. Kaempfe. *Laserinduzierte Deformation metallischer Nanopartikel in Gläsern*. PhD thesis, Martin-Luther University, 2000.
- [36] M. Kaempfe, H. Graener, A. Kiesow, and A. Heilmann. *Applied Physics Letters*, 79:1876–18788, 2001.
- [37] M. Kaempfe, T. Rainer, J. K. Berg, G. Seifert, and H. Graener. *Applied Physics Letters*, 77:459–461, Erratum: *ibid.* 77, 459 (2000), 1999.
- [38] A. E. Kaplan. External self-focusing of light by a nonlinear layer. *Radio Physics and Quantum electronics*, 12(6):692–696, 1969.
- [39] K. L. Kelly, E. Coronado, L. L. Zhao, and C. G. Schatz. The optical properties of metal nanoparticles: The influence of size, shape, and dielectric environment. *J. Phys. Chem. B*, 107:668–677, 2002.
- [40] H. Kogelnik and T. Li. Laser beams and resonators. *Applied Optics*, 5(10):1550–1567, 1966.
- [41] U. Kreibig and M. Vollmer. *Optical properties of Metal Clusters*. Springer, 1995.
- [42] M-J. Lammarre, F. Billard, and L. Martinu. Local field calculations of the anisotropic nonlinear absorption coefficient of a aglinded gold nanorods embedded in silica. *Journal Optical Society of America B*, 25:961–971, 2008.

BIBLIOGRAPHY

- [43] J. Li, S. Liu, Y. Liu, F. Zhou, and Zhi-Yuan. Li. Anisotropic and enhanced absorptive nonlinearities in a macroscopic film induced by aligned gold nanorods. *Applied Physics Letters*, 96:263103–26106, 2010.
- [44] S. Link and A. M. El-Sayed. Optical properties and ultrafast dynamics of metallic nanocrystals. *Annu. Rev. Phys. Chem*, 54:331–66, 2003.
- [45] S. A. Maier and H. A. Atwater. Plasmonics: Localization and guiding of electromagnetic energy in metal/dielectrics structures. *Journal of Applied Physics*, 98:011101–011110, 2005.
- [46] J. H. Marburger. Self-focusing : Theory. *Progress in Quantum Electronics*, 4:35–110, 1975.
- [47] Ralf Menzel. *Photonics-Linear and nonlinear interactions of laser light and matter*. Springer, 2007.
- [48] G. Mie. Beiträge zur optik trüber medien, speziell kolloidaler metallösungen. *Annalen der Physik*, 25:377, 1908.
- [49] S. Fujiwara N. Sugimoto, H. Kanbara and K. Tanaka. Ultrafast response of third-order optical nonlinearity in glasses containing bi₂o₃. *Optics Letters*, 21:1637–1639, 1996.
- [50] Ahmet Akin Ünal. *Time-resolved investigations on ultrafast shape modification dynamics of silver nanoparticles embedded in glass*. PhD thesis, Martin-Luther-Universität Halle-Wittenberg, 2009.
- [51] L. Palfalvi and J. Hebling. Z-scan study of the thermo-optical effect. *Applied Physics B*, 78:775–780, 2004.
- [52] Burno Palpant. Third-order nonlinear optical response of metal nanoparticles, p.p 461-508.
- [53] M. J. Paz-Alonso, H. Michinel, and S. Bara. Nonlinear refractive index of glass plate used for beam transformation and its applications to z scans. *Journal Optical Society of America B*, 20:2484–2491, 2003.
- [54] M. Perner, P. Bost, U. Lemmer, Von. G. Plessen, J. Fledmann, U. Becker, M. Menning, and M. Schmidt. Optically induced damping of the surface plasmon resonance in gold olloids. *Physics Review Letters*, 78(11):2192–2195, 1997.
- [55] R. Philip, M. Anija, C. S. Yelleswarapu, and D. V. G. L. N. Rao. Passive all-optical diode asymmetric nonlinear absorption. *Applied Physics Letters*, 91:141118–10, 2007.
- [56] R. Philip, G. R. Kumar, N. Sandhyarani, and N. Pradeep. Picosecond optical nonlinearity in monolayer-protected gold, silver, and gold-silver alloy nanoclusters. *Physical Review B*, 62:13160–13166, 2000.

-
- [57] Anatoliy Pinchuk and Uwe Kreibig. Interface decay channel of particle surface plasmon resonance. *New Journal of Physics. IOP*, 5:15101–15115, 2003.
- [58] G. Piredda. *Materials for Nonlinear Optics: Semicontinuous Gold Films and Fast Saturable Absorbers*. PhD thesis, University of Rochester, 2008.
- [59] R. V. Ramaswamy and R. Srivastav. Ion-exchanged glass waveguides : a review. *Journal of Lightwave Technology*, 6:984–1000, 1988.
- [60] D. Ricard, P. Roussignol, and C. Flytzains. surface mediated enhancement of phase conjugation in metal colloids. *Optics Letters*, 10(10):511–513, 1986.
- [61] R. Rosei. Temperature modulation of the optical transitions involving the fermi surface in ag: Theory. *Physical Review B*, 10(2):474–483, 1974.
- [62] R. Rosei, C. H. Culp, and J. H. Weaver. Temperature modulation of optical transitions involving the fermi surface in ag : Experimental. *Physical Review B*, 10(2):484–489, 1974.
- [63] M. Scharte, R. Porath, T. Ohms, M. Aeschlimann, J. R. Krenn, H. Ditlbacher, F. R. Aussenegg, and A. Liebsch. Do mie plasmons have a longer lifetime on resonance than off resonance. *Applied Physics B*, 73:305–310, 2001.
- [64] V.M. Shalaev. *Nonlinear Optics of Random Media:Fractal Composites and Metal-Dielectrics*. Springer, 2000.
- [65] M. Sheik-Bahae. Third order optical nonlinearities. *OSA Handbook of Optics*, IV, Chapter 17:1–50, 2000.
- [66] M. Sheik-Bahae and M. P. Hasselbeck. *Third order optical nonlinearities*. OSA Hand of Optics, Vol. IV, Chapter. 17, 2000.
- [67] M. Sheik-Bahae, A. A. Said, J. D. Wei, H-T. Hagan, and Van. W. E. Stryland. Sensitive measurements of optical nonlinearities using single beam. *IEEE Journal of Quantum Electronics*, 26(4):760–769, 1990.
- [68] M. Sheik-Bahae, A. A. Saiid, J. D. Hagan, J. M. Soilau, and Van. W. E. Stryland. Nonlinear refraction and optical limiting in thick media. *Optical Engineering*, 30(8):1228–1235, 1991.
- [69] D. D. Smith, G. Fisher, R. W. Boyd, and A. D. Geogory. Cancellation of photoinduced absorption in metal nanoparticle composites through a counter-intuitive consequence of local field effects. *Journal of Optical Society of America B*, 14(7):6200–6205, 1997.
- [70] J. E. Spie and R. W. Boyd. Nonlinear susceptibilities of composite optical materials in the maxwell garnett model. *Physics Revie A*, 46(3):1614–1629, 1992.

BIBLIOGRAPHY

- [71] A. Stalmashonak, G. Seifert, A. A. Unal, U. Skrypczak, A. Podlipensky, A. Abdolvand, and H. Graener. Toward the production of micropolarizers by irradiation of composite glasses with silver nanoparticles. *Applied Optics*, 48:F37–F43, 2009.
- [72] Andrei Stalmashonak. *Laser-induced shape transformation of silver nanoparticles embedded in glass*. PhD thesis, Martin Luther University, 2010.
- [73] C-K. Sun, F. Vallee, L. H. Acioli, E. P. Ippen, and J. G. Fujimoto. Femtosecond-tunable measurement of electron thermalization in gold. *Physical Review B*, 50:15337–15348, 1994.
- [74] R. L. Sutherland. *Hand book of Nonlinear Optics*. Marcel Dekker Inc., 1996.
- [75] L. W. Tutt and T. F. Boggess. A review of optical limiting mechanisms and devices using organics, fullerenes, semiconductors and other materials. *Progress in Quantum Electronics*, 17:299–338, 1993.
- [76] Eva M Vogel. Glasses as nonlinear photonics materials. *J. Am. Ceram. Soc.*, 72:719–724, 1989.
- [77] D. Weaire, S. B. Wherrett, A. D. Miller, and D. S. Smith. Effect of low-power nonlinear refraction on laser beam propagation insb. *Optics Letters*, 4:331–333, 1974.
- [78] Tai-Huei. Wei and Tzer-Hsiang. Huang. A stud of photophysics using the z-scan technique: lifetime determination for high-lying excited states. *Optical and Quantum Electronics*, 28:1495–1508, 1996.
- [79] A. Yariv. *Quantum Electronics-3rd edition*. John Wiley & Sons, 1987.

Acknowledgements

I would like to express my deep and sincere gratitude to my supervisor Dr. Seifert. His understanding, encouragement and personal guidance have provided the best possible basis for the present thesis and a large comfort zone during my entire Ph.D time. His logical way of thinking has been of great value for me. Throughout my thesis-writing period, he provided good teaching, good company, and lots of good ideas. I would have been lost without him.

I shall be ever obliged to Dr. Jens Lange for his technical assistance in the lab and the encouragement. I can't remember a single day when he was not willing to discuss the obstacles associated with the experiment. I also truly thank Prof. Wehrspohn whose suggestions and encouragement had been a source of great inspiration for me.

I want to thank all my colleagues from Optics, μ MD and ZIK for providing a warm and lively atmosphere. Specially Mortiz, Snigdha, Tino, and Armin who always had an open ear to listen to me and provide invaluable help at any point during the day. Some of my experiments involving PHAROS laser system would not have materialized without the assistance of Ulrich, for which I thank him sincerely. Many thanks to Frau.Otten for the kind help in preparing the samples. I also owe a lot to my ex-colleagues specially Akin, Andre, Stefan, and Sumedha for providing a stimulating and fun-filled environment especially during the initial stages of my Ph.D life in Halle.

I thank CODIXX AG for providing samples with Ag nanoparticles for the experiments.

I am grateful to Prof. Graener and IMPRS Halle for giving me an opportunity to participate in this Ph.D programme project.

I would also like to take this opportunity to thank my Alma Mater for making me what I am today. My greatest regards to Rajan Sir who always mentored me throughout my academic life. Special thanks to Gin sir and Charu sir for the nice teachings and encouragement which I received during my stay in IIT G. I am grateful to my classmates Anto, Thejal, Hari, Pradheesh and Ginu and many more. Many thanks to Remya for the critical reading of the thesis.

My sincere love and regards to my grand parents for the memorable moments. Special regards to my brother who has been a source of inspiration throughout my life. I owe a lot to my almighty father for bestowing upon me to face different phases of life and complete this project successfully.

Lastly, and most importantly, I wish to thank my parents,. They raised me, supported me, taught me, and loved me. To them I dedicate this thesis.



Curriculum Vitae

Personal details

Name : Sabitha Mohan

Date of Birth : 01-05-1980

Place of Birth : Mariathuruth, Kottayam, India

Marital Status : Single

Present Address: Richard Paulick Strasse-13, 06124 Halle-Saale, Germany

Education

1995–97 Pre-degree, Mahatma Gandhi University

1997–2000 B.Sc Physics, Mahatma Gandhi University

2000–02 M.Sc Physics, Mahatma Gandhi University

2004–07 Research associate, IIT Guwahati

2007- Ph.D Student, Optics group, Martin-Luther-University, Halle-Wittenberg

Master thesis (2001-02): Growth and Liesegang ring phenomena of calcium phosphate crystals

IIT G project: Fabrication and Characterization of silver nanocluster embedded planar waveguides in glass

PhD thesis title: Third-order optical nonlinearities of glass-metal nanocomposites

Work Experience

Two Years of assistantship in B-tech lab course, IIT Guwahati.

Assistantship in Physikalische Grund Praktikum, Martin Luther University.

Research Publications

- S.Mohan, G. Jose, *Stability of Core-Shell nanoparticles formed in dielectric media*, Applied Phy. Lett., **91**, 253107(2007).
- G.Medhi, P.Nandi, S.Mohan, G.Jose, *Silver Nanocluster Formation in Silicate Glass by Single Step Ion-exchange*, Mat. Lett, **61**, 2259(2007).

Conference

- S. Mohan, H. Graener and G. Seifert, *Surface plasmon assisted optical nonlinearities of metal nano-ellipsoids in glass*, Emerging trends and novel materials in photonics, Delphi, Octo. 2009 (Oral).
 - S. Mohan, U. Skrzypczak, H. Graener, G. Seifert, *Anisotropic nonlinear optical properties of metal nanocomposite glass*, IEEE CLEO EUROPE-EQEC,2009, Munich, Germany (poster).
 - S. Mohan and G. Seifert, *Polarization controlled switching of optical nonlinearity in nanocomposite glass*, DPG meeting 2011, Dresden, Germany (oral).
 - S. Mohan and H. Graener, *Nonlinear Optical properties of metal nanocomposites*, Photonics 2008, Delhi India (poster).
 - S. Mohan, P.Nandhi, G. Jose, *Fabrication and Characterization of silver nanocluster embedded planar waveguides in glass*, (ICOL-2005), Dehradun India, December 2005 (poster).
-

Erklärung

Hiermit erkläre ich, dass ich diese Arbeit selbständig und ohne fremde Hilfe verfaßt, andere als die von mir angegebenen Quellen und Hilfsmittel nicht benutzt und die den benutzen Werken wörtlich oder inhaltlich entnommenen Stellen als solche kenntlich gemacht habe.

Eine Anmeldung der Promotionsabsicht habe ich an keiner anderen Fakultät einer Universität oder Hochschule beantragt.

Sabitha Mohan